Chapter 1
Introduction and Background

The importance of nanoparticles, that is, particles with dimensions in the range of about 10 nm to few hundred nanometers is obvious: They find use as dispersion colors and as adhesives; in industry they play an important role in the formulation of pigments and in the production of catalysts. Finally nanoparticles find use as quantum dots with special properties for electronic coponents. In a thorough study of the scientific literature, it became evident that much has been written on inorganic nanoparticles and on the principles of nanoparticles formation. In contrast, surprisingly, little is learnt of the mechanisms of particle formation of organic systems. Two strategies are conceivable for the formation of the nanoparticles: 1) the mechanical milling of the raw material by wet or dry milling processes; 2) The conversion of the products or educts dissolved in suitable solvents into nanodispersed systems by precipitation, condensation or specific synthesis procedures.

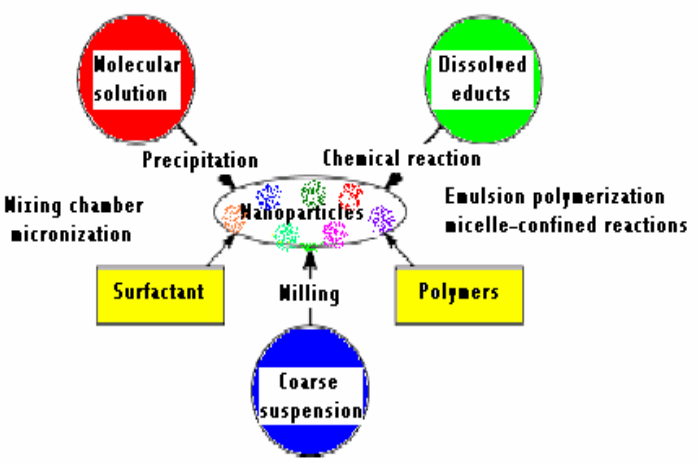

Figure 1.1 Methods for the preparation of the nanoparticles

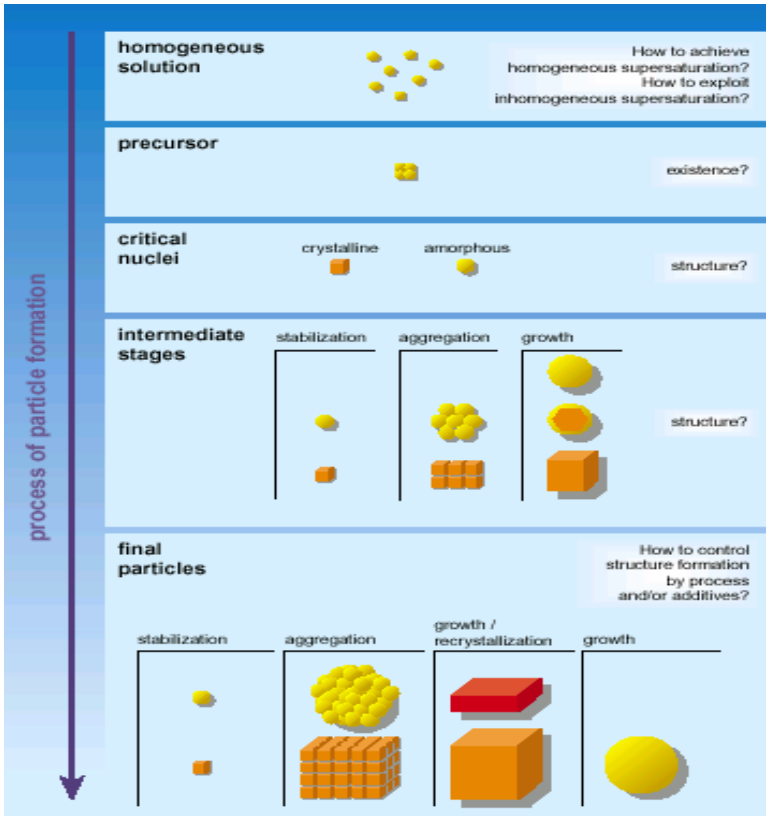

Figure 1.2 Stages of particle formation

Organic nanocrystals have attracted tremendous research interests over the past few years owing to their special properties which lie between the properties of molecules and those of bulk material.[1] The electronic properties of organic nanoparticles differ fundamentally from those of inorganic ones[2] because of weak intermolecular forces accompanying interactions of van der Waals type or hydrogen bonding.[3] Organic nanocrystals allow much increased variability and flexibility in synthesis of materials, preparation of nanoparticles, and investigation of their physicochemical properties such as luminescence[4] or large nonlinear optical efficiency;[5] they are thus expected to serve as novel functional materials in electronics and photonics.[6] From a fundamental point of view, organic nanoparticles are fascinating as their size-dependent optical properties on absorption and emission.[7-10] Nakanashi and co-workers, pioneered investigation of this subject, particularly focusing on fabrication of nanocrystals and characterization of perylene[7] and other organic systems.[6, 7] According to an investigation of nanoparticles of pyrazoline derivatives,[8] the emitted color can be tuned with wither the particle size or the excitation wavelength. Enhanced emission due to aggregation has been reported for organic systems including CN-MBE,[9] *p*-BSP,[10] a silole derivative[11] and conjugated polymers.[12]

Similar to inorganic ones, nanocrystals from organic molecules also show the size-dependent optical properties. For example, β-carotene.

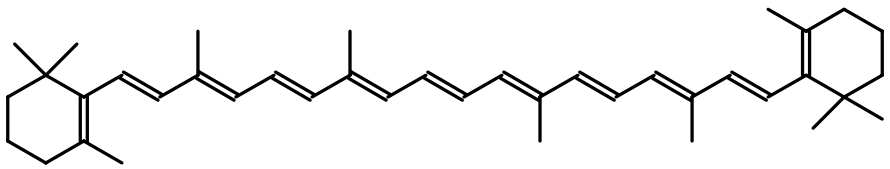

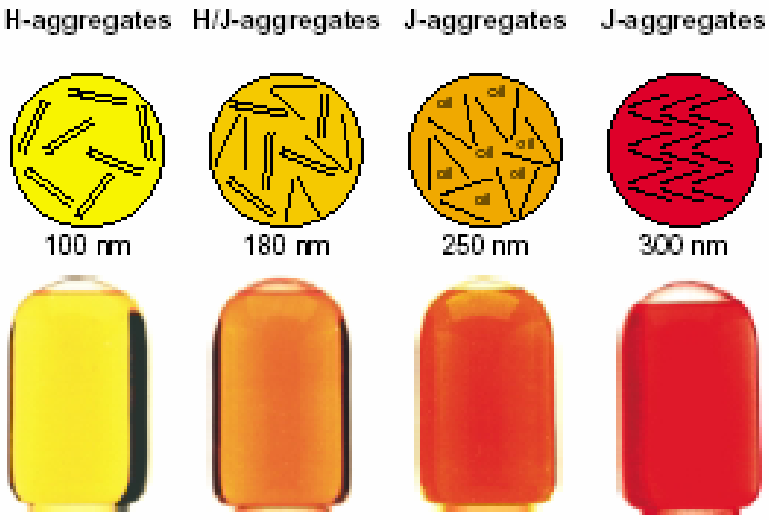

Figure 1.3 Influence of particle size and aggregation structure on the colortone nuance of nanodispersed β-carotene.

In organic molecular crystals, the electronic properties are fundamentally different from those of inorganic metals and semiconductors because of the weak intermolecular interaction forces of the van der waals type or the hydrogen bond[3]. However, organic nanocrystals allow much more variability and flexibility in materials synthesis and nanoparticles preparation and studying their physicochemical properties, such as luminescence[4] or high nonlinear optical efficiency;[5, 13] they are thus expected to serve as novel functional materials in electronics and photonics.[6, 14] Nakanishi and co-workers,[7, 15-20] initiated systematic research on the preparation and characterization of the organic nanocrystals. Their choice of systems investigated was aimed primarily at the potential fields of applications of organic nanocrystals in the area of microelectronics and photonics as alternatives to inorganic systems. Some of the examples included were the preparation of the organic nanaocrystals of Perylene,[15] 6-

dicarbazolyl-2,4-hexadiyne (DCHD),[18] 1,1,4,4-Tetraphenyl-1,3-butadiene (TBP) and so on.

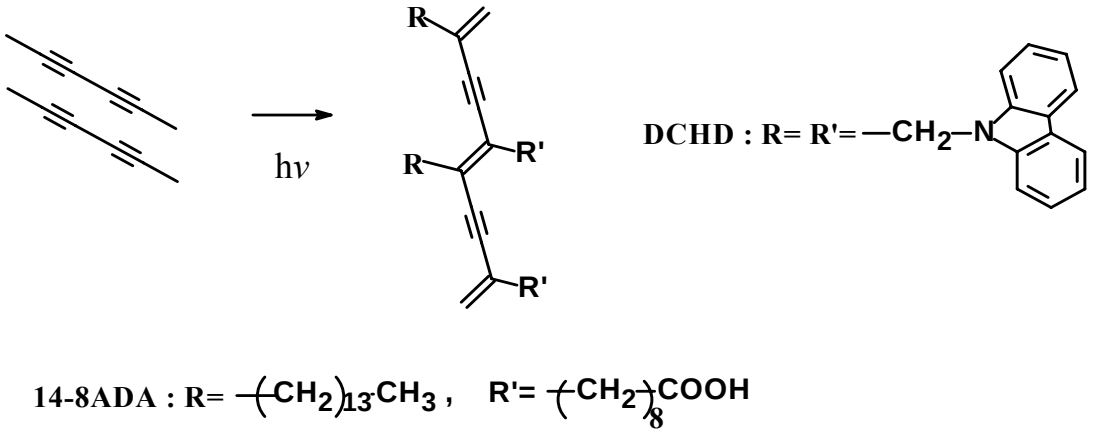

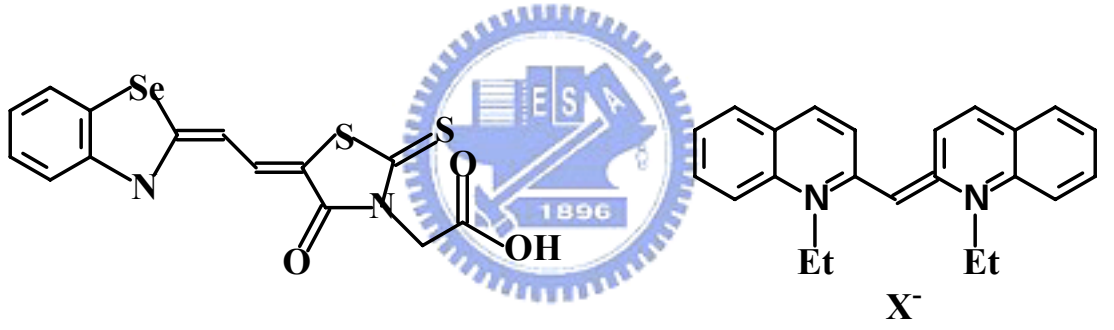

MCSe-C18 **PIC(X)** **X^- : Br^-, I^-, Cl^-**

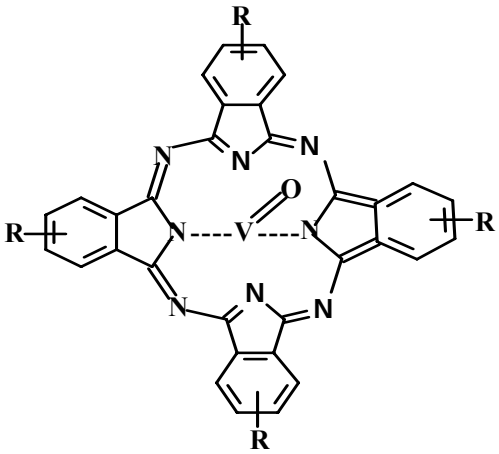

VOPc ($-SC_6H_{13}$)$_4$

R = $-SC_6H_{13}$

Figure 1.4 Various compounds studied by Nakanishi group

In most of the above works, simple reprecipitation method was used for the formation of nanocrystals.

Recently, some of the researchers have investigated the size-dependent optical properties of the organic nanoparticles of perylene,[15]

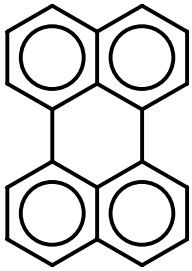

1-phenyl-3-((dimethylamino-styryl)-5-((dimethylamino)phenyl)-2-pyrazoline (PDDP),[8] 1,3-diphenyl-5-pyrenyl-2-pyrazoline (DPP),[21] 1,3-Diphenyl-5-(2-anthryl)-2-pyrazoline (DAP),[22] 1-phenyl-3-((dimethylamino)styryl)-5-((dimethylamino)phenyl)-2-pyrazoline (PDDP)[8], polydiacetylene.[23]

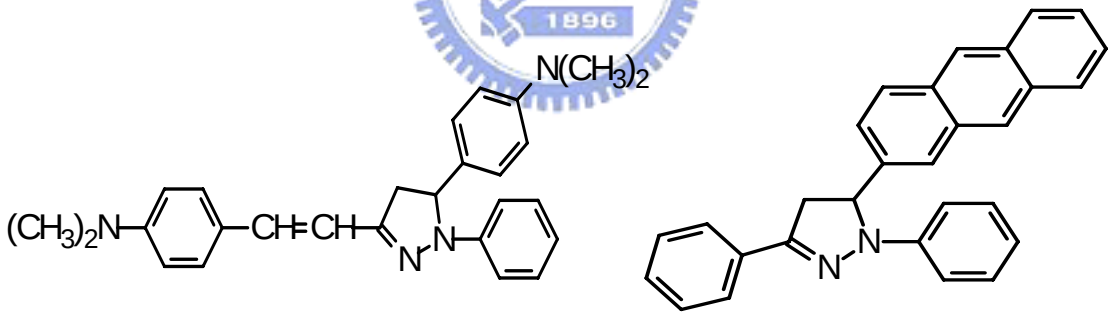

PDDP

DAP

In the investigation on the perylene system, a shift in the absorption band maximum of about 30 nm was found on a reduction in particle size from 200 nm to 50 nm. Little research has been done with regards to the nature of the excited state in the organic molecular crystals. Band shifts of up to 30 nm have also been observed with diphenyl-naphthyl-pyrazoline (DPNP) nanocrystals (400 nm to 20 nm). In investigations on the polydiacetylene

system a blue shift of the absorption maximum of about 15 nm was also found with decreasing particle size (150 nm to 70 nm) and similarly interpreted.

An et al[9] formed the fluorescent organic nanoparticles (FONs) with mean diameter of 30-40 nm of CN-MBE by simple reprecipitation method. CN-MBE nanoparticles exhibit a strongly enhanced emission and on/off fluorescent switching which senses organic vapor. They attributed this enhanced fluorescence emission in CN-MBE nanoparticles to the synergetic effect of planarization and J-aggregation (restricted excimer formation). Enhanced emission due to aggregation has been reported for other organic systems including *p*-BSP,[10] nile red,[24] silole derivatives,[11, 25-35] and conjugated polymers.[12]

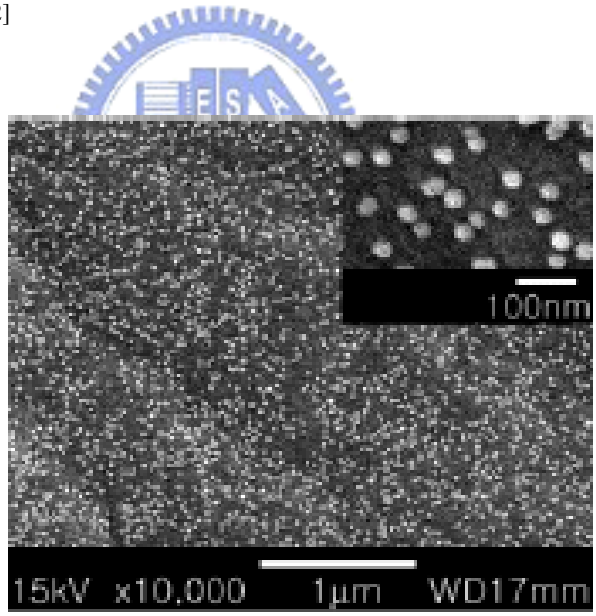

Figure 1.5 SEM image of the CN-MBE nanoparticles

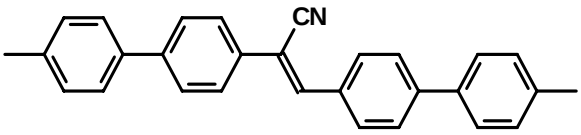

CN-MBE

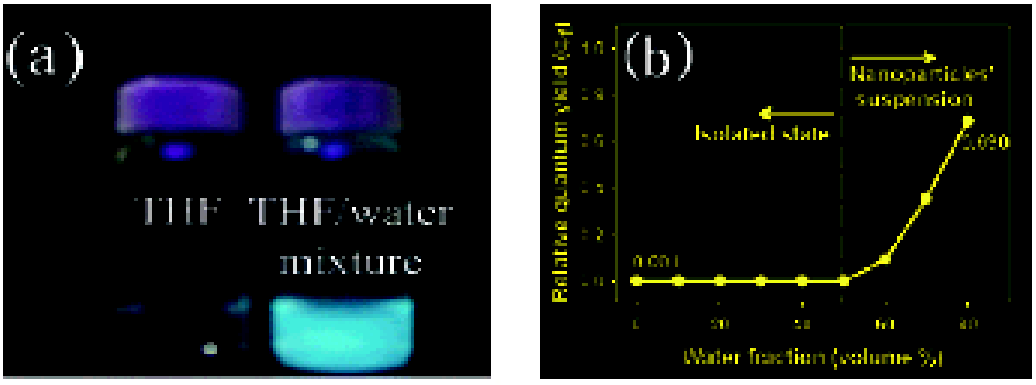

Figure 1.6 (a) The fluorescence emission of CN-MBE in THF (left) and THF/water mixture (80% volume fractions of water) (nanoparticles' suspension) (right) under UV light (365 nm). (b) Relative quantum yields of CN-MBE depending on water fractions in THF.

Silole family is also one of the best examples of fluorescent organic nanoparticles and have been extensively studied by Prof. Tang's group. Typical example being HPS in which Si is bonded with six phenyl rings. Their geometry gets restricted in nanoparticles.

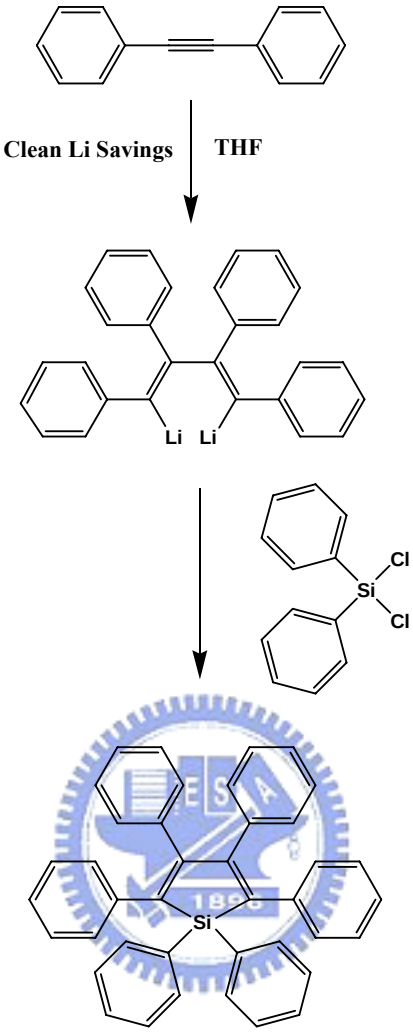

Hexa-Phenyl Silole (HPS)

Scheme 1.1 [25]

In addition, we have also synthesized the rod and coil molecules having conjugated molecules as a rod and polyethylene oxide having various degrees of polymerization, as coil segments. One of the fascinating subjects in areas such as materials science, nanochemistry, and biomimetic chemistry is concerned with the creation of supramolecular architectures with well-defined shapes and functions.[36] Ordered mesoporous solids with nanoscale pore sizes are of interest in areas such as catalysis, sensors, size- and shape-

selective separation media, adsorbents, and scaffolds for composite materials synthesis. Those with pore sizes on the order of 50 nm to 100 μm are also of interest for applications in photonics, optoelectronics, lightweight structural materials, and thermal insulation.[37-39] Self-assembly of molecules through non-covalent forces including hydrophobic and hydrophilic effects, electrostatic interactions, hydrogen bonding, microphase segregation, and shape effects has the great potential for creating such supramolecular structures.[40-44] Rod-coil block copolymers have both rigid rod and block copolymer characteristics. The formation of liquid crystalline nematic phase is characteristic of rigid rod, and the formation of various nanosized structures is a block copolymer characteristic. Apart from the wide range of different supramolecular structures in nanoscale dimensions, another unique characteristic is that rod segments can endow various functionalities such as photophysical and electrochemical properties to the supramolecular materials.[1, 36, 40-42]

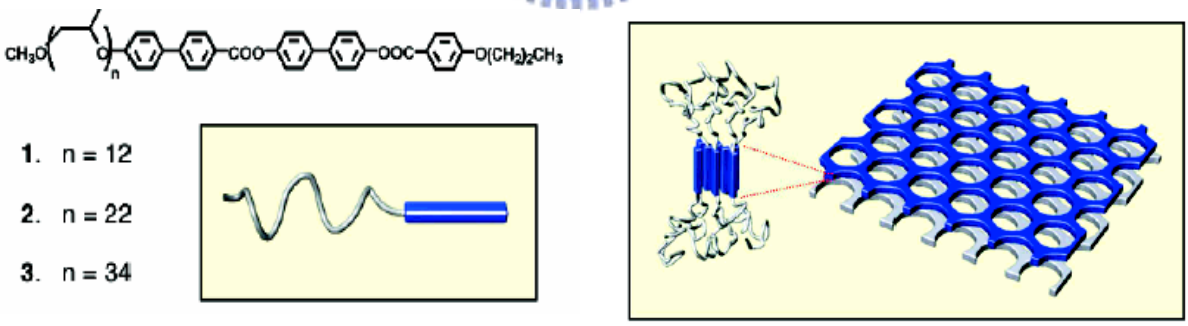

Figure 1.7 Schematic representation of supramolecular honeycomb structure formed by rod-coil molecules is shown in above figure. The honeycomb layers are stacked in ABAB arrangement to give rise to 3-D order. The rod segments are aligned axially perpendicular to the layer plane with a herringbone arrangement.

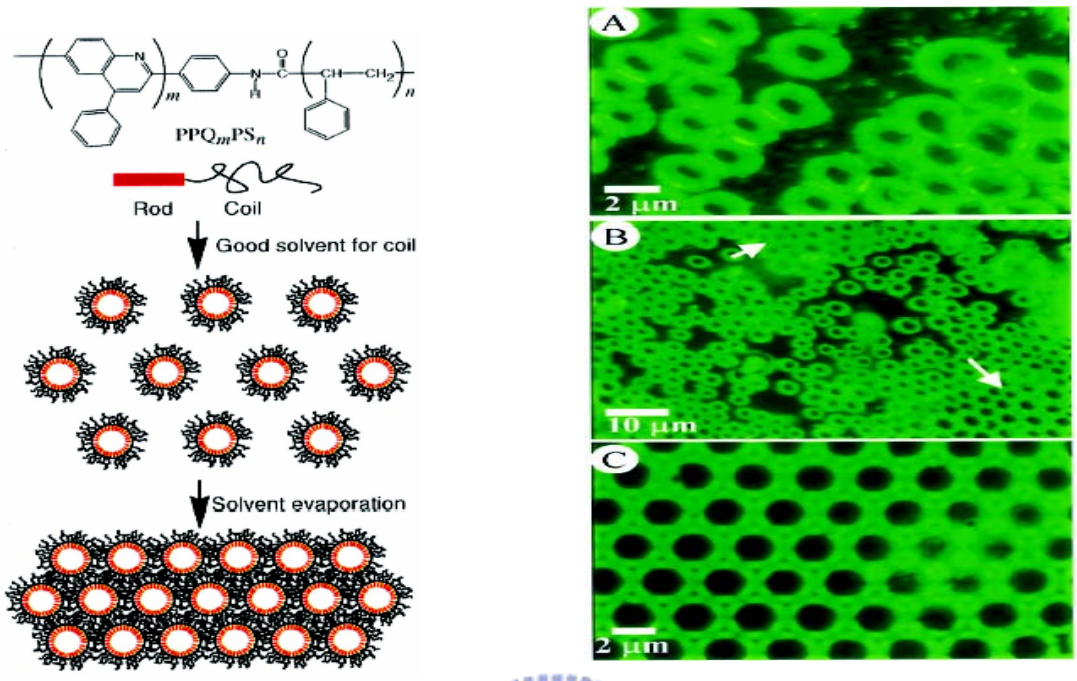

Figure 1.8 1) Molecular structure of the rod-coil diblock copolymer PPQ-PS and schematic illustration of its hierarchical self-assembly into ordered microporous materials 2) Fluorescence photomicrographs of solution-cast micellar films of PPQ_{10}-PS_{300} obtained by ambient air drying of different diblock solution concentrations in CS_2: (A) 0.005 weight %, (B)) 0.01 weight %, and (C) 0.5 weight %. Arrows in (B) indicates regions of self-ordering.

Jenekhe et al[45] reported the self-organization of hollow spherical micelles from a rod-coil diblock copolymer system in a selective solvent for the flexible coil-block and their long-range, close-packed self-ordering into iridescent, ordered microporous solids. They also synthesized amphiphilic poly(phenylquinoline)-block-polystyrene (PPQ-b-PS) rod-coil diblock copolymers and observed their self-assembly into various morphologies, viz., cylindrical, spherical and lamellar.[46]

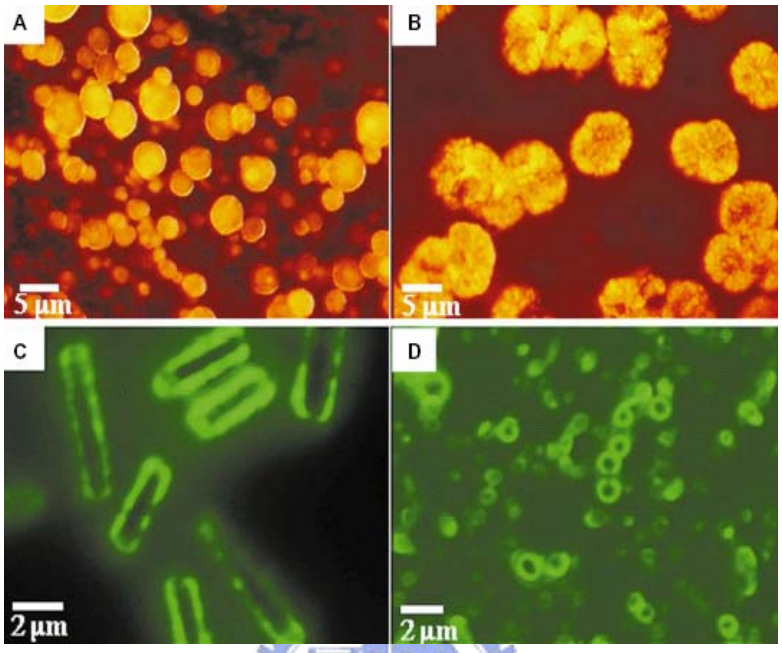

Figure 1.9 Fluorescence micrographs of the PPQ60-PS300 aggregates (A) Spherical (B) lamellar (C) cylindrical, and (D) vesicular aggregates

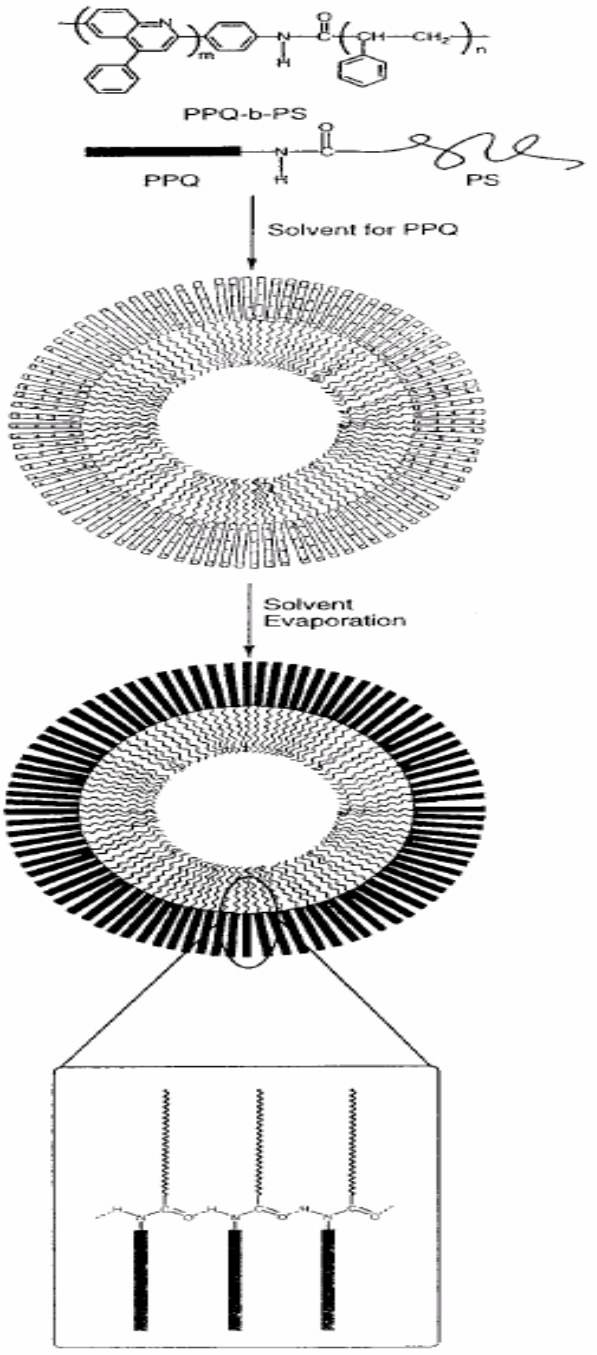

Figure 1.10 Chemical structure and schematic illustration of the self-assembly of PPQ-b-PS rod-coil diblock copolymers into hollow aggregates

The emphasis in the application of nanodispersed organic active compounds and effect materials as well as current research and development targets is concerned mainly with the optimization and control of the optical properties, by particle size and supramolecular structure of the particles. Photoluminscence emission and excitation studies showed that the photophysical properties strongly depend on the supramolecular structure of π-conjugated rod segments[18]. Previous research efforts have led to the synthesis of many conjugated polymers, particularly derivatives of poly(phenylene vinylene) (PPV), soluble in organic solvents and easily processed into films with great promise as organic electronic materials.[47-49] Controlling the nanoscale structure of rodlike conjugated polymers has proven difficult. However, supramolecular order plays a critical role in device performance, as both charge mobility and luminescent efficiency are influenced by molecular aggregation and structural defects.[50-54] π–Conjugated oligomers are now widely studied for use in optoelectronic devices because their well-defined chemical structure facilitates tuning of electronic properties.[55-58] Use of well-defined oligomers reduces defect density while enabling more control over the effective conjugation length. In particular, oligo(*p*-phenylene vinylene)s (OPVs) are being investigated for use in solar cells and light-emitting diodes (LEDs) due to their stability, high luminescent efficiency, and ease of synthesis.[59-62] OPVs with solubilizing substituents combine the low-cost, solution-based processing of conjugated polymers with the improved structural control inherent to oligomers.[54, 58, 62, 63] Recently, Stupp et al[64] synthesized a series of amphiphilic molecules consisting of oligo(phenyl vinylene) asymmetrically end-substituted with a hydrophilic poly(ethylene glycol) (PEG) segment and a hydrophobic alkyl chain. This amphiphilic structure induces self-assembly into both

thermotropic and lyotropic lamellar liquid crystalline (LC) phases. The molecules form strongly fluorescent, self-supporting gels in both water and polar organic solvents. By varying the length of the ethylene glycol block, one can change the structure and solubility of the amphiphile, altering its electronic properties. Photoluminescence (PL) is influenced by the structure of the material, with enhanced emission in the LC state due to assembly of the chromophore in confined two-dimensional layers. Self-assembly controlling molecular aggregation at the nanoscale could significantly improve the performance of OPV-based materials in optoelectronic devices.

Chapter 2

Experimental Section

2.1 Instrumental Techniques (Characterization Methods):

The number of instrumental techniques we used to characterize our materials is summarized below.

2.1.1 Nuclear Magnetic Resonance (NMR):

^{1}H NMR spectra were recorded on Unity-300 spectrometer at 300 MHz for samples in $CDCl_3$, *d*-Acetone, *d*-Methanol solutions.

2.1.2 Scanning Electron Microscopy (SEM):

Images were acquired on a field-emission scanning electron microscope-JSM-6500 F, JEOL. To enhance the conductivity of the specimen, a layer of platinum was sputtered (current 30 mA, pressure 4 Pa, duration 30 s).

2.1.3 Tunneling Electron Microscopy (TEM):

TEM micrographs were observed under JEOL, JEM-2010 using lasey carbon grid as the substrate.

2.1.4 Steady State UV/visible Absorption and Photoluminescence spectra (PL):

UV-Visible absorption spectra were recorded on Hewlett-Packard HP8453 spectrometer and Cary 50, Varian and fluorescence spectra on

F4500 Hitachi and SpectraPro-150 (with Muller SVX 1450 xenon lamp) spectrophotometers in standard manners.

2.1.5 Time-resolved Spectral Measurements:

Femtosecond up-conversion and Picosecond TCSPC measurements were done in collaboration with Prof. E. W.-G. Diau's group.

2.1.6 X-ray Crystallography: (In collaboration with Prof. C. S. Lee's group)
(a) Powder XRD collections. X-ray powder diffraction data were collected with a diffractometer (Bruker D8, 40 kV, 40 mA) with Bragg-Brentano geometry, Cu Kα radiation (λ= 0.15406 nm), and a 40-mm Göbel mirror.
(b) Single-crystal XRD collections. PPB single crystals were obtained on slow evaporation of its THF solution, and its X-ray diffraction data were collected with the use of graphite monochromatized Mo Kα radiation (λ = 0.71073 Å) at 298 K on a Bruker APEX CCD diffractometer.

2.2 Synthetic Procedures:

2.2.1 Synthesis of PPB (1):

The 1,4-di[(*E*)-2-phenyl-1-propenyl]benzene (PPB) was synthesized by Heck coupling reaction. A mixture of α-methylstyrene (2.5 g, 25.4 mmol), 1,4-dibromobenzene (2.0 g, 8.4 mmol), palladium (II) acetate (0.04 g, 0.16 mmol), tri-(*ortho*-tolylphosphine) (0.10 g, 0.33 mmol) and triethylamine (4.92 g, 48.78 mmol) was prepared in a thick-walled screw-cap glass tube. The tube was capped under argon and heated for 24 h at 120°C. After cooling the mixture it was extracted with ethyl acetate. The organic layer

was washed with saturated NaCl, water and dry $MgSO_4$. After filtration and evaporation of the solvent the solid crude was recrystallized from hexane to produce fine transparent crystals (Yield= 65 %).

^{1}H NMR (300 MHz, $CDCl_3$): δ= 7.51-7.54 (m, 4H; Ar-H), 7.34-7.39 (m, 8H; Ar-H), 7.27-7.30 (m, 2H; Ar-H), 6.82-6.83 (d, 2H; vinyl), 2.32 (d, 6H; -CH_3).

Formation of Nanoparticles. PPB nanoparticles were prepared by a simple reprecipitation method.[7] Water played a role of precipitating solvent for PPB in THF. Volume fractions of water were added up to 80%, with vigorous stirring at 300 K. Distilled water and THF were filtered with a membrane filter with pore size 0.2 μm. In all samples solutions (mixtures), the concentration of chromophore (2.9×10^{-5} mol L^{-1}) was constant after addition of distilled water. After 60% volume fraction of water addition, aggregation of PPB in the mixed solution produced nanosize particles. These suspensions were homogenous and stable, for several months. Samples for powder and SEM tests were prepared by dropping the sample onto a glass substrate (for powder XRD) or a carbon tape (for SEM) and dried at room temperature. To accumulate sufficient sample, this process was repeated several times.

2.2.2 Syntheis of Distyrylbenzene (DSB) (2):

1,4-dibromobenzene (5 g, 21.2 mmols), styrene (6.6 g, 63.5 mmols), P(*o*-tolyl)$_3$ (0.5 g, 1.7 mmols), K_2CO_3 (8.78 g, 63.5 mmols) and Bu_3N (0.78 g, 4.2 mmols) were taken in a round bottom flask containing about 25 mL deionized water. The reaction mixture was stirred and heated at about 100^{o}C for one day. The color of the solution formed was brown. The reaction

mixture was acidified with dilute HCl and was extracted with ethyl acetate and washed with water and saturated NaCl. The organic layer was dried over $MgSO_4$ and the solution was filtered and solvent was removed on rotar. After keeping at high vacuum overnight yellowish solid formed, which on recrystallization from warm chloroform gave greenish white fluppy crystals (Yield= 67%).

^{1}H NMR (300 MHz, $CDCl_3$): δ= 7.54 (d, 8H; Ar-H), 7.35-7.32 (t, 4H; Ar-H), 7.24 (m, 2H; Ar-H), 7.10 (s, 4H; vinyl).

2.2.3 Synthesis of CN-DSB (3):

CN-DSB was synthesized by Knoevenagel reaction. Typically, KOH (4.2 g, 75.14 mmols) was added to a solution of terephthaladehyde (5.0 g, 37.20 mmol) and phenylacetonitrile (8.8 g, 75.14 mmol) in ethanol (50 mL). A greenish yellow gel-type mixture was formed immediately after addition. The resulting solution was stirred for overnight at room temperature. The mixture was then filtered and washed several times by ethanol. The crude was recrystallized from chloroform to give greenish yellow solid (Yield= 45%).

^{1}H NMR (300 MHz, $CDCl_3$): δ= 7.93 (s, 4H; Ar-H), 7.66-7.63 (m, 4H; Ar-H), 7.49 (s, 2H; Ar-H), 7.41-7.38 (m, 4H; Ar-H), 7.19 (s, 2H; vinyl); m.p. 270-272^{o}C.

Formation of Nanostructures. CN-DSB nanostructures were obtained by a simple reprecipitation method. Water served as a precipitating solvent for CN-DSB in THF. Volume fractions of water were added up to 90%, with vigorous stirring at 296 K. Distilled water and THF were filtered with a membrane filter (pore size 0.2μm). In all these samples (mixtures), the

concentration of chromophore (3.6×10^{-5} mol L^{-1}) was constant after addition of distilled water. To see the concentration dependence on the nanostructures formation of CN-DSB, another series with different concentrations, viz. 1.8 x 10^{-5}, 3.6×10^{-5}, and 7.2×10^{-5} mol L^{-1} was prepared. These suspensions were homogenous and stable. Samples for SEM tests were prepared by dropping the sample mixture onto a microscopic glass or carbon tape and dried under vacuum.

Preparation of PMMA Thin Film and Single Crystal Thin Film. CNDSB was dissolved in $CHCl_3$ and mixed with PMMA at the w/w ratio of 1:1000. After the stock solution was prepared, the mixture of 1:1000 CNDSB/PMMA solutions was spin-coated on quartz. Single crystal film was prepared for UV-visible measurement by grinding the single crystal into powder, and uniformly spreading on quartz.

2.2.4 Synthesis of OPV Derivative with Long Alkyl Side-Chain (DSB-C8):

1,4-Diiodo-2,5-dimethoxybenzene (4):

1,4-dimethoxybenzene (3 g, 21.7 mmols), iodine crystals (5.5 g, 21.7 mmols), HIO_3 (2.3 g, 13.0 mmols) and sulphuric acid (30%, 5 mL in water) were taken together in round bottom flask. A mixture of solvents carbon tetrachloride and acetic acid were added in 1:2 proportion by volume (here 5 mL:10 mL). The reaction mixture was stirred and refluxed (70^oC) for one day and monitored the conversion by TLC. After stopping the reaction, mixture was filtered. The residue was treated with dichloromethane, aqueous $N_2S_2O_7$, saturated NaCl, organic layer dried over $MgSO_4$ and filtered. The

solvent was removed on rotavap and the solid crude was recrystallized from chloroform to give 1,4-diiodo-2,5-dimethoxybenzene **4**. (Yield= 78%).

^{1}H NMR (300 MHz, $CDCl_3$): δ= 7.19 (s, 2H; Ar-H), 3.82 (s, 6H; O-CH_3).

2,5-Diiodo-1,4-benzenediol (5):

Compound **4** (1 g, 2.5 mmols) was dissolved in dry CH_2Cl_2 solution and stirred at -15^{o}C under nitrogen atmosphere. Then added 1.7 mL of BBr_3 dissolved in 1 M CH_2Cl_2 (0.42 g, 1.7 mmols) slowly. Reaction was completed after about 6 hours. The mixture was extracted with water/ CH_2Cl_2, saturated NaCl, organic layer dried over $MgSO_4$, filtered. The solvent was evaporated on rotar and the solid crude obtained was recrystallized from EA/Hexane mixture to give crystals of **5** (Yield= 55%).

1-[2,5-Diiodo-4-(octyloxy)phenoxy]octane (6):

Compound **5** (2 g, 5.5 mmols), K_2CO_3 (1.6 g, 13.7 mmols) were mixed in ~ 50 mL of dimethylformamide (DMF). Solution was turned reddish and then added n-octyl bromide (1-bromo octane) (2.75 g, 11 mmols). The mixture was stirred and heated at ~70^{o}C for about 3 h and then poured in water, acidified by dilute HCl. It was extracted with EA/water, washed with saturated NaCl, organic layer was dried over $MgSO_4$, filtered and solvent was evaporated on rotavap to get solid which was purified by recrystallization from EA/Hexane to give **6** (Yield= 83%).

1,4-Di(octyloxy)-2,5-di[(*E*)-2-phenyl-1-propenyl]benzene (DSB-C8) (7):

α-methyl styrene (0.6 g, 5 mmols), compound **6** (1 g, 1.7 mmols), $Pd(OAc)_2$ (0.008 g, 0.034 mmols), P(*o*-tolyl)$_3$ (0.02 g, 0.7 mmols) and triethylamine (10 mL) were taken in a screw cap hard glass tube. Argon gas

purged into it and the tube was heated on oil-bath at about 130°C for 3 days. The mixture formed a greenish gel. Then it was filtered and triethylamine was evaporated on rotar. After the work-up, the crude liquid was formed which solidified at high vacuum. The compound was separated on column (blue fraction- it is highly fluorescent under UV) using hexane as eluent to give yellowish green solid DSB-C8 (**7**) (Yield= 76%).

^{1}H NMR (300 MHz, $CDCl_3$): δ= 7.57-7.54 (d, 4H; Ar-H), 7.39-7.34 (t, 4H; Ar-H), 7.30-7.24 (t, 2H; Ar-H), 6.98 (s, 2H; vinyl), 6.91 (s, 2H; Ar-H), 3.98-3.94 (t, 4H, O-CH_2), 2.29 (s, 6H, vinyl CH_3), 1.78 (m, 4H, -CH_2-), 1.46 (m, 4H, -CH_2-), 1.40-1.20 (m, , -CH_2-), 0.8-1.0 (m, 6H, -CH_3).

Formation of Nanostructures of DSB-C8: DSB-C8 nanostructures were obtained by a simple reprecipitation method. Water served as a precipitating solvent for CN-DSB in THF. Volume fractions of water were added up to 90%, with vigorous stirring at 296 K. Distilled water and THF were filtered with a membrane filter (pore size 0.2μm). In all these samples (mixtures), the concentration of DSB-C8 chromophore (3.5×10^{-4} mol L^{-1}) was constant after addition of distilled water.

2.2.5 Synthesis and Formation of HPS nanostructures (8):

1,1,2,3,4,5-Hexaphenylsilole (HPS) was synthesized according to a published procedure.[25] HPS nanostructures were obtained by a simple reprecipitation method, in which water served as a precipitating solvent for HPS in THF. Solutions with volume fractions 0, 50, 60, 70, 80 and 90% of water were prepared and stirred vigorously for an hour before spectral measurements. Distilled water and THF were filtered with a membrane filter

(pore size 0.2 μm). In all samples, the concentration of HPS in THF solution was 1.9 x 10^{-5} mol L^{-1} after addition of distilled water. The resulting suspensions after water addition were homogeneous.

^{1}H NMR (300 MHz, $CDCl_3$): 7.66 (m, 4H), 7.37 (m, 6H), 7.01-6.83 (m, 20H).

FT-IR (KBr): 3055, 3024, 1597, 1485, 1441, 1298, 1111, 1074, 1027, 790, 764, 741, 713, 697, 509 cm^{-1}. Mp = 186-187^{o}C

2.2.6 Amino-stilbene Compounds and their Nanostructures Formation (9-12):

We studied the nanoparticles formation of amino-stilbene compounds (shown below) and observed their steady-state UV-visible spectra and SEM images. These are having electron-donating (-OMe and -H) and electron withdrawing (-CF_3 and -CN) groups. Initially, stock solutions of all these compounds in 5 mL THF were prepared with constant concentration of 1.66 x 10^{-3} M. In all 10, 9, 12.5 and 9.8 mg of amino-stilbenes (with –OMe, -H, -CF_3 and –CN groups, respectively) were dissolved in 5 mL THF each and then certain amounts were injected through microsyringe into THF or water as required. Thus nanodispersions of these compounds in water were formed.

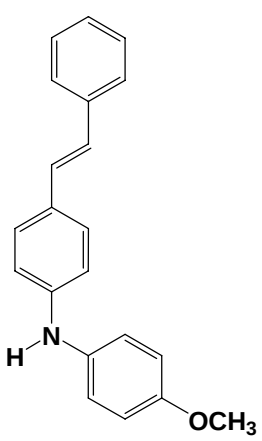

(9)

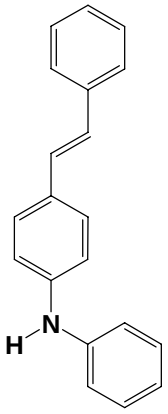

(10)

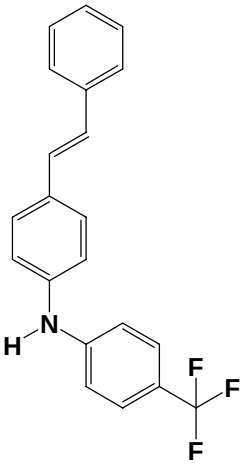

(11)

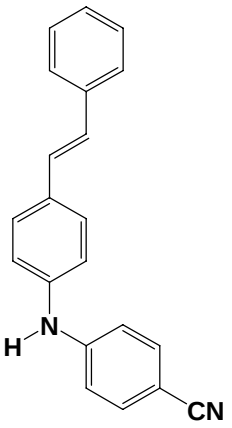

(12)

2.2.7 Synthesis of rod-coil molecules:

The synthesis of rod-coil molecules containing poly(ethylene oxide)s with various degrees of polymerization was performed as outlined in the Schemes 2.6 and 2.7. The appropriate poly(ethylene oxide) reacted with *p*-iodo phenol (Mitsunobu Reaction) to produce an intermediate which in turn reacted with 1-[(*E*)-2-phenyl-1-ethenyl]-4-vinylbenzene to give oligophenylene vinylene (OPV) derivative as a rod segment and poly(ethylene oxide)s as coil segment.

4[(*E*)-2-phenyl-1-propenyl] aniline (13):

p-iodoaniline (5 g, 22.8 mmols), α-methyl styrene (4.04 g, 34.2 mmols), $PdCl_2$ (0.04 g, 1 mol%), P(*o*-tolyl)$_3$ (0.277 g, 0.912 mmols), K_2CO_3 (4.72 g, 34.2 mmols) were taken in a three-necked round bottom flask. N, N-Dimethylformamide (DMF) and water in proportion of 1:2.5 by volume was used as solvent system. The mixture was heated at about 100^{o}C for one day. The black solution formed was extracted with ethyl acetate, water, saturated NaCl and organic layer was dried over $MgSO_4$. The solvent was removed on

rotavap to get solid crude. The product was purified by the recrystallization of the crude from ethyl acetate/hexane mixture. Brownish crystals were formed (Yield- 85%). ^{1}H-NMR(300 MHz, $CDCl_3$, δ, ppm) : 7.50-7.47 (m, 2H, Ar-H), 7.36-7.30 (m, 2H, Ar-H), 7.26-7.21 (m, 3H, Ar-H), 7.17-6.62 (m, 2H, Ar-H *ortho* to $–NH_2$, 1H, *ortho* to –CH), 3.90-3.40 (s, 2H, $-NH_2$), 2.26 (d, 3H, $-CH_3$),

1-Iodo-4-[(E)-2-phenyl-1-propenyl]benzene (14):

Compound **13** (4.0 g, 19.2 mmols) was taken in a round bottom flask and dissolved in concentrated H_2SO_4 (5.6 g, 57.36 mmols), stirred for some time and kept in ice bath. Then was added cooled solution of $NaNO_2$ (1.70 g, 24.8 mmols) in water to the above mixture to form the diazonium salt of the compound. The clear solution was obtained and bubbling was observed. The aqueous solution of KI (4.11 g, 4.11 mmols) was then added dropwise. Stirring continued for an hour. The mixture was then heated at about 65^{o}C for one hour, cooled down and treated with aqueous $Na_2S_2O_3$ to neutralize excess KI, extracted with ethyl acetate, water, saturated NaCl, dried over $MgSO_4$ and filtered. After removing solvent on rotar red solid crude was obtained. The product was purified by column chromatography using hexane as an eluent. White solid was obtained (Yield= 54%).

^{1}H-NMR(300 MHz, $CDCl_3$, δ, ppm) : 7.68-7.65 (t, 2H, Ar-H), 7.49-7.47 (t, 2H, Ar-H), 7.35-7.32 (m, 4H, Ar-H), 7.09-7.06 (d, 1H, Ar-H), 6.70 (s, 1H, -CH), 2.23 (d, 3H, $-CH_3$).

1-[(*E*)-2-phenyl-1-propenyl]-4-[(*E*)-1-propenyl] benzene (16):

Compound **14** (1.0 g, 4.27 mmols) was reacted with isopropenylmagnesium bromide (**15**) (9 mL in 0.5 M THF) under absolutely

dry conditions. $PdCl_2$ (0.015 g, 0.084 mmols) was used in catalytic amount. Dry THF was used as a solvent. The reaction was carried out at 0^oC under nitrogen atmosphere. Isopropenylmagnesium bromide was added very slowly. Monitored the reaction by TLC and stirred for about 5 hours. After 5 hours, the reaction was quenched by adding few drops of water. THF was removed on rotar, extracted with CH_2Cl_2, water, saturated NaCl, dried over $MgSO_4$ and filtered. After removing solvent on rotavap, reddish solid crude was obtained. The product was separated on column by hexane. The white solid product was obtained (Yield= 40%).

^{1}H-NMR (300 MHz, $CDCl_3$, δ, ppm) : 7.54-7.47 (m, 4H, Ar-H), 7.46-7.32 (m, 5H, Ar-H), 6.82 (s, 1H, -CH), 5.41 (d, 1H, -CH), 5.08-5.09 (d, 1H, -CH), 2.35-2.25 (t, 3H, $-CH_3$), 2.20-2.15 (t, 3H, $-CH_3$).

Iodobenzene-PEG (n = 8, 17, 45) (18a-c):

Iodophenol (6 g, 27.2 mmols), poly(ethyleneglycol methyl ether) with ethylene glycol repeat units n = 8 (**17a**) (11.5 g, 30.0 mmols), PPh_3 (8.6 g, 32.7 mmols) were taken in a round bottom flask. To it was added about 40 mL dry THF and stirred in an ice-bath. To this solution was added diisopropyl azodicarboxylate (DIAD) (7.2 g, 35.4 mmols) slowly. Then after removing ice-bath stirred the reaction mixture overnight. THF was removed on rotavap. Added little EA and hexane and triturated and kept for cooling in the refridgerator. The solid formed may be of oxide of PPh_3 and discarded. Repeated this procedure of crystallization several times to get the filtrate, concentrated it and kept under high vacuum to finally yield the desired compound **18a**. The similar procedure was followed for the reactions involving poly(ethylene glycol methyl ether) with repeat units n = 17 (**17b**)

and 45 (**17c**). The compounds **18a** and **18b** were liquid, yellow and brownish respectively; whereas **18c** was solid.

18a: ^{1}H-NMR (300 MHz, $CDCl_3$, δ, ppm) : 7.47-7.44 (d, 2H, Ar-H), 6.63-6.60 (d, 2H, Ar-H), 4.02-3.63 (m, 32 H, -CH_2-CH_2-O), 3.29 (s, 3H, -CH_3).

18b: ^{1}H-NMR (300 MHz, $CDCl_3$, δ, ppm) : 7.55-7.52 (d, 2H, Ar-H), 6.71-6.68 (d, 2H, Ar-H), 4.10-3.53 (m, 68 H, -CH_2-CH_2-O), 3.38 (s, 3 H, -CH_3).

18c: ^{1}H-NMR (300 MHz, $CDCl_3$, δ, ppm) : 7.52-7.49 (d, 2H, Ar-H), 6.68-6.65 (d, 2H, Ar-H), 4.06-3.50 (m, 180 H, -CH_2-CH_2-O), 3.30 (s, 3H, -CH_3).

PPB-PEG (n = 8, 17, 45) (19a-c):

Compounds **19a-c** were obtained by Heck coupling. Typically, compounds **16** (0.4 g, 0.8 mmols), **18a** (1 g, 0.7 mmols), $Pd(OAc)_2$ (0.003 g, 0.007 mmols), P(*o*-tolyl)$_3$ (0.008 g, 0.014 mmols) were mixed in triethylamine (about 3.5 mL) solution and stirred in a screw-capped hard glass tube at around 85^{o}C. Within an hour solution became greenish in color. Stopped heating after 2.5 days. Triethylamine was removed on rotar, extracted the mixture with EA, water, saturated NaCl, dried over MgSO4 and filtered. EA was removed on rotar to get yellow viscous liquid which under high vacuum solidified. It was heated in EA/hexane. After decantation and cooling several times desired (**19a**) pale white solid was formed (Yield= 55%). The similar procedure was followed for the compounds **19b-c** using **18b-c**.

19a: ^{1}H-NMR (300 MHz, $CDCl_3$, δ, ppm) : 7.50-7.47 (m, 4H, Ar-H), 7.35-7.25 (m, 5H, Ar-H), 7.25-7.20 (m, 4H, Ar-H), 6.90-6.85 (d, 1H, vinyl –CH), 6.76 (s, 1H, vinyl –CH), 4.15-3.50 (m, 32 H, -CH_2-CH_2-O), 3.30 (d, 3H, O–CH_3), 2.25-2.20 (s, 6H, vinyl –CH_3).

19b: ^{1}H-NMR (300 MHz, $CDCl_3$, δ, ppm) : 7.52-7.48 (m, 4H, Ar-H), 7.40-7.32 (m, 5H, Ar-H), 7.32-7.25 (m, 4H, Ar-H), 6.90-6.85 (d, 1H, vinyl –CH), 6.82 (s, 1H, vinyl –CH), 4.15-3.50 (m, 68 H, -CH_2-CH_2-O), 3.35 (d, 3H, O–CH_3), 2.35-2.25 (s, 6H, vinyl –CH_3).

19c: ^{1}H-NMR (300 MHz, $CDCl_3$, δ, ppm) : 7.58-7.50 (m, 4H, Ar-H), 7.45-7.35 (m, 5H, Ar-H), 7.35-7.20 (m, 4H, Ar-H), 6.95-6.90 (d, 1H, vinyl –CH), 6.85 (s, 1H, vinyl –CH), 4.20-3.45 (m, 180 H, -CH_2-CH_2-O), 3.38 (d, 3H, O–CH_3), 2.60-2.18 (s, 6H, vinyl –CH_3).

1,4-Di[(*E*)-2-phenyl-1-ethenyl]benzene (20):

Bromo-styrene (10g, 54.6 mmols), styrene (8.5 g, 82 mmols), triethylamine (16.5 g, 164 mmols), $Pd(OAc)_2$ (0.12 g, 0.55 mmols) and P(*o*-Tolyl)$_3$ (0.33 g, 1.1 mmols) were taken together in a hard glass screw cap tube. Argon gas was purged through it and the tube was heated at about 100^{o}C. Within few minutes the greenish gel was formed. Heating continued for one day. Then reaction mixture was extracted with water, ethyl acetate and then the organic layer was washed with saturated NaCl and dried over $MgSO_4$. The solvent was removed on rotar and the soild crude was obtained. Recrystallization several times to ensure the purity, gave yellow solid compound **20** (Yield= 57%). ^{1}H NMR

DSB-PEG (n = 8) (21):

Compound **20** (0.23 g, 1.1 mmols), **18a** (0.5 g, 0.85 mmols), triethylamine (3.0 g, 30 mmols), $Pd(OAc)_2$ (0.02 g, 0.009 mmols) and P(*o*-Tolyl)$_3$ (0.005 g, 0.017 mmols) were taken together in a hard glass screw cap tube. Argon gas was purged through it and the tube was heated at about 100^{o}C. Within few minutes the greenish gel was formed. Heating and stirring stopped after 10 h. Then reaction mixture was extracted with water, ethyl acetate and then the organic layer was washed with saturated NaCl and dried over $MgSO_4$. The solvent was removed on rotar and the soild crude was obtained. Recrystallization from EA/Hexane gave yellowish solid **21** (Yield= 57%).

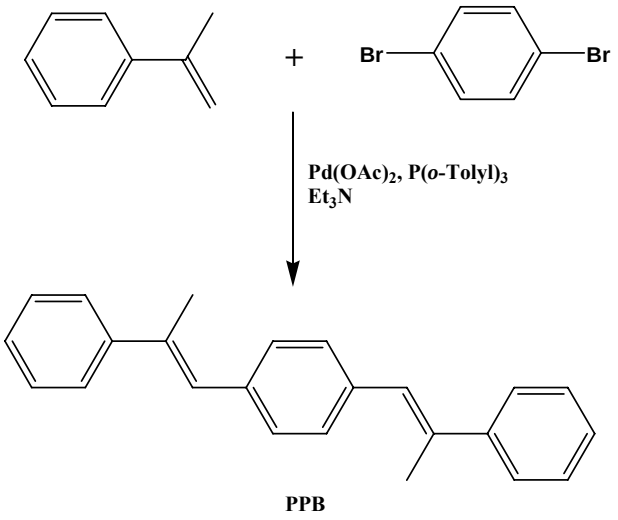

PPB (1)

Scheme 2.1- Synthesis of PPB (1)

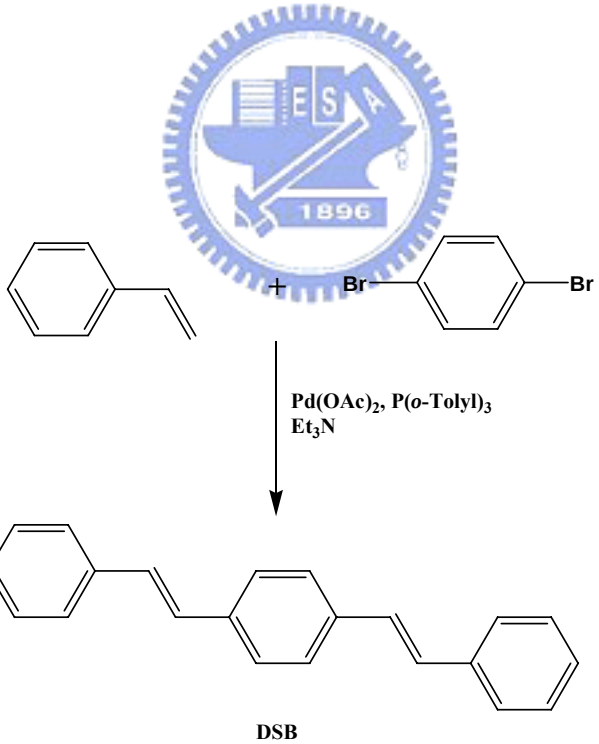

DSB (2)

Scheme 2.2- Synthesis of DSB (2)

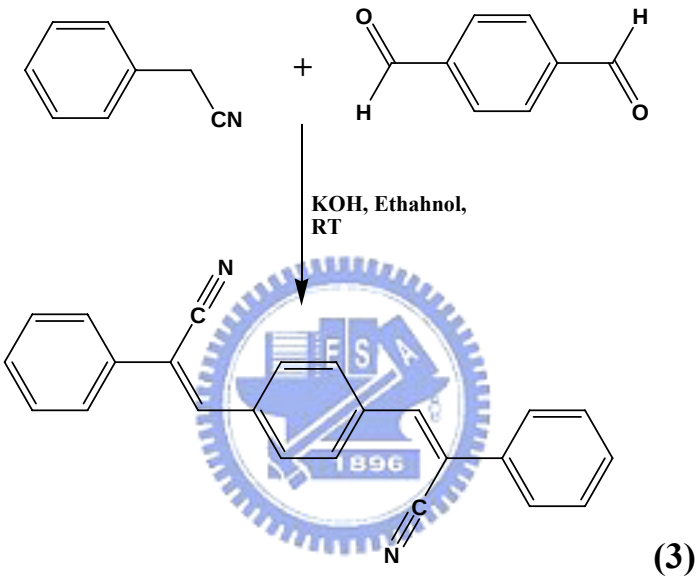

(3)

Scheme 2.3- Synthesis of CN-DSB (3)

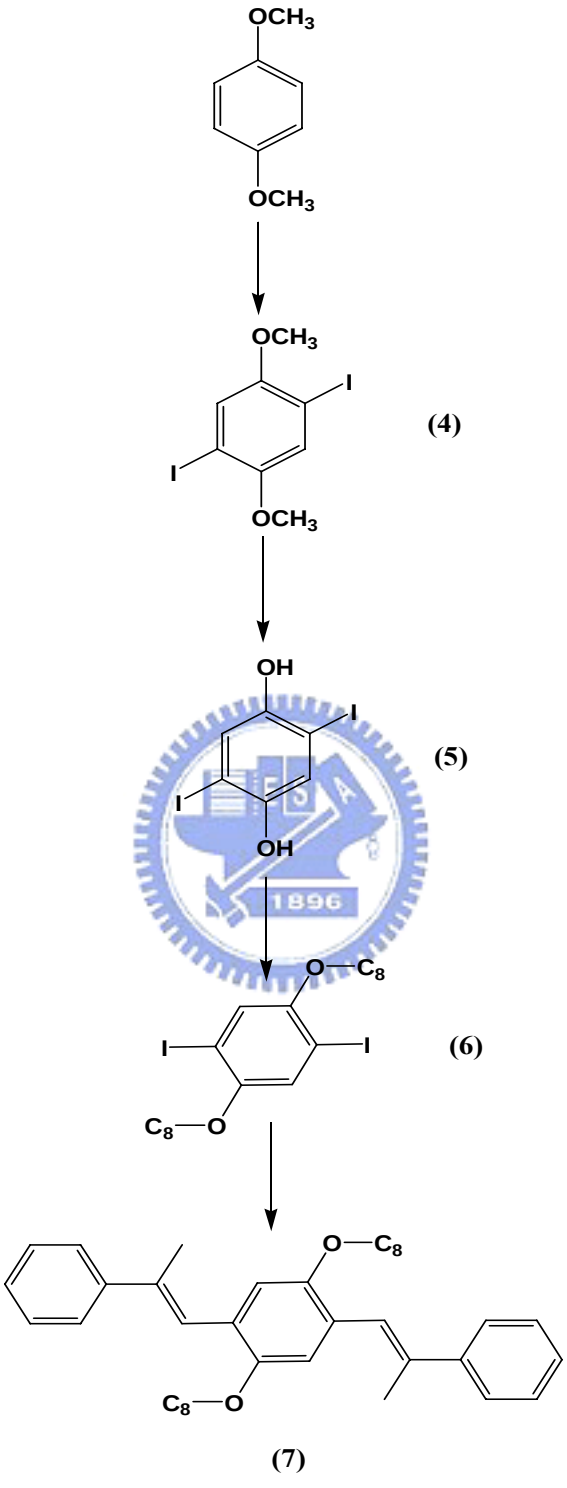

Scheme 2.4- Synthesis of DSB-C8

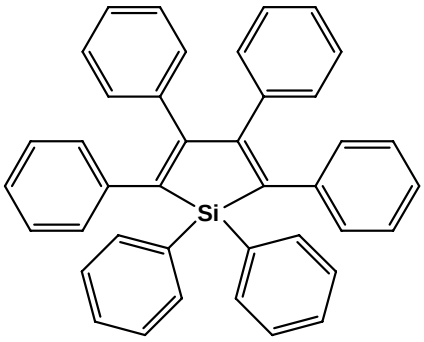

Scheme 2.5- Hexaphenyl Silole (HPS) (8)

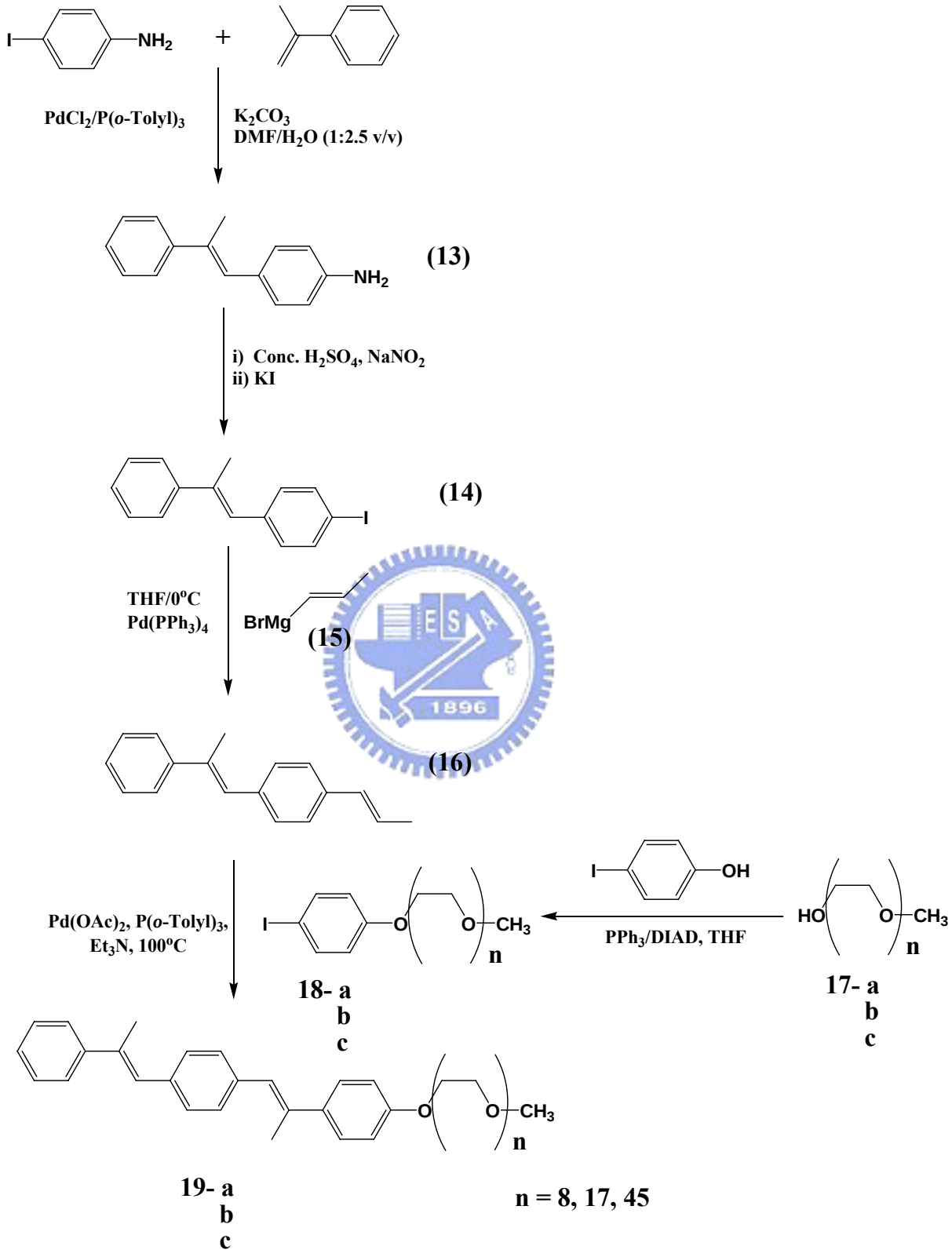

Scheme 2.6- Synthesis of OPV rod-coil molecules-I

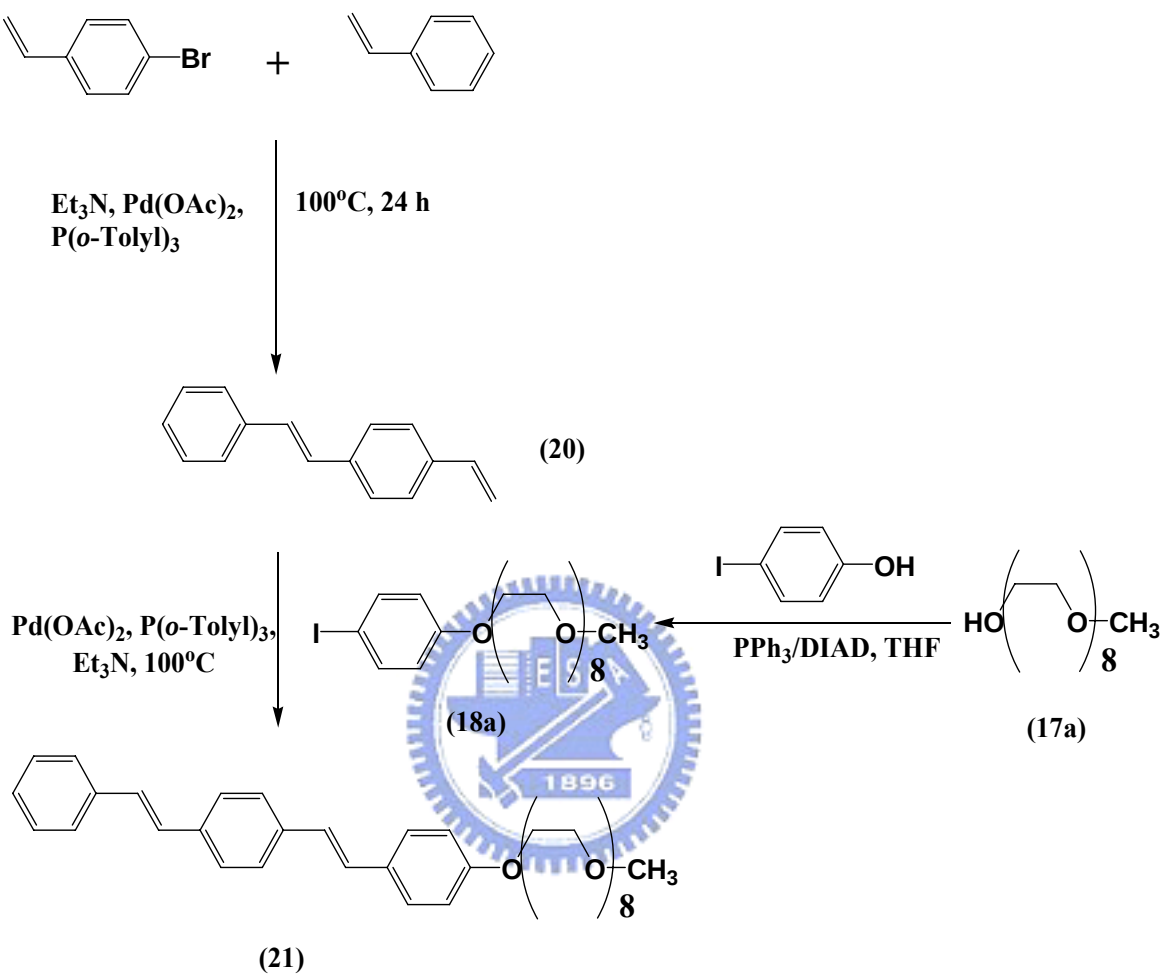

Scheme 2.7 Synthesis of OPV rod-coil molecules-II

Chapter 3

Results and Discussion

In this research work, we report, in details, synthesis and the size and nanostructure-dependent optical properties of conjugated organic compounds- 1,4-di[(*E*)-2-phenyl-1-propenyl]benzene (PPB), (Z)-3-[4-(z)-2-cyano-2-phenyl-1 ethenyl] phenyl}-2-phenyl-2-propenenitrile (CN-DSB), DSB-C8 and hexaphenylsilole (HPS), Amino-stilbene derivatives and some of the rod-coil molecules with oligophenylenevinylene (OPV) derivatives as rod segments. The purpose of the research reported here was to investigate the photophysical properties, nature of the excited states in isolated molecule, nanostructures and/or bulk crystals.

3.1 1,4-Di[(*E*)-2-phenyl-1-propenyl]benzene (PPB):

Here, we describe about the preparation of the fluorescent organic nanoparticles of 1,4-di[(*E*)-2-phenyl-1-propenyl]benzene (PPB) that belongs to the family of oligophenylenevinylenes (OPV) with two methyl groups added to the 1,4-distyrylbenzene (DSB) skeleton (as shown below).

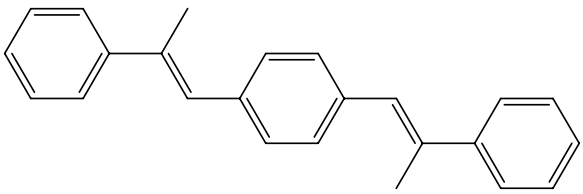

Synthesis and Characterization: 1,4-Di[(*E*)-2-phenyl-1-propenyl]benzene (PPB) was synthesized according to Heck coupling method. Proton Nuclear

Magnetic Resonance spectrum for the PPB is shown in the following Figure 3.1.

Preparation of Fluorescent Organic Nanoparticles: PPB nanoparticles were prepared by a simple reprecipitation method.[7] In this method, initially a stock solution of PPB in THF is prepared. Then a specific amount of the solution is taken from this stock and diluted with THF solvent and kept for stirring at room temperature. The desired amount of distilled water (filtered through 0.2 micrometer pore membrane) was added immediately and at once into the above solution while still strirring. The stirring was continued for one hour. Then all measurements were taken after that. When nanoparticles were formed the solution suspension looked intense bright under UV lamp.

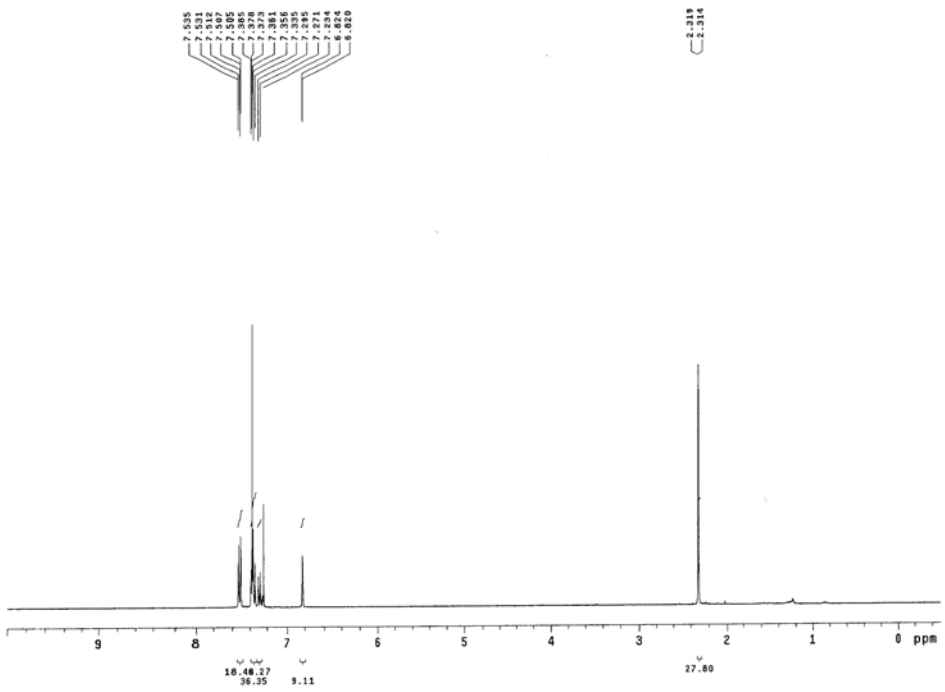

Figure 3.1 ^{1}H NMR Spectrum of PPB

We observed that fluorescent emission from PPB nanoparticles is very intense whereas PPB itself is non-fluorescent in dilute solution. Despite the similarity of chemical structure between PPB and DSB, free DSB in solution is strongly fluorescent but its nanoparticles show weak emission like that of DPST[9] As UV absorption spectra of PPB nanoparticles are blue-shifted relative to their spectrum in solution and shows a strong emission in the solid state.

To get the further understanding of this unusual phenomenon, we have investigated, in collaboration with Prof. E. W.-G. Diau's group, the dynamics of relaxation from excited states and undertaken structural identification of free PPB and its nanoparticles using techniques such as UV-vis and PL, field-emission scanning electron microscopy (SEM), femtosecond (fs) and picosecond (ps) time-resolved fluorescence dynamics, and X-ray diffraction (XRD). Two emissive states in PPB nanoparticles were identified in the ps fluorescence transients and confirmed through powder XRD measurements wherein we observed two distinct packing structures. The emission enhancement from PPB nanoparticles relative to its THF solution reflects a geometrical change from a twisted conformation to a nearly planar one so as to form a herringbone-type aggregation with an edge-to-face feature shown in the single crystal structure of PPB.

3.1.1 Scanning Electron Microscopy of PPB Nanoparticles

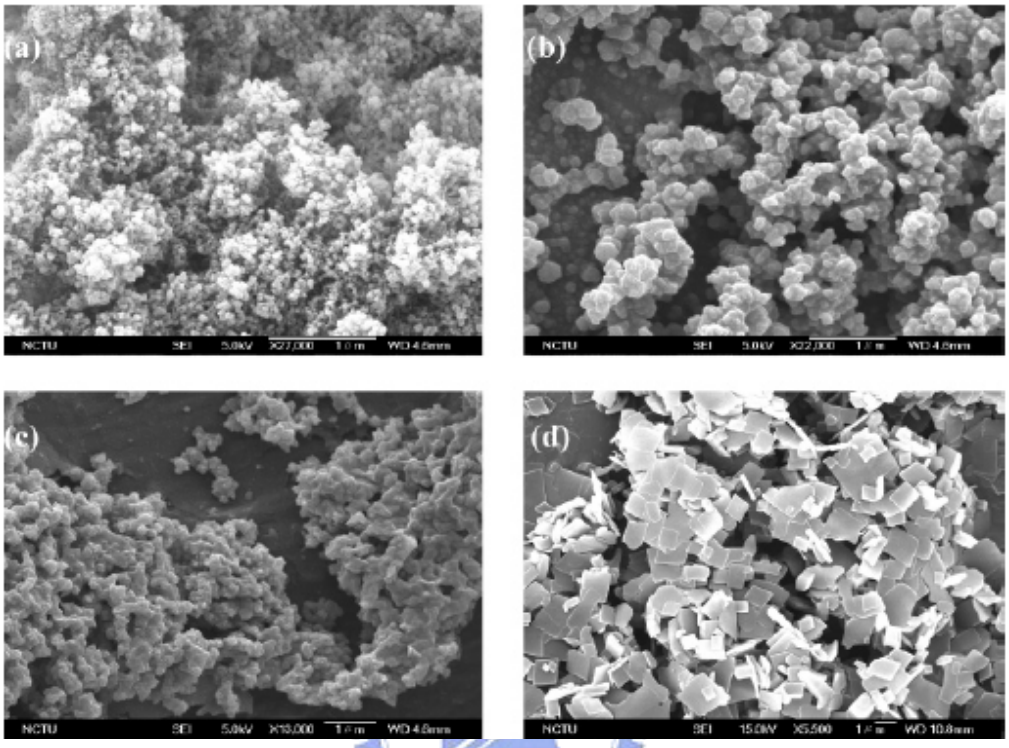

Figure 3.2 SEM images of PPB nanocrystals showing the size with average diameters, (a) 50, (b) 150, (c) 300 nm, and (d) ~ 1 μm for suspensions of nanoparticles containing 65, 70, 75, and 80% volume fractions of water added to THF, respectively.

PPB nanoparticles in a series were prepared according to a simple reprecipitation method with THF as solvent and water as non-solvent with 0, 50, 55, 60, 65, 70, 75, and 80%. The nanoparticle suspension in the mixed solution appeared turbid when the volume fraction of added water exceeded 60%. The color of solutions deepened (became deep blue) on increase of the volume fraction of water from 65 to 80%, and the size of nanoparticles

increased with increased volume fraction of the water. Figure 3.2 presents SEM photographs of PPB nanoparticles with average particle size varying with water volume fraction of the solutions: (a) 50 nm at 65%, (b) 150 nm at 70%, (c) 300 nm at 75%, and (d) 1 m at 80%. According to the SEM images shown in Figure 3.2, the free molecules in the solution begin to aggregate at 65% volume fraction of water addition. The spherically shaped particles were formed initially as the superior solvent THF was replaced by the inferior solvent water, and dispersed in bulk water. The observed spherical shape of the nanoparticles likely results from minimization of interfacial energies between PPB and water molecules.[10] As the proportion of added water became greater than 65%, the size of PPB nanoparticles increased greatly, because the molecules aggregated to larger structures. This size-dependent feature indicates that nanocrystallization of PPB proceeds as the volume fraction of water in the solution increases because the water-insoluble PPB molecules aggregate at large water fractions. At 80% water volume fractions, larger particles (size 1 m) were found, and their shape became rectangular (Figure 3.1D). This formation of rectangular microparticles in 80% solution likely reflects a competition between anisotropic growth and spherical aggregation and is similar to a case involving the one-dimensional nanostructures of *p*-BSP in mixtures of water and THF.[10] The size-dependent optical properties of PPB nanoparticles differ from those reported previously.[10,8]

3.1.2 Absorption and Photoluminescence Spectroscopy

UV–visible absorption spectra and the corresponding emission spectra of PPB with various volume fractions of added water are shown in Figure 3.3. The UV–vis spectra (Figure 3.3a) show strong absorption with a maximum

at 314 nm in solutions of 0–65% water volume fraction. At 70% solution, the absorbance at 314 nm decreases significantly, and a shoulder appears on the blue side of the feature. An additional absorption at 273 nm appears at 75% solution and becomes more prominent at 80% solution. With the increase of water volume fraction beyond 70%, absorbance at 314 nm markedly decreased and another absorption building at 273 nm implies the formation of PPB nanoparticles at larger volume fractions of water. We observed a significantly enhanced fluorescent emission of PPB nanoparticles. Emission of PPB at 0–60% water volume fractions was scarcely detectable, indicating the almost nonfluorescent nature of free PPB molecules in dilute solution. The emission spectrum for a solution in THF features a continuous broad line with a maximum near 406 nm (Figure 3.3b), with 5-times enlargement. All other emission spectra with a water volume fraction less than 60% have similar shape and intensity. Above 60% water volume fraction addition, PPB nanoparticles with two new spectral features are formed and can be described in comparison with the emission spectrum of PPB in THF solution.

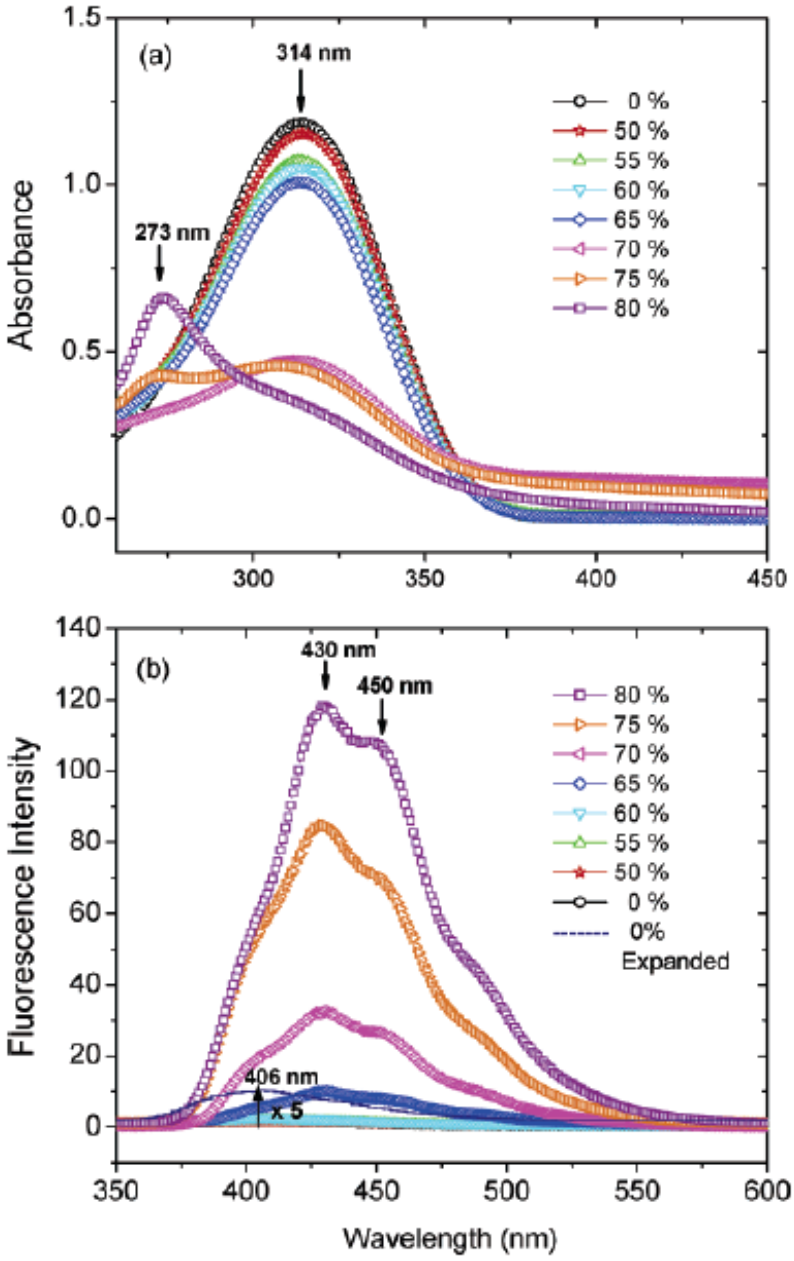

Figure 3.3 (a) UV-Vis absorption and (b) Photoluminescence spectra of PPB at various mixtures of water and THF.

Emission spectra of PPB for a volume fraction of water between 65 and 80% are distinctly shifted to a greater wavelength (maximum near 430 nm) with

an evident vibrational structure. Although the observed red-shifted emission spectra had a similar shape, a substantially enhanced intensity was found for spectra of PPB in 65–80% solutions. The emission became highly intense, as the nanoparticles became larger for volume fractions of added water above 65% (Figure 3.3b). Because this observed intensity systematically increases as a function of volume fraction of added water, we conclude that formation of PPB nanoparticles produces this enhanced emission. The larger the particle is, higher is the intensity of emission. This observed phenomenon of enhanced fluorescence of PPB nanoparticles resembles that of CN-MBE nanoparticles where both intra- and intermolecular effects have been reported to explain this fluorescence enhancement. An intramolecular effect generally implies that free, separated molecules with a twisted conformation in solution undergo efficient relaxation via a nonradiative channel, whereas molecules in planar conformations in the solid state suppress deactivation channel. An intermolecular effect arises from interactions between molecules when molecular aggregations become more significant. This effect strongly depends on the geometry of the packing structure.

There are two types of aggregations: H- and J- Aggregations. According to a molecular exciton model, H-aggregates tend to accelerate nonradiative relaxation process because of strong -stacking interactions in the parallely aligned structure; and J-aggregates hinder the nonradiative process for molecules arranged in a head-to-tail direction. In this case, absorbance spectra of PPB nanoparticles show a distinct blue-shift (Figure 3.3a), which characteristically indicates formation of H-type aggregates. Our observation of enhanced fluorescence shown in Figure 3.3b is incomprehensible as a typical H-type aggregation as reported for DPST and DSB.

3.1.3 Picosecond Relaxation Dynamics of PPB Nanoparticles

Time-dependent measurements done by C.-W. Chang, of PPB in various mixed solutions in water and THF were performed using time-correlated single-photon counting (TCSPC) with excitation at λ_{ex} = 310 nm; typical results (λ_{fl} = 420 nm) are shown in Figure 3.4.

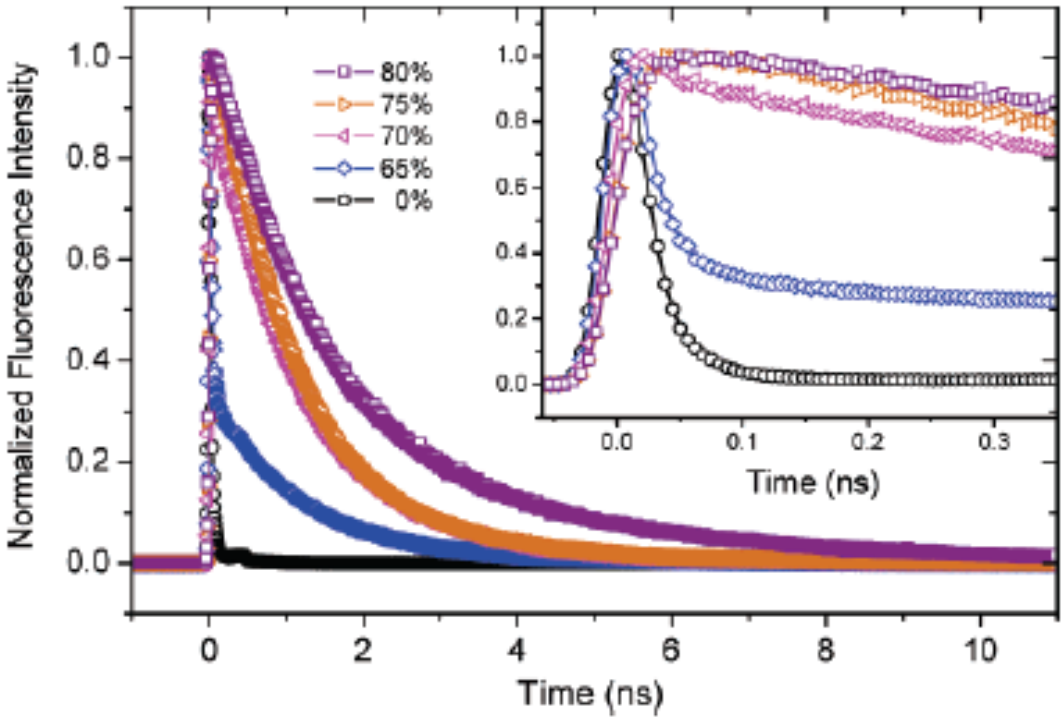

Figure 3.4 Picosecond fluorescent transients of PPB obtained on excitation for various mixtures of water and THF as indicated (λ_{ex} = 310 nm and λ_{fl} = 420 nm). Inset: corresponding transients on a subnanosecond scale. (Expts. by C.-W. Chang)

The fluorescence decay profiles (transients) of PPB in 0–60% water volume fractions are all characterized by a sharp spike. The transients for 50, 55, and 60% solutions are identical to that of THF solution, so did not show in Figure 3.4. The transient at the 65% solution contains two major parts: one

part shows a rapid decay and other shows a slow-decay character with a decay coefficient on a nanosecond time scale. At 70% volume fraction of water, the slow-decay part is a major component of the transient. When the water content was 75% and 80%, the contribution of the rapid decay became negligible and the slow decay became dominant in these transients. These observations indicate that formation of PPB nanoparticles led to formation of new components (the slow-decay part) in the fluorescence transients with much larger lifetimes of the excited state. Thus larger the nanoparticle is, the more significant the slow-decay part becomes. This feature is consistent with intensity enhancement observed in the corresponding steady-state fluorescence spectra (Figure 3.3b).

3.1.4 Molecular Structures of PPB

In collaboration with Prof. C.-S. Lee's group, the powder XRD pattern of a bulk PPB sample is obtained and is shown in Figure 3.5a. The observed strong reflections for each [00*l*] plane indicates a strongly preferred orientation due to the plate shape of the crystal, consistent with the calculated powder pattern when the effect of preferred orientation along [001] planes is taken into account. Powder XRD patterns of nanoparticles formed from varied water addition (65–80%) are shown in Figure 3.5b. A diffraction peak at $2\theta = 7.3°$ (d = 1.22 nm) was clearly observed in XRD data of all 65–80% samples. This additional feature indicates formation of nanoparticles in which PPB molecules arrange in three-dimensional packing of a new type.

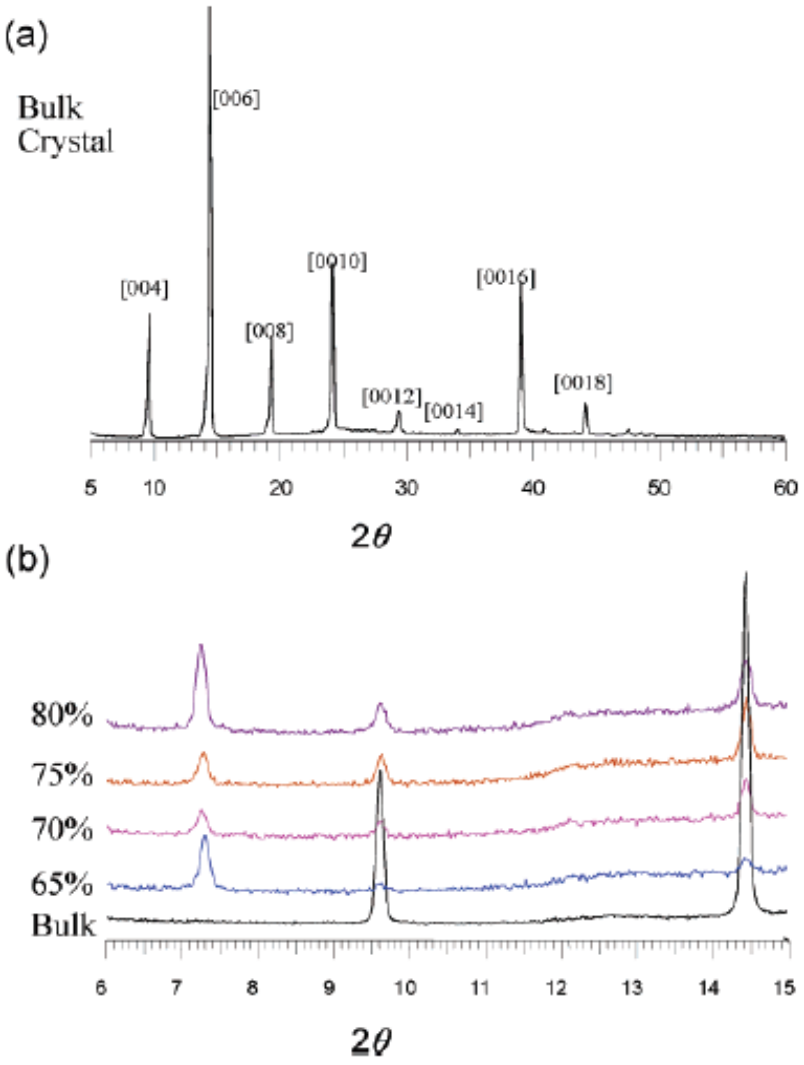

Figure 3.5 (a) Powder XRD pattern of PPB bulk material. (b) Powder XRD patterns of PPB nanoparticles from various mixtures of water and THF as indicated. (Expts. by C.-S. Lee)

The presence of diffraction features at both 2 . = 7.3 . and 2 . = 9.6 . and 14.5 . in the 65–80% samples indicates that water-induced PPB nanoparticles contain PPB in long-range packing structures of two types; one is the same as the bulk material, whereas the other is yet to be identified.

Single crystal of PPB was obtained on slow evaporation of its THF solution. There are four independent PPB molecules in a unit cell. The packing of PPB molecules along the *a*-axis shows a structure of herringbone type. This molecular packing feature is similar to that of chemically related compounds, e.g., DSB and other OPV.

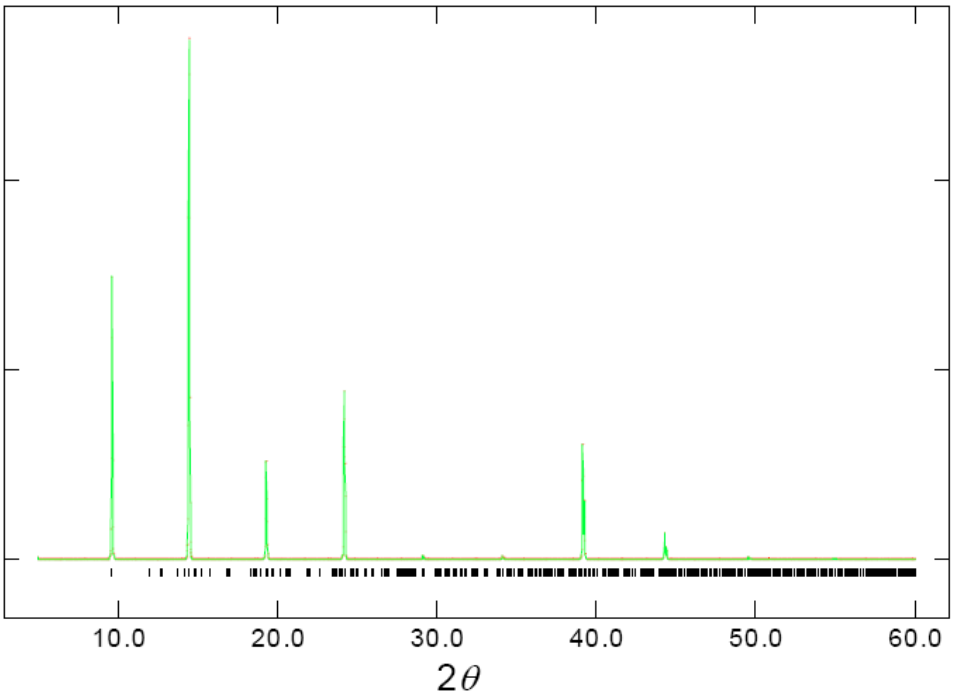

Figure 3.6 Calculated powder XRD pattern of PPB bulk crystal. The effect of preferred orientation is simulated by Dollase and March function at [001] direction.

The simulated pattern is consistent with the result from the powder XRD experiment of bulk PPB material when the effect of preferred orientation on the [001] direction is applied. For PPB, we observed strong fluorescence

from the aggregates. The pinwheel packing of PPB is affected to some extent by steric interference of methyl groups and by the “out-of-plane” nature of the ethene moiety with respect to the benzene rings.

The free DSB molecule has a planar geometry, with all atoms located in the same symmetry plane and the free PPB molecule has a nonplanar structure with one end benzene ring twisted from the molecular plane by 80 . The structure of the free PPB molecule differs markedly from that in a single crystal, in which three benzene rings in PPB align parallel to a symmetry plane similar to the planar geometry of the free DSB molecule. The twisted conformation of a free PPB molecule is essentially nonfluorescent in dilute solution; however the planar geometry of the three benzene rings in the PPB unit cell of aggregates produces strong emission in the solid state. This observed enhancement of emission from solutions of 65–80% water seems to be the due to conformational change of PPB molecules when aggregating to nano-size particles.

In brief, size-dependent optical properties of PPB nanoparticles were observed. These particles were prepared by reprecipitation in solutions of water and THF at various volume fractions and are characterized by SEM, UV-visible spectroscopy, XRD. We observed strong emission from PPB nanoparticles, but emission of free PPB in dilute solution was barely detectable. The fluorescent intensity of these nanoparticles increases with their size. Thus, PPB in dilute solution is nonfluorescent due to the twisted conformation; however, molecular planarity, geometrical rigidity, and loose packing produce strong fluorescent emission in PPB nanoparticles. A nearly planar geometry of molecules of PPB in the unit cell of a single crystal is confirmed by XRD measurements. Moreover, powder XRD experiments demonstrate that two packing structures are involved in PPB nanocrystals:

one forms aggregates according to a herringbone-type arrangement as observed in a single crystal, and other which could not be identified. The observed induction period of the emissive state likely reflects an involvement of solvent molecules inside the nanocrystal of the unknown structure. Thus, PPB exhibits weak emission in dilute solution but blue-shifted absorption and distinguishly strong red-shifted emission in nanoparticle aggregates. The enhanced emission of nanoparticles is due to the combined effects of a planar conformation and the formation of herringbone-type aggregates with an edge-to-face feature.

3.2 (Z)-3-[4-(z)-2-Cyano-2-phenyl-1 ethenyl] phenyl}-2-phenyl-2-propenenitrile CN-DSB:

Synthesis and Characterization:

CN-DSB was synthesized by Knoevenagel reaction. Proton Nuclear Magnetic Resonance Spectrum for CN-DSB is shown in the Figure 3.7.

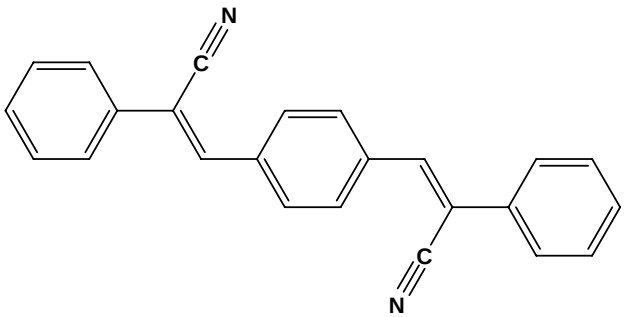

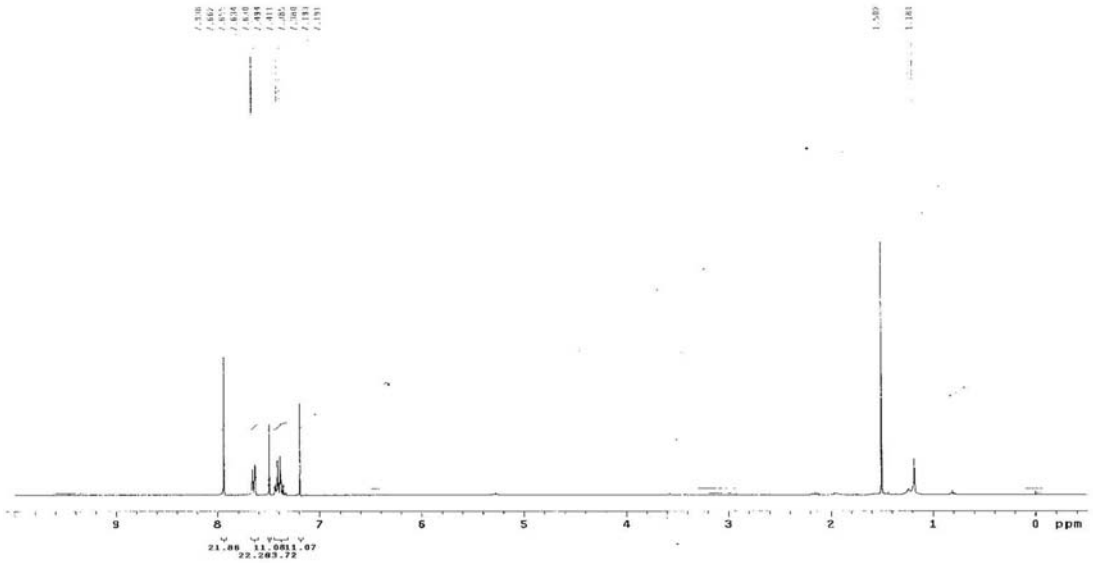

Figure 3.7 ^{1}H NMR Spectrum of CN-DSB

Formation of CN-DSB Nanostructures:

CN-DSB nanostructures were obtained by a simple reprecipitation method. Initially a stock solution of CN-DSB in THF is prepared. Then a specific amount of the solution is taken from this stock and diluted with THF solvent and kept for stirring at room temperature. The desired amount of distilled water (filtered through 0.2 micrometer pore membrane) was added immediately and at once into the above solution while still strirring. The stirring was continued for one hour. Then all measurements were taken after that. Scanning Electron Microscopy showed the formation of nanobelts for CN-DSB. When nanobelts were formed the solution suspension looked intense bright blue under UV lamp.

3.2.1 Scanning Electron Microscopy of CN-DSB Nanostrucures

Parts a, b and c in Figure 3.8 presents SEM photographs of CN-DSB nanostructures obtained by varying the percent volume water fractions in THF solution of CN-DSB; final concentration of solution being constant (3.6×10^{-5} M). Although the aggregation of the CN-DSB molecules might start at the early stages of the mixing, well-evolved nanostructures could be observed only after 70% of water addition. It is clear from SEM that free molecules in the solution aggregates to form curvy nanoparticles at 70% volume fraction of water addition as the good solvent (THF) was replaced by the poor solvent (water), and dispersed in bulk water. As the proportion of added water became greater than 70%, the molecules aggregated to larger structures and the shape and size of CN-DSB nanostructures changed greatly giving rise to nanobelts. This shape and size-dependent feature indicates that evolution of CN-DSB nanostructures proceeds as the volume fraction of water in the solution increases because the water-insoluble CN-DSB molecules aggregate at large water fractions. When the volume fraction of added water was increased to 90%, the size of the nanobelts along the entire length increased (Figure 3.8c). This formation of nanobelts is more or less similar to a case involving the one-dimensional nanostructures of *p*-BSP in mixtures of water and THF. Concentration dependence of the CN-DSB nanostructures formation was also studied. The nanobelts suspensions were prepared for different concentrations of CN-DSB, at 80% of water volume fractions addition. These show the formation of the nanobelts with increasing size along the entire length, ranging from 150 to 300 nm (See Figure 3.8-d, b and e).

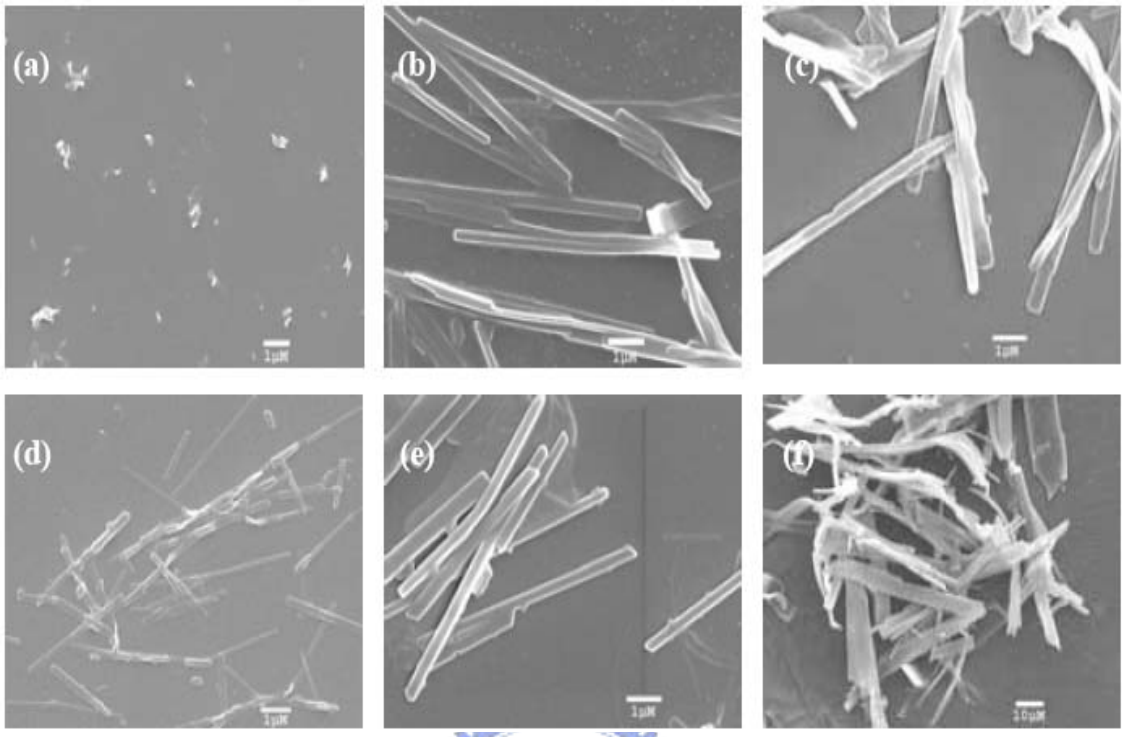

Figure 3.8 SEM images showing the evolution of CN-DSB nanostrutures obtained at different water additions and at concentrations of 3.6 × 10^{-5} mol L^{-1} *viz.* (a) 70, (b) 80, (c) 90% to THF, 1.8 × 10^{-5} mol L^{-1} for 80% (d), 7.2 × 10^{-5} for 80% (e), and for the CN-DSB bulk crystals (f), respectively.

3.2.2 Steady-state Absorption and Photoluminescence Spectra:

CN-DSB is a greenish yellow solid at room temperature. In solution it is almost non-fluorescent at low concentrations. Figure 3.9 shows the characteristic UV-visible absorption spectra (figure 3.9a) and corresponding emission spectra (figure 3.9b) of CN-DSB with various volume fractions of added water, compared to the CN-DSB single crystal, and CN-DSB in PMMA with the ratio of 1:1000. CN-DSB in THF solution exhibit strong absorption maximum at 366 nm. When water was added to THF solution of

CN-DSB, at 70% v/v addition, there was a blue shift of about 10 nm with a significant decrease in the absorbance. This shift in the absorbance is attributed to the formation of the thin, curvy nanoparticles. With the increase in the percentage of water addition, dramatic changes were observed in the absorption spectra; the absorbance increased with a large blue shift and the peak maxima were observed at 320 and 310 nm for 80 and 90% of volume fractions of water addition, respectively. This considerable and much significant blue shift and increased absorbance is attributed to the formation of well-evolved nanobelts ranging in few micrometers in length. The baseline of the absorption at longer wavelengths increases, suggesting the scattering (Mie scattering) from the larger particles formed. The blue-shifted nature of this UV-vis absorption of CN-DSB nanoparticles resembles that for DPST and DSB, for which substantially decreased emission intensity was reported on formation of nanoparticles. In contrast, we observed a greatly enhanced fluorescence emission of CN-DSB nanobelts. To measure the absorbance of a single crystal, the powder of CNDSB single crystal was dispersed on quartz and we observed that the absorbance maximum shifted slightly to ~340 nm. The increase in the baseline of the absorption at longer wavelength was attributed due to the scattering of the particles. Also we prepared thin film of CNDSB in PMMA (1:1000) to study how intramolecular rotational or torsional motion affects the excited-state dynamics. The shape of its absorption spectrum (Figure 3.9a) was similar to that of CNDSB in THF solution, which indicated that no aggregation occurred in PMMA film and the only function of PMMA is to restrict the motion of the molecule.

Emission of CN-DSB in THF is very weak. It showed the clear vibronic structures at around 425 and 445 nm (see Figure 3.9b). At 70% volume

fractions of water addition, these vibronic structures almost disappeared and a red-shifted emission band with maximum peak at around 505 nm with much enhanced emission intensity was formed. On formation of nanobelts, at 80 and 90% volume fractions of water addition, a highly intense emission band was observed with a maximum peak at about 518 nm. This observed intensity systematically increases as a function of added water and thus consequently with formation of well-evolved nanobelts. CN-DSB single crystal showed maximum peak at about 510 nm, which was similar to the spectra for CNDSB nanobelts. The packing between CNDSB single crystal and nanobelts was the same. For CN-DSB in PMMA film, the absorption maximum was similar to that of CNDSB in THF, but the photoluminescence intensity was significantly enhanced, which can be attributed to the deactivation of nonradiative decay by restricted intramolecular vibrational and torsional motions.

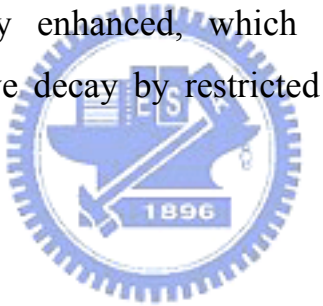

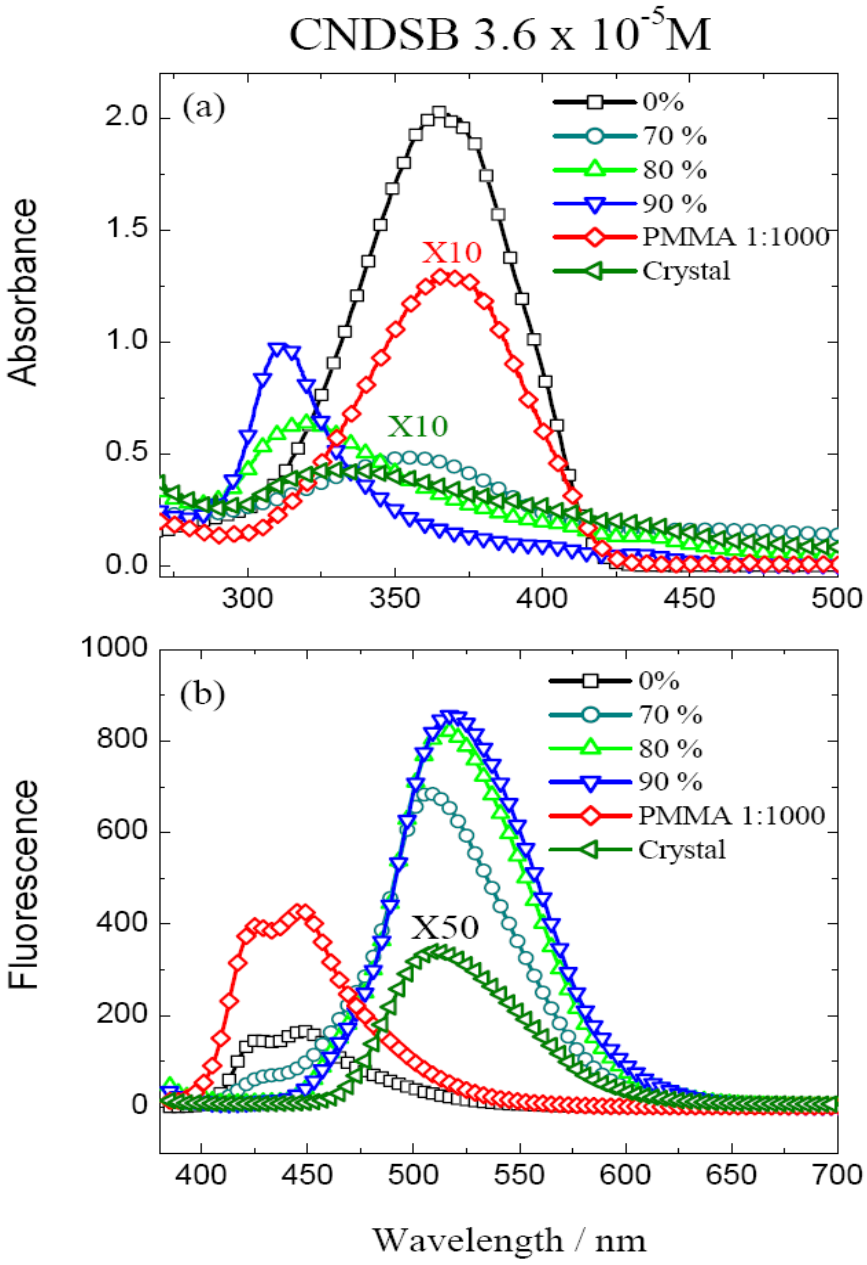

Figure 3.9 (a) UV-visible absorption spectra of CNDSB in various mixtures of water and THF, the absorbance of PMMA and single crystal film were also indicated as red diamond and olive left-triangle, respectively. (b) PL spectra of CNDSB in various mixtures of water and THF, PMMA thin film, and single crystal film as indicated.

Figure 3.10 (a) and (b) show the absorbance and photoluminescence spectra of the CN-DSB at different concentrations dispersed in water, respectively. Absorbance and emission both were decreased in water as compared to CN-DSB THF solution for the injection of 50 μL compound solution in THF. Absorbance was appeared at 360 nm for THF solution, but was decreased in the water dispersions with the appearance of a new band at around 315 nm. Also, the emission was observed at λ_{max} of about 422 nm but decreased in water dispersions at the same concentration with the formation of new band at around 522 nm. Emission showed increase in the intensity as the concentration increased with no change in the emission band position in water dispersions.

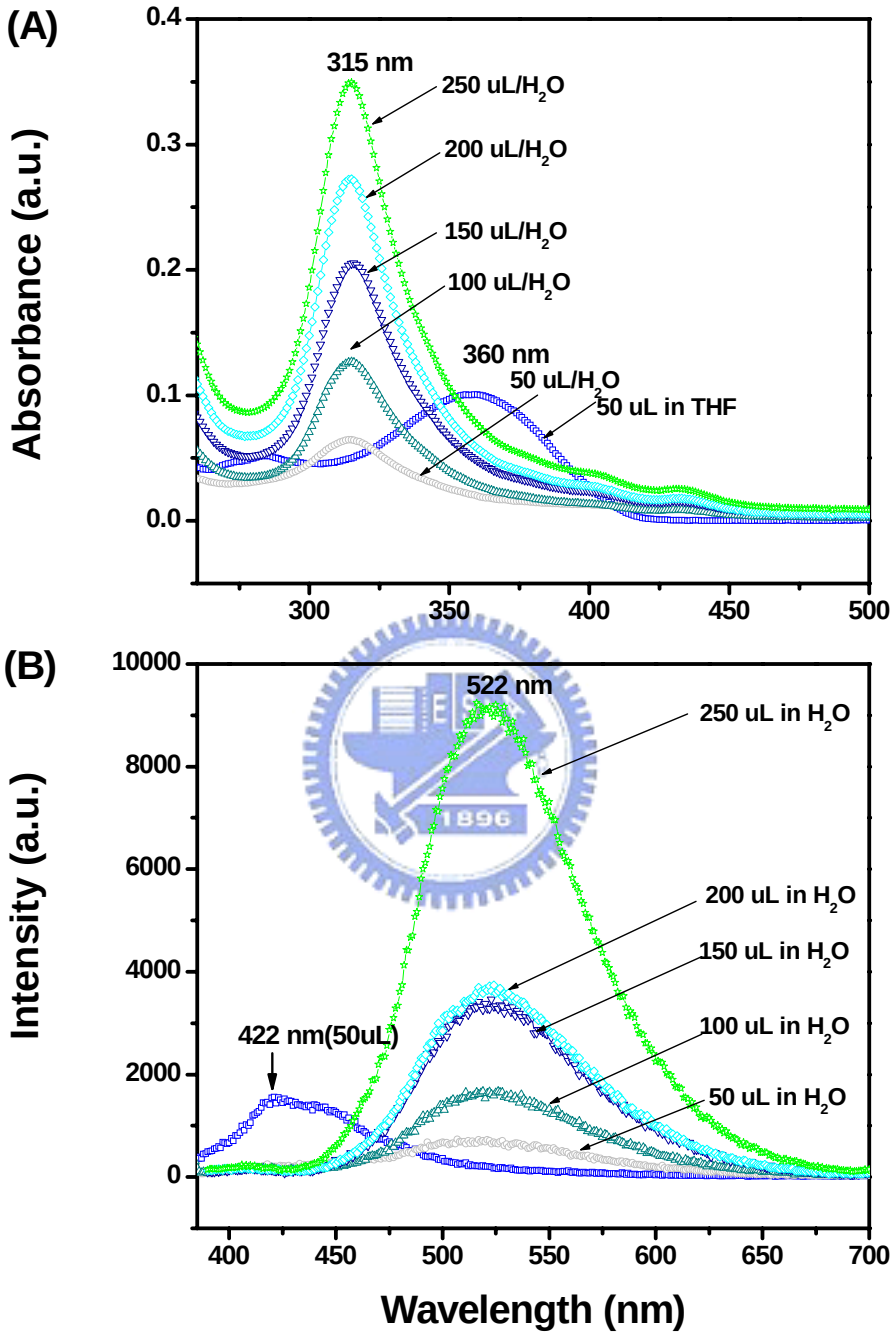

Figure 3.10 (A) Absorption and (B) Photoluminescence spectra of CN-DSB dispersed in water at different concentrations, as indicated.

3.2.3 Molecular structures of CNDSB in solid state:

Figure 3.11a show the crystal structures of the CNDSB determined at 100K. The general formula for CNDSB is $(C_6H_5)_2(C_6H_4)(C_2HR_2)$, where R = CN. There are eight symmetry related CNDSB molecules in a unit cell that can be reduced to two symmetry unique molecules, *cis*- (**1**) and *trans*-CNDSB (**2**), as shown in Figure 3.11b and 3.11c. For both molecules, the central benzene ring connects two phenyl groups via the ethylene bond in 1,4-positions. The packing patterns of CNDSB molecules form the well-known herringbone packing extending along the ***ac*** plane. The calculated herringbone angles based on such a definition of CNDSB is 87.2°, indicative of nearly perpendicular arrangement, which is quite different than that from PPB (166.9°).

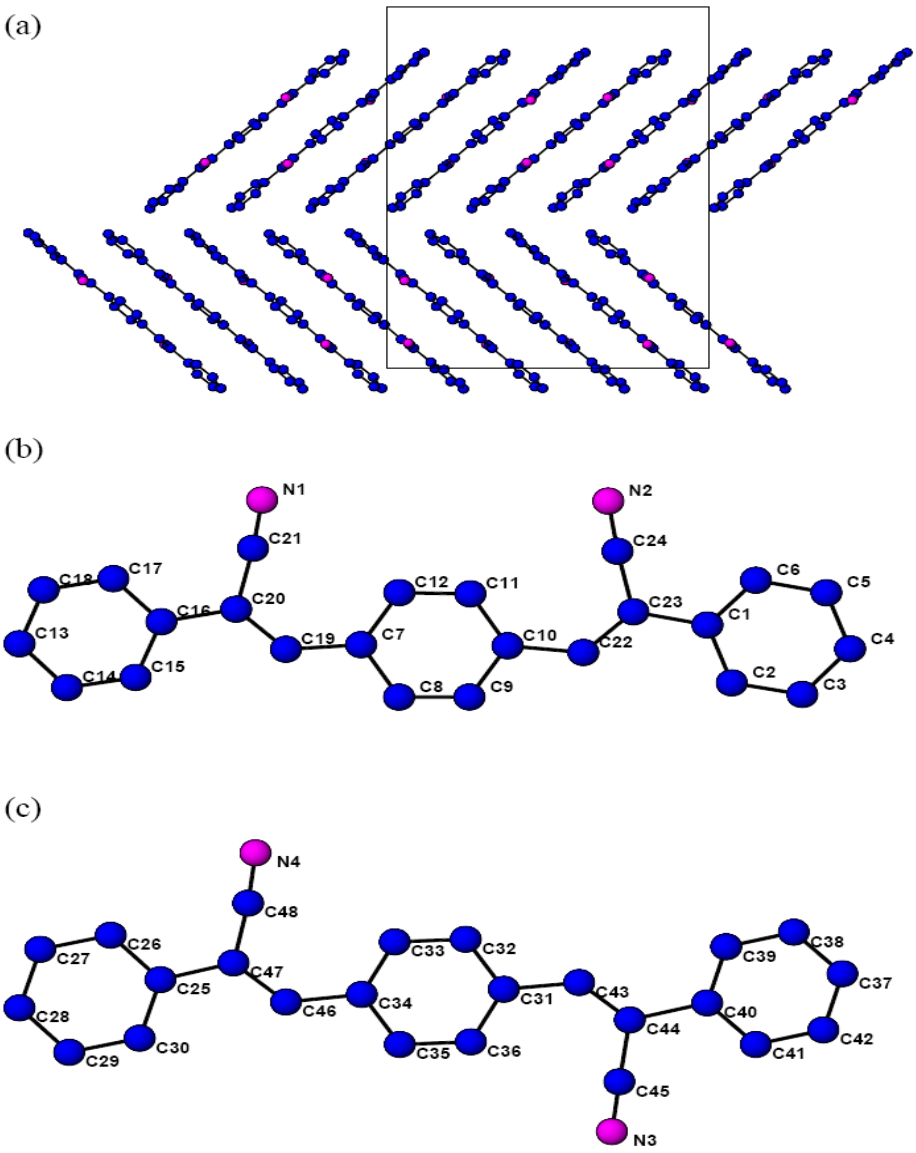

Figure 3.11 (a) Projection of the structure viewed along the [010] direction showing herringbone arrangement of CNDSB molecules. (b) The front view of *cis*-CNDSB molecules with the atomic numbering scheme. Blue circles: C. Red Circles: N. Hydrogen atoms are omitted for clarity. (c) The front view of *trans*-CNDSB molecules with the atomic numbering scheme. Blue circles: C. Red Circles: N. Hydrogen atoms are omitted for clarity. (By C.-S. Lee)

3.2.4 Picosecond Relaxation Dynamics of CNDSB nanobelts:

The ps time-resolved fluorescence spectra of CNDSB in various fractions of water and THF are shown in Figure 3.12. The excitation wavelength was 375 nm, and probed at 500 nm. Due to the limited temporal resolution of the instrument response, a sharp spike featured the transient of CNDSB in THF solution (0%). At 70% volume fraction of water, besides the spike that we observed in 0% solution, additional long component appeared in the transient. In 70% solution, the SEM image indicated that CNDSB molecules start to aggregate to form curvy nanoparticles, thus the slow component was attributed to the emission from these nanoparticles. In 80% and 90% solution, the sharp spike disappeared and the long component that appeared in 70% became the dominant part of the transient, this phenomenon indicated that most CNDSB molecules were aggregated, and the residual non-aggregated molecules were negligible. In order to avoid the interference of nonaggregate CNDSB molecules, for the relaxation dynamics of CNDSB nanobelts, the analysis was focused on the long decay components in 70, 80, and 90% solutions. At least two emissive states exist in CNDSB nanobelts: intrinsic excitonic state and defect state. From the SEM results, we know that in 70% solution CNDSB molecules starts to aggregate to form nanoparticles, and the crystalline structure is not as good as those in higher water content solutions and in a single crystal.

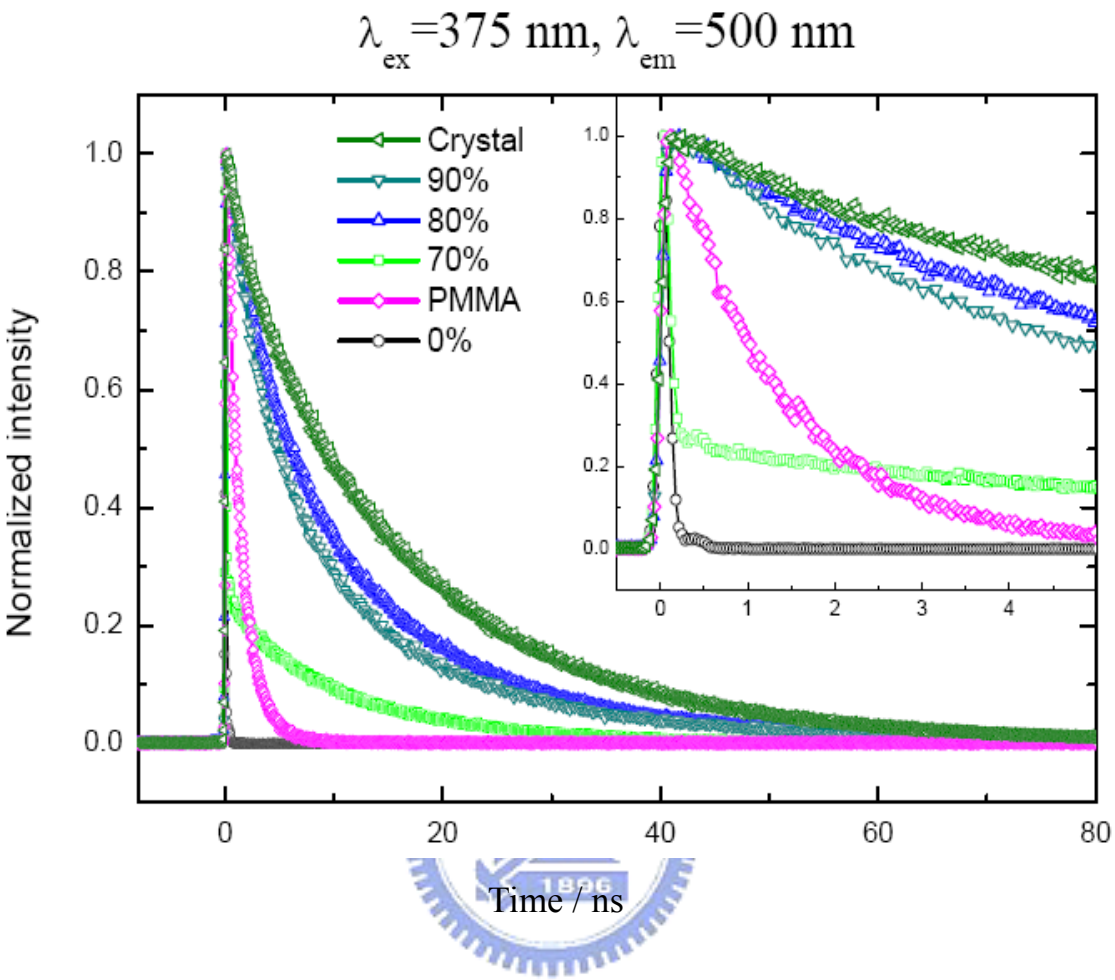

Figure 3.12 Picosecond time-resolved spectra of CNDSB in various water/THF mixtures, PMMA thin film, and single crystal obtained at λ_{ex}=375 nm, λ_{em}=500 nm. The inset was the corresponding transients in shorter time scale. (Expts. by C.-W. Chang)

To investigate how intramolecular motion would affect the excited state dynamics of CNDSB molecules, the temporally resolved transients for CNDSB/PMMA films were measured by Chih-Wei Chang. Yan Ren et[30] al also observed similar results in which the lifetime of 1,1,2,3,4,5-hexaphenylsilole (HPS) increased significantly in high viscosity solvents and low-temperature glasses. The similarity of the UV and PL spectra between CNDSB in THF solution and PMMA films indicated that no aggregation and structural changes occurred in PMMA films, and the fluorescence lifetime should be close to the radiative lifetime of CNDSB molecule. The structural confinement is only parts of the reason for the enhancement of the quantum yield in nanobelts, and the other possible reason (planar conformation, and formation of herringbone-type aggregates) has been discussed in our previous study.

In summary, for CNDSB in THF, both isomerization (0.91 ps) and vibrational relaxation (23.6 ps) processes were observed. In PMMA film, as the isomerization channel was blocked, we observed only the energy transfer process (31 ps). The XRD of single crystal indicated that the unit cell of a single crystal was constructed by both *trans* and *cis* isomers of CNDSB. For single crystal, the observed two ~ns components were attributed to the intrinsic excitonic state (17.1 ns) and defect state (2.97 ns). The optical properties of CNDSB nanobelts were also investigated. The nanobelts were prepared by reprecipation in solutions of water and THF at various volume fractions, and characterized by SEM, UV-vis absorbance and photoluminescence spectroscopy, pico-second time-resolved spectroscopy. The SEM results indicated that CNDSB molecules formed nanobelts as the volume fraction of the water exceed 70%, and the size of the nanobelts increases with the increase of water fraction. In short, we provided more

direct evidence for the deactivation through intramolecular isomerization channel, and the result indicated that structural confinement also contributed parts of the enhancement in nanobelts.

3.3 OPV Derivative With Long Alkyl Side Chain {1,4-di(octyloxy)-2,5-di[(*E*)-2-phenyl-1-propenyl]benzene} (DSB-C8):

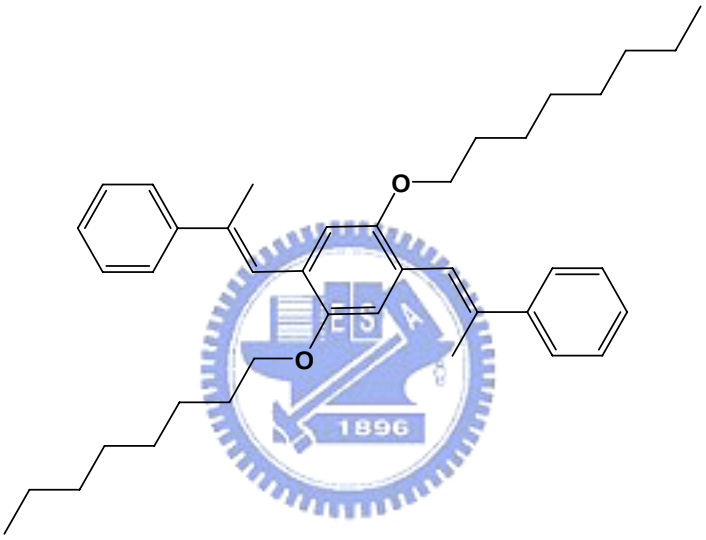

Synthesis of DSB-C8 is shown in the Scheme 2.4 and its nanostructures preparation was done by a method similar to that used for PPB and CN-DSB. The ^{1}H NMR spectrum for DSB-C8 is shown in the following Figure 3.13. DSB-C8 showed the formation of micellar-like structures and the enhanced fluorescence in these nanostructures was observed.

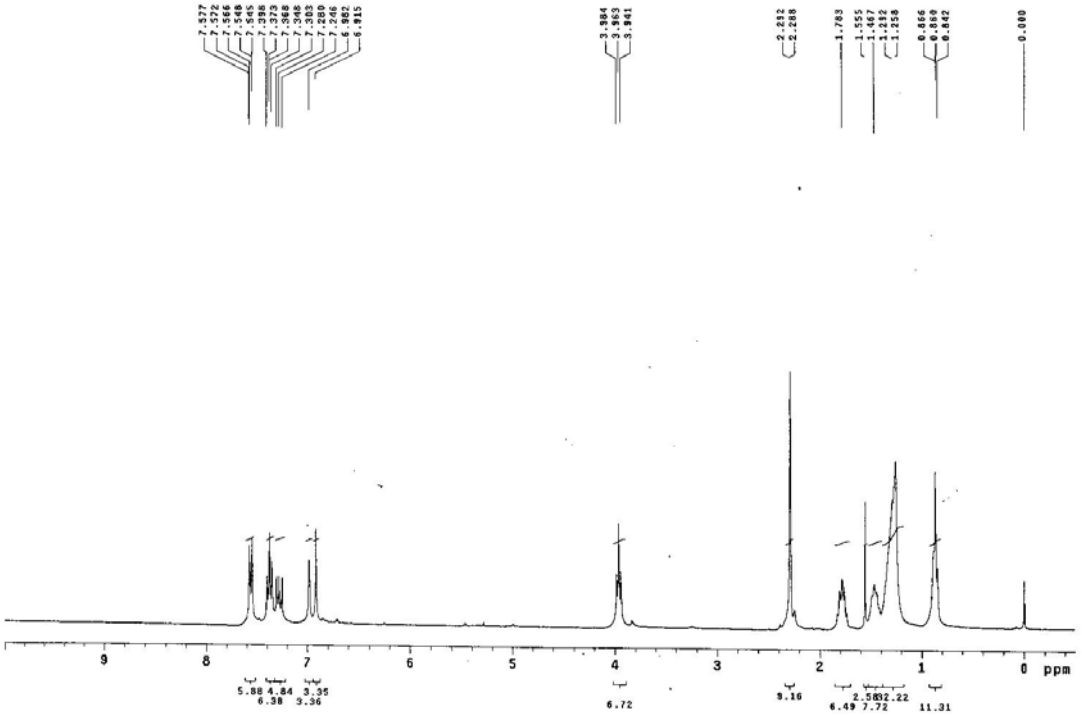

Figure 3.13 ^{1}H NMR spectrum for DSB-C8

3.3.1 Steady-state Absorbance and Photoluminescence Spectra:

DSB-C8 shows bright blue fluorescence in solution state (THF) and it is observed from figure (Figure 3.14a) that, its absorbance in THF solution shows two bands with λ_{max} at 297 nm and other at 345 nm. At 50% water addition, almost there was no change in the absorbance. However, there was an increase in the absorbance above 60% water volume fraction. The absorbance peak at 345 nm red-shifted gradually and attained the peak position at 350 nm for 80% water addition. For 60, 70 and 80% water volume fractions, at longer wavelength there observed Mie-scattering which is attributed due to the formation of the larger structures which is evident from the SEM images shown below. The photoluminescence intensity also

showed the same trend as that for absorbance. For molecular solution of DSB-C8 in THF and 50% volume fractions of water addition, the maximum peak was observed at 440 nm. As the water volume fractions increased from 60 to 80%, the PL intensity also increased with gradual red-shift of 5 nm (see Figure 3.14b) and peaks were also broadened.

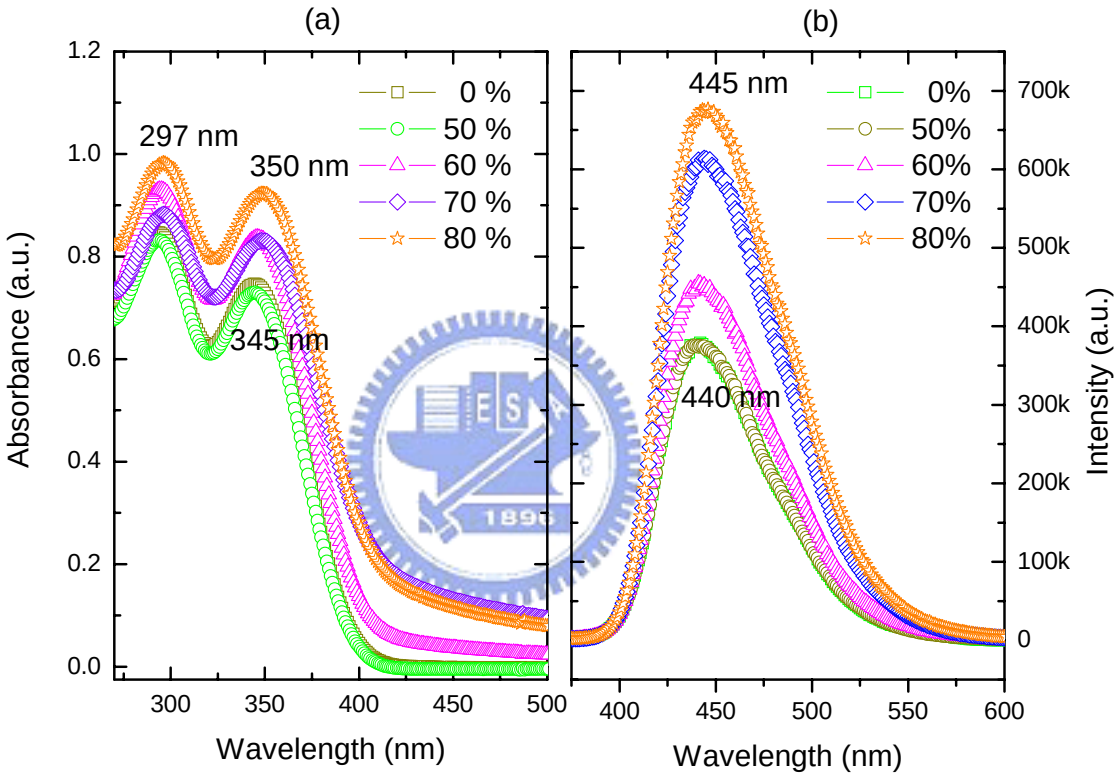

Figure 3.14 UV absorbance and photoluminescence spectra of DSB-C8 at different percent volume fractions of water and THF

3.3.2. Nanostructures Formation and Scanning Electron Microscopy (SEM):

Figure 3.15 shows the nanostructures formation at various percent of water addition. The nanostructures were started to form at 60% volume fractions of water addition. At 60%, worm-like micellar structures having

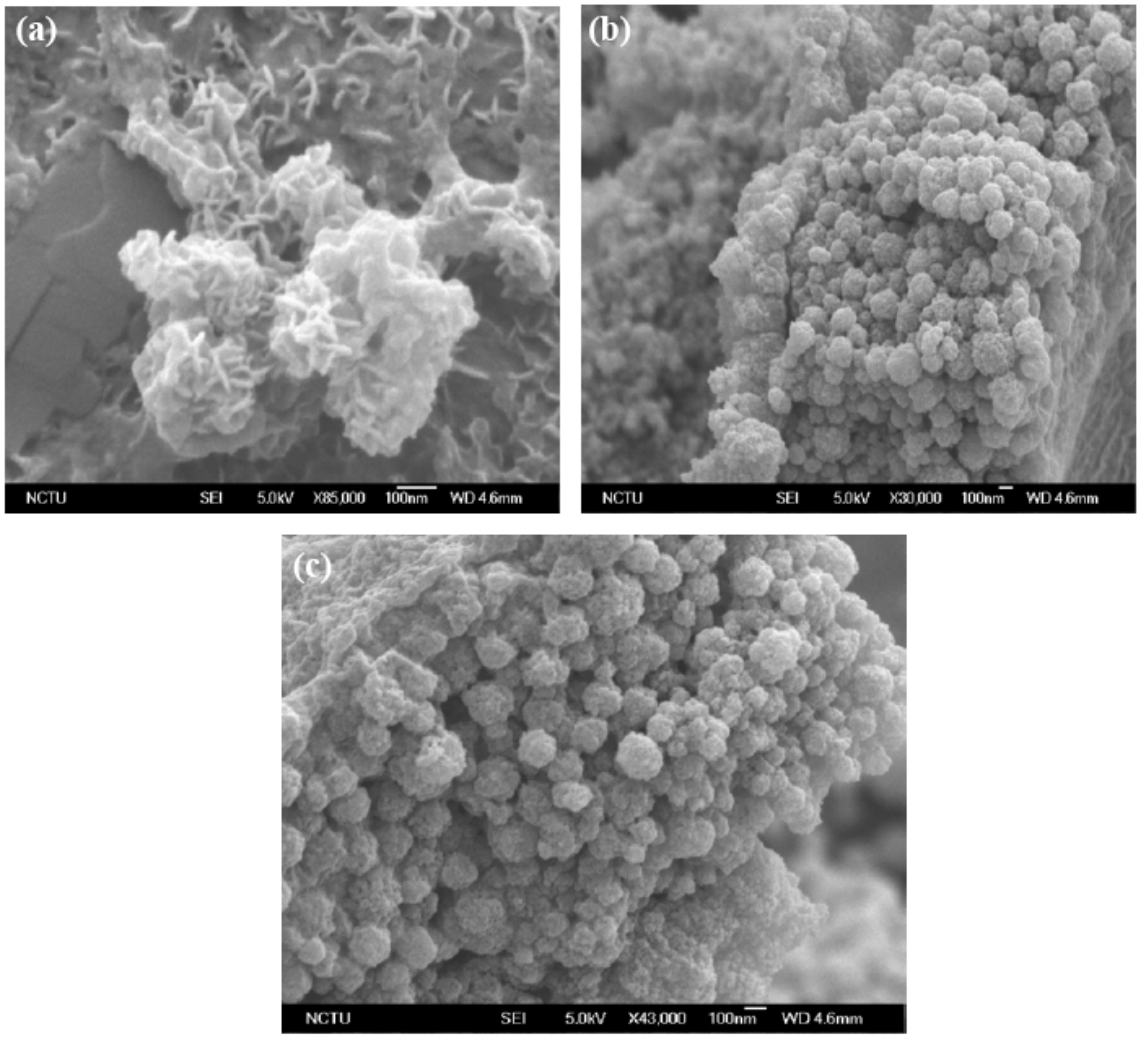

Figure 3.15 SEM images of the DSB-C8 nanostructures formed at (a) 60 (b) 70 and (c) 80% volume fractions of water addition into THF.

lengths in about 100 nm were observed and as the water volume fraction was increased from 70 to 80%, theses worm-like micelles appeared to be

accumulated or started to aggregate and form the granular nanostructures with the diameters roughly about 200-300 nm. The latter might be responsible for the Mie-scattering of the absorbance and enhancement of the PL intensity.

3.4 Hexaphenylsilole (HPS):

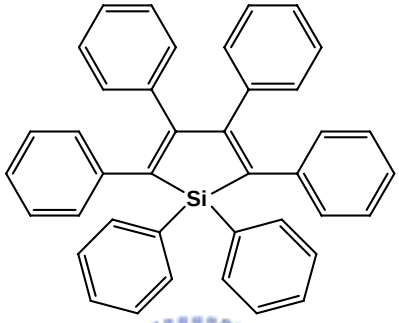

Hexa-Phenyl Silole (HPS)

3.4.1 Scanning Electron Microscopy (SEM) images:

Hexaphenylsilole (HPS) is greenish color crystalline compound which emits very bright blue color under UV light and its THF solution is faint green when seen by naked eyes and shows almost no fluorescence under UV light. HPS nanoparticles were prepared according to simple reprecipitation with THF as solvent and volume fractions of water, viz. 0, 50, 60, 70, 80 and 90%. The nanoparticle suspension in these solutions appeared slightly turbid when the volume fraction of added water exceeded 60%. Although molecular aggregation might have initiated at smaller volume fractions of added water, formation of nanostructures with clear images was observed by SEM only after 60% water additions. In four parts, Figure 3.16 presents SEM photographs of HPS nanostructures prepared at (a) 60, (b) 70, (c) 80 and (d) 90% of added water.

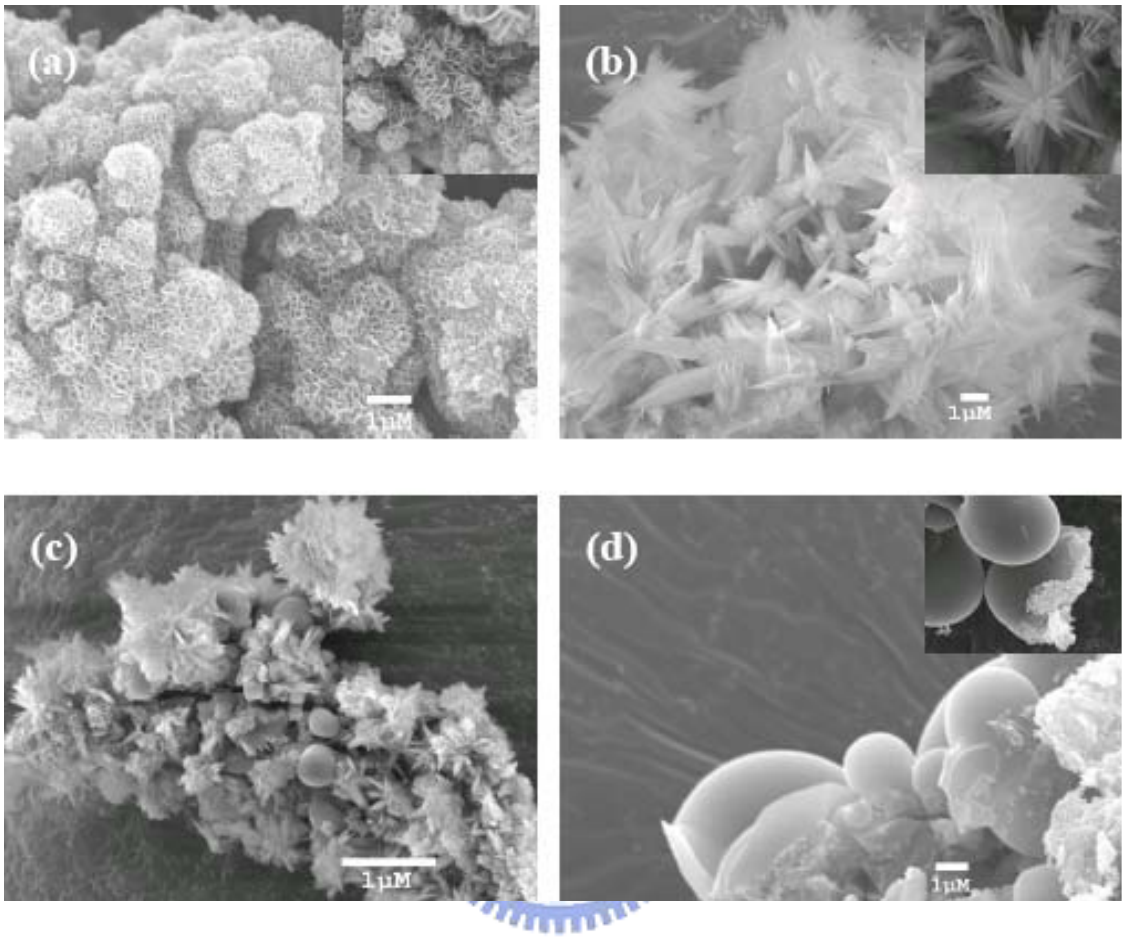

Figure 3.16 SEM images of various nanostructures of HPS obtained from suspensions of nanoparticles with (a) 60, (b) 70, (c) 80 and (d) 90 % volume fractions of water added to THF, respectively.

According to the SEM, it seems that free molecules in solution began to aggregate and to evolve during growth with increasing fraction of water addition. Thin sheets of nanostructures of length 300-400 nm and thickness only a few nanometers were formed at 60% volume fraction of added water, initially. During such process, the superior solvent (THF) was replaced by

the inferior solvent (water) and dispersed in bulk water. As the proportion of added water was increased beyond 60%, the molecules aggregated to larger particles. At 70% volume fraction of water addition, nanoflowers were obtained, as shown in the inset of Figure 3.16b. When the volume fraction of added water was increased to 80%, nanoglobular structures and a few nanoflowers were formed (Fig. 3.16c). At 90% of water addition, these nanoglobules grew to a diameter of a few micrometers. The inset of Figure 3.16d shows broken microglobules incorporated with nanosheets and/or nanoflowers with a surface layer, indicating that these microglobules evolved from the original nanoglobules on encapsulating those nanostructures inside globular structures at 90% water addition during aging of the solution.

In our experiments, water with varied volume fractions was added quickly into THF solutions of HPS, so that THF becomes replaced by water and dispersed in the bulk water. This process takes no more than a few seconds and is spontaneous. All solutions were stirred for an hour after mixing so that the well evolved nanostructures were obtained. During solvent dispersion, the HPS molecules tend to aggregate, which produces sheets with thickness a few tens of nanometers. We suppose that particles at lower water fractions are smaller. At 70% volume fraction of added water, the degree of aggregation increases abruptly and produces novel nanoflowers (Figure 3.16b). We speculate that, upon further increase of the water fraction to 80% solution, HPS nanoglobules began to form at the expense of nanoflowers (Figure 3.16c). Formation of HPS microglobules observed at 90% solution (Figure 3.16d).

3.4.2 Absorption and Emission Spectra of HPS Nanostructures

HPS is a faint green solid under normal light, but emits bright fluorescence of Prussian blue color under UV irradiation. UV/visible absorption spectra and corresponding emission spectra of HPS with various volume fractions of added water are shown in Fig. 3.17-a and b, respectively.

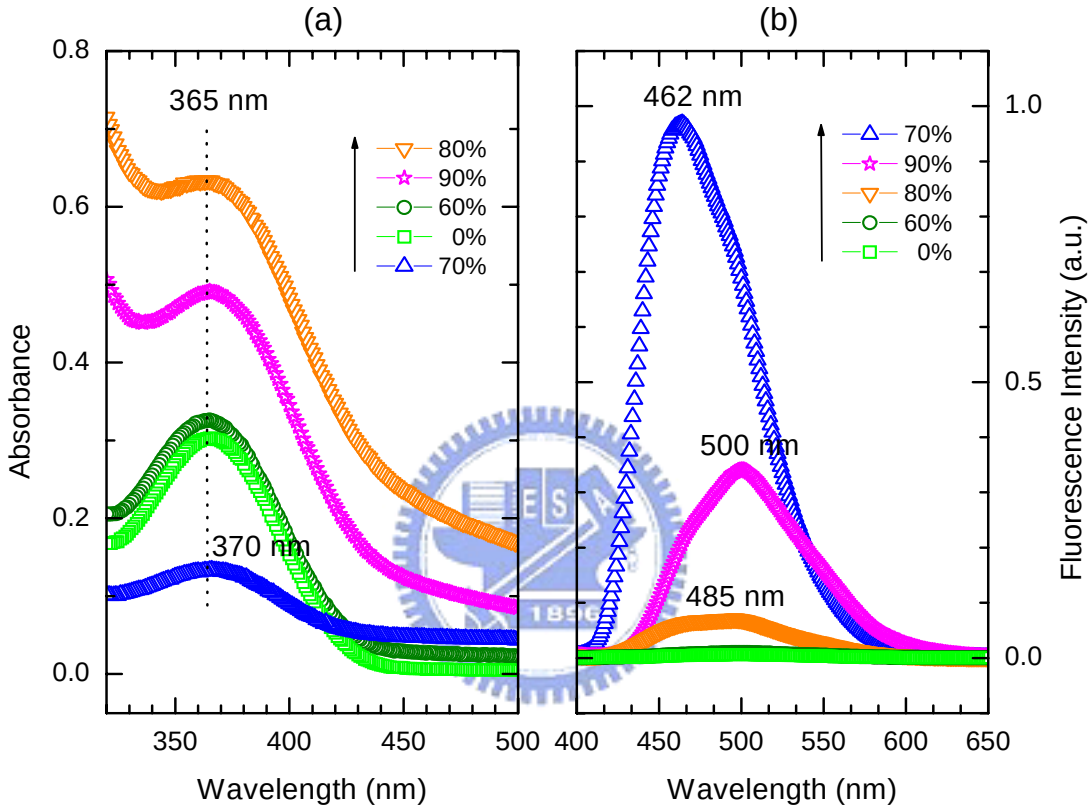

Figure 3.17 (a) UV/visible absorption spectra of HPS showing the variation of absorbance with proportions of water and THF as indicated. (b) PL spectra of HPS showing the variation of fluorescent intensity for mixtures of water and THF at various proportions as indicated.

In general, the UV/visible spectra show absorption with a maximum near 365 nm for all solutions. The appearance of Mie scattering in the long wavelength region of the spectra for 70-90% solutions indicates the

formation of significant HPS aggregates in those solutions and that is consistent with SEM photographs shown in Figure 3.16. At 70% volume fraction of added water, the absorbance decreased substantially with the maximum absorbance slightly shifted to 370 nm. At solutions with water volume fractions 80 and 90%, increased absorbance accompanied substantial Mie scattering interference shown as a tail extending into the visible region.

Remarkable effects were observed in the corresponding emission spectra (Figure 3.17b). The HPS solution in pure THF showed almost no emission and the solutions at 50 and 60% water fractions showed likewise only weak emission comparable to that of the 0% solution. Although the SEM image in figure 3.16a shows formation of nanosheets at 60% added water, we observed no enhancement of emission, but, when the water fraction was increased to 70%, the emission was enhanced about hundred times that of the HPS solution in pure THF, with the maximum peak (λ_{max}) occurring at 462 nm. This enhancement is due to the formation of nanoflowers as can be seen in Figure 3.16b. The emission of a HPS film is reported to be slightly blue-shifted and narrower than that of its solution.[31] Furthermore, HPS in a mixture of acetone and water also shows a blue-shifted feature with emission enhanced at water fraction 60%.[35] In our studies, the enhanced blue-shifted spectral feature occurs at 70% solution on formation of the novel nanoflowers.

We observed a decreased PL intensity with a maximum at 485 nm, for 80% added water. This decrease might be due to the formation of some nanoglobules along with nanoflowers (Figure 3.16c). When the volume fraction of added water was increased to 90%, the PL intensity again increased with the wavelength red-shifted to ca. 500 nm. Figure 3.18 from left to right shows PL images of solutions excited at 365 nm, for 0, 70 and

90% volume fractions of added water, respectively. Color tuning with emission enhancement of HPS was thus observed upon formation of nanoflowers and microglobules.

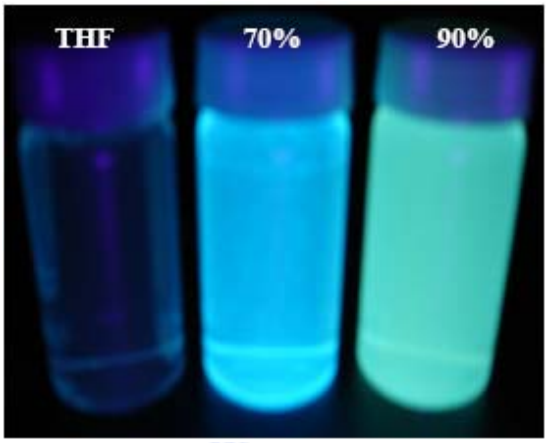

Figure 3.18 Fluorescence emission of HPS in pure THF (left), suspensions of nanoparticles in water/THF mixtures with 70 % (middle) and 90 % (right) water. (Excitation at 365 nm)

3.4.3 Picosecond TCSPC measurements:

Time-dependent measurements of HPS in solutions of water and THF at various proportions were performed using time-correlated single-photon counting with excitation at λ_{ex} = 375 nm and emission observed at λ_{em} = 520 nm; typical results are shown in Figure 3.19, and the fitted parameters are summarized in Table 3.1.

Table 3.1: Fitted time coefficients of HPS in water/THF solutions at various concentrations.[a,b]

Time coefficients/ns	0 %	60 %	70 %	80 %	90 %
τ_1	0.02 (1.0)	0.04 (1.0)	0.2 (0.27)	0.15 (0.74)	0.37 (0.36)
τ_2			6.2 (0.73)	6.3 (0.02)	4.3 (0.18)
τ_3				0.5 (0.24)	1.8 (0.46)
$\tau^{[c]}$	0.02	0.04	4.6	0.4	1.7
$\Phi_F^{[d]}$	0.0015	0.003	0.35	0.03	0.13

[a] The excitation wavelength was fixed at 375 nm and emission was observed at 520 nm.

[b] The numbers in parentheses are the relative amplitudes.

[c] Mean lifetime $\tau = \Sigma_i A_i \tau_i$, where A_i is relative amplitude of component i.

[d] Fluorescence quantum yield was determined by the ratio $\tilde{\tau}\ \tau_r$, where τ_r(~13 ns) is the radiative time coefficient determined.

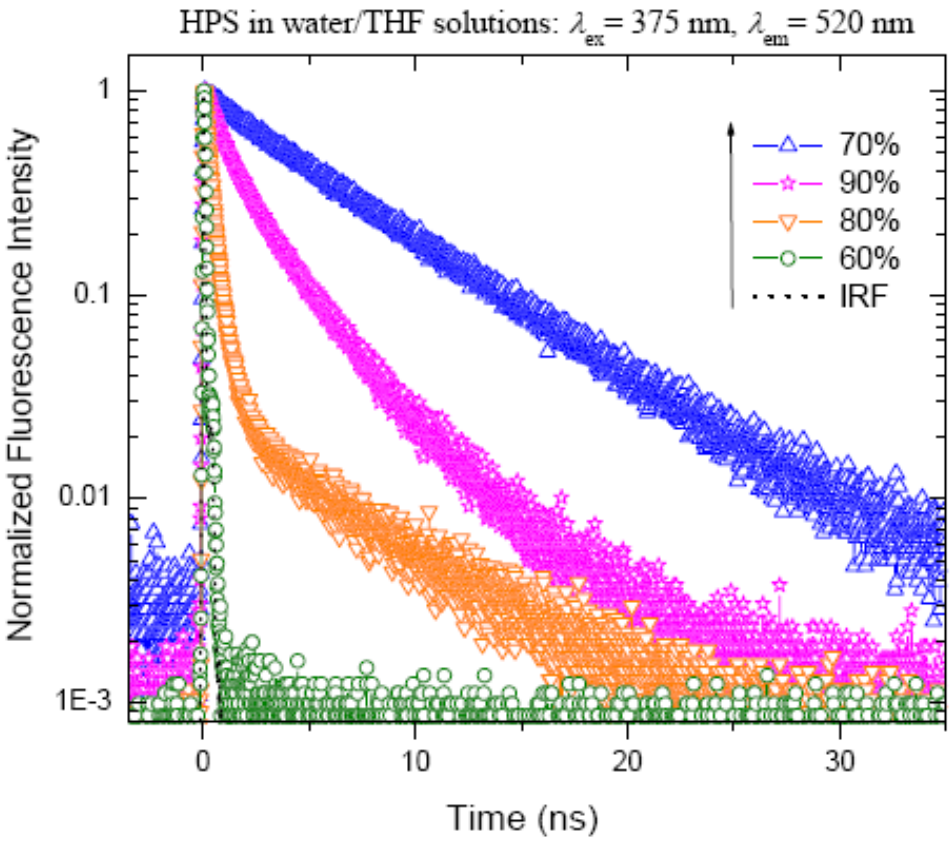

Figure 3.19 Picosecond fluorescent transients of HPS in water and THF mixtures with various proportions as indicated. The data were obtained with excitation at λ_{ex} = 375 nm and emissions probed at λ_{em} = 520 nm. (Expts. by C.-W. Chang)

Fluorescence was scarcely detectable for HPS dissolved in THF/water mixtures with water fractions less than 60%. In dilute solution of THF, HPS molecules can move freely without restriction imposed on certain intramolecular motions. Water was initially added into the THF solution and HPS molecules began to pack and to form aggregates because water is a poor solvent for HPS. Increasing the water fraction to 70% caused a major

enhancement of emission intensity (Figure 3.17b) and also increased lifetime of the excited state (Figure 3.19). The efficient nonradiative relaxation of HPS that occurs in THF became inhibited due to the restriction of the intramolecular vibrational and torsional motions in the nanostructures that produces the enhanced fluorescence observed for nanoflowers at 70% solution. The transient in 80% solution (Figure 3.190) displays a much more rapid kinetic feature with a tiny slow decay component and its decay coefficient was 6.3 ns. Increasing the water volume fraction to 90%, the kinetics of the transient showed an intermediate decay feature between those of 70% and 80% solutions (Figure 3.19). Because the nanoglobules produced in the 80% solution evolved to form microglobules in the 90% solution (Figure 3.16), the effective length of conjugation of HPS aggregates might be greater for the former than the latter, which is consistent with the observed emission intensity being more intense for the former than for the latter and the emission spectrum being red-shifted to 500 nm for the 90% solution (Figure 3.17b).

In conclusion, we have prepared various types of nanostructures of hexaphenylsilole (HPS) in solutions of water and THF using reprecipitation and characterized their enhanced and color-tunable photophysical properties with steady-state and time-resolved spectral methods. Strong emission from well evolved HPS nanoaggregates was observed, but emission from HPS in dilute THF solution was barely detectable. We found that novel nanoflowers were produced at 70% water addition with blue-shifted emission, λ_{em} = 462 nm, with an increase in intensity by hundred times. Picosecond time-resolved fluorescence investigations yielded excited-state lifetimes of about 4.6, 0.4 and 1.7 ns for nanoflowers, nanoglobules and microglobules, respectively. The observed enhancement of the emissions in various

water/THF solutions is not only due to the AIE effect but also strongly depends on the morphologies of the nano/microstructures.

3.5 Nanostructures formation of Amino-stilbene Derivatives:

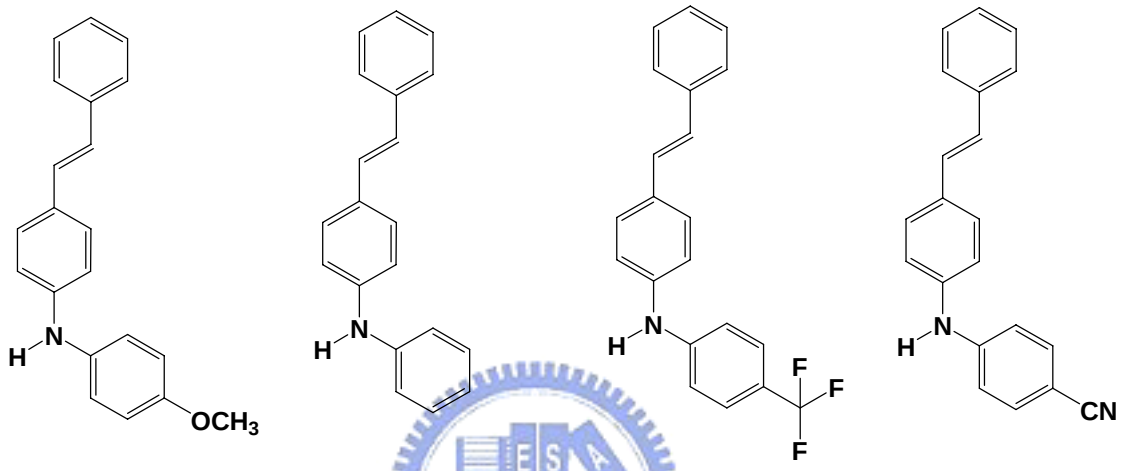

Initially, stock solutions of all these amino-stilbene compounds in 5 mL THF were prepared with constant concentration of 1.66 x 10^{-3} M. In all 10, 9, 12.5 and 9.8 mg of amino-stilbenes (with –OMe, -H, -CF_3 and –CN groups, respectively) were dissolved in 5 mL THF each and then certain amounts were injected through microsyringe into THF or water as required. Thus nanodispersions of these compounds in water were formed.

3.5.1 Steady-state Absorbance and Photoluminescence Spectroscopy:

Figure 3.20, in two parts, show (a) absorbance and (b) photoluminescence spectra of the molecular solutions in THF and nanoparticles of various amino-stilbene derivatives, as indicated. It has been observed that the fluorescence gets quenched in nanoparticles, and the absorbance spectra are blue-shifted in nanoparticles. The photoluminescence intensities are

decreased with large red-shifts. These compounds can thus be applicable in fluorescence on-off switching.

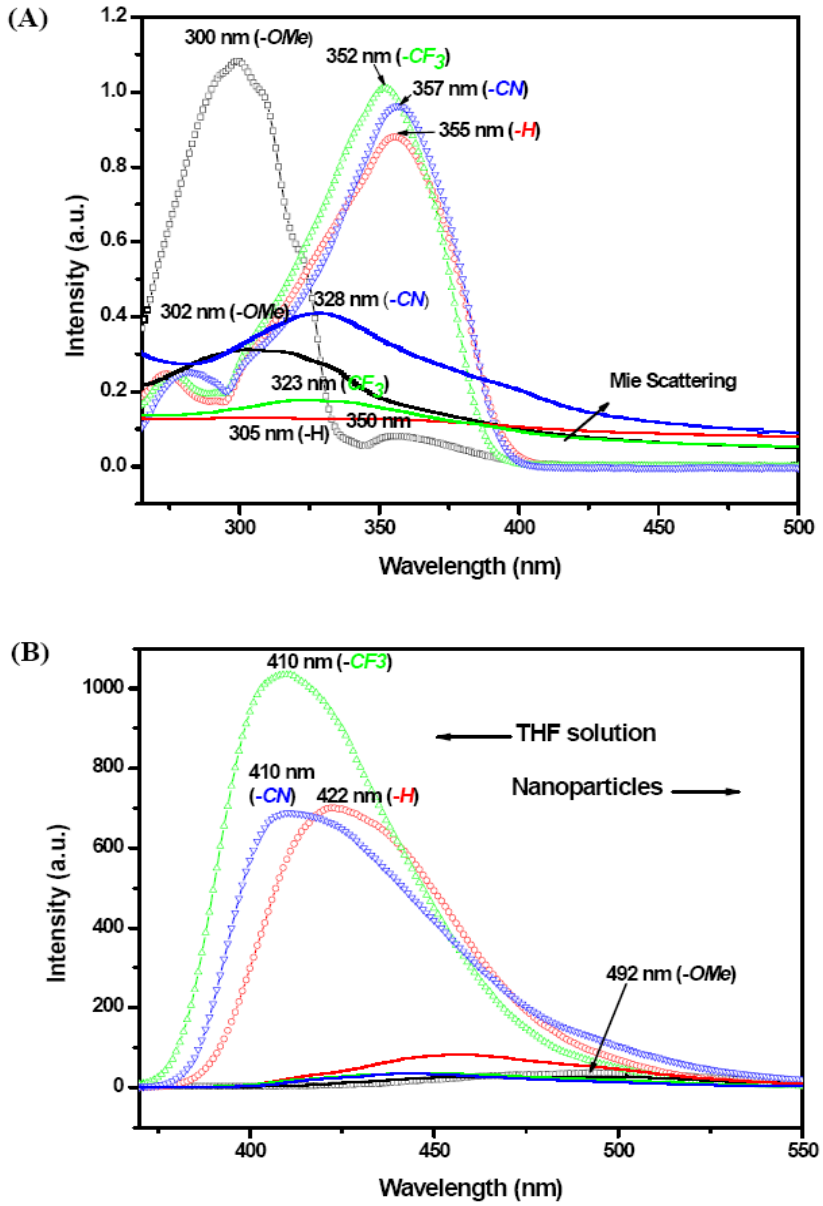

Figure 3.20 (A) UV-Vis absorbance and (B) Photoluminescence Spectra of the Amino-stilbene derivatives in THF solution and in nanoparticles, as indicated.

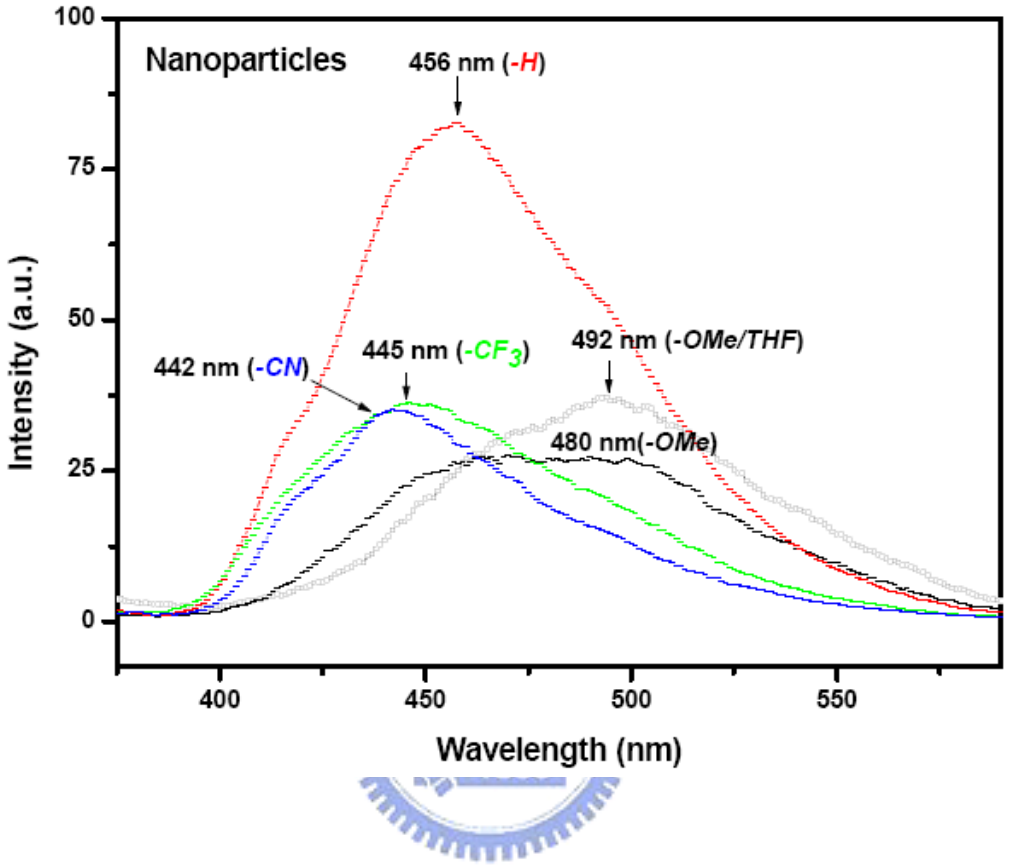

Figure 3.21 Photoluminescence Spectra (enlarged) of the Amino-stilbene Derivatives nanoparticles suspensions.

3.5.2 Scanning Electron Microscopy:

In four parts, Figure 3.22 show the SEM images of the nanoparticles of various amino-stilbene derivatives obtained from reprecipitation method. Compound **9** showed hollow vesicular morphology (200-250 nm), compound **10** showed spherical (150-200 nm), compound **11** (150-200 nm) and **12** (250-300 nm) showed cubic morphologies.

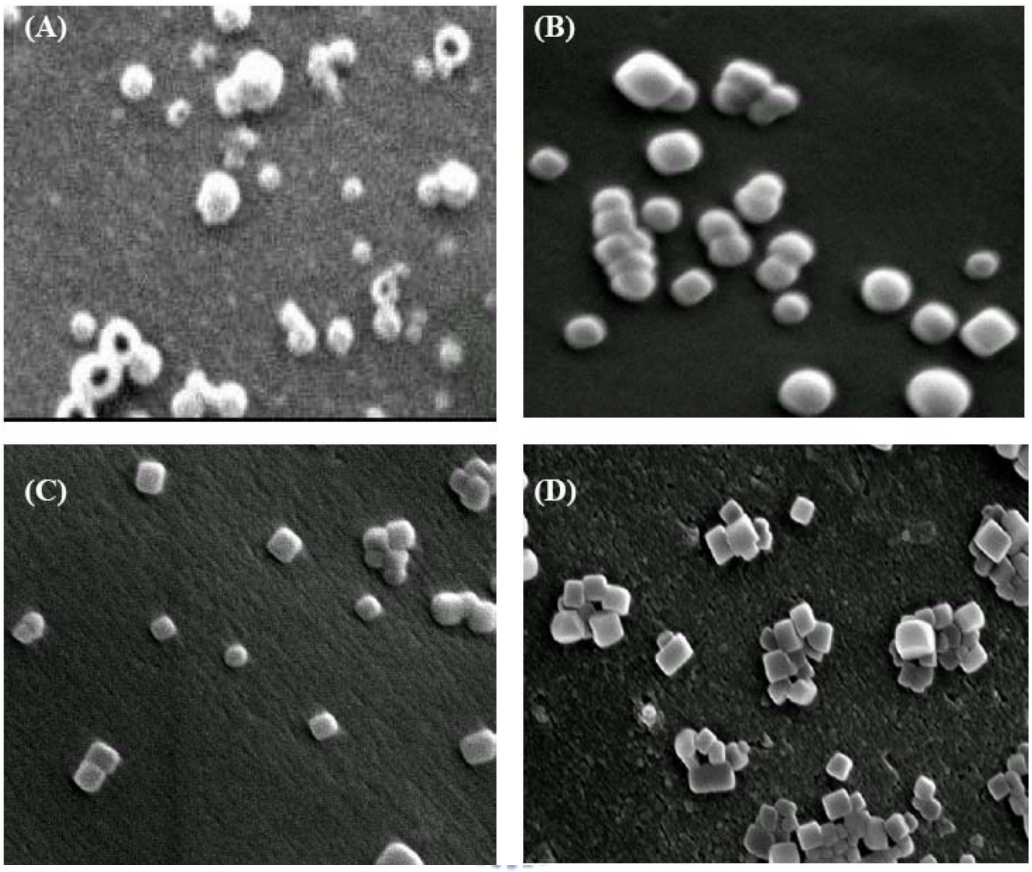

Figure 3.22 Scanning electron microscopy images of the nanoparticles of Amino-stilbene derivatives (a) –OMe 200-250 nm, (b) –H 150-200 nm, (c) -CF_3, 150-200 nm and (d) –CN, 250-300 nm

3.6 Rod-Coil Molecules (15a-c):

(A)

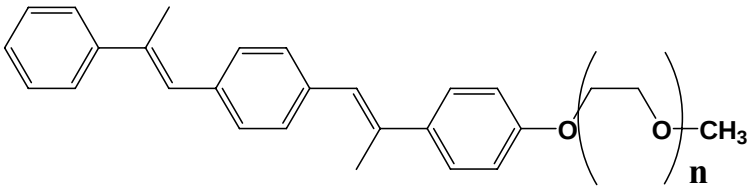

n = 8, 17, 45

Synthesis and Characterization:

The representative OPV derivatives with different ethylene glycol repeating units (n = 8, 17, 45) were synthesized as outlined in the Scheme 2.6 and their ^{1}H NMR spectra are shown in the following Figures 3.23, 3.24, and 3.25, respectively.

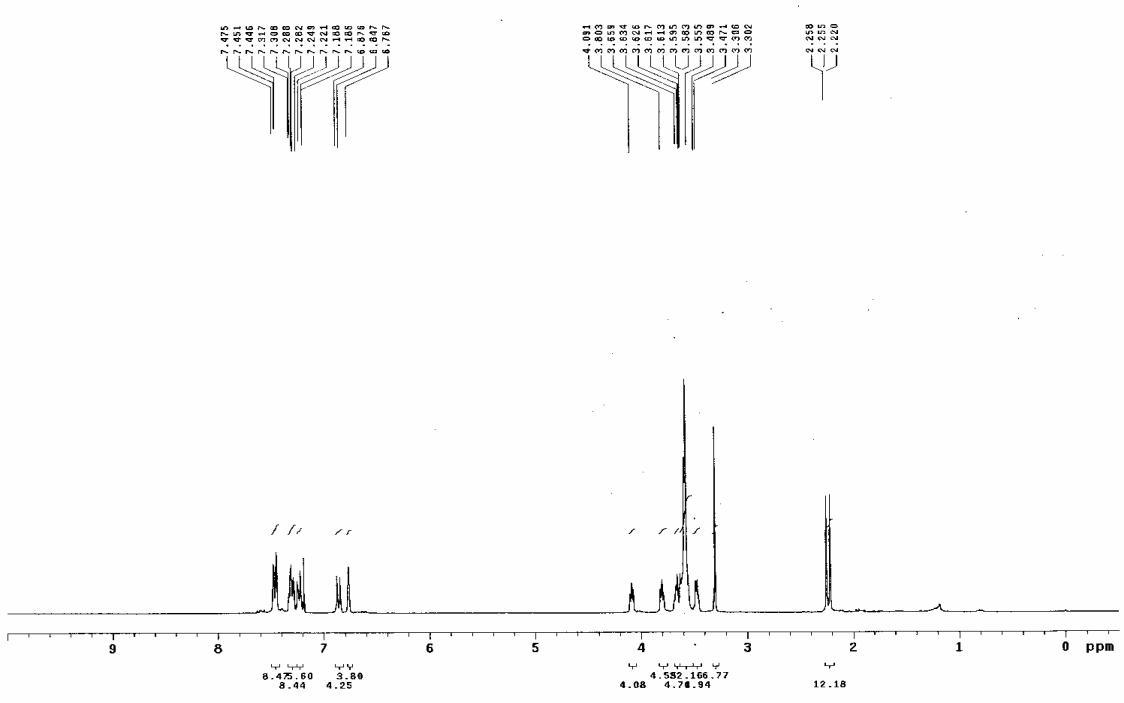

Figure 3.23 ^{1}H NMR Spectrum of Compound 19a

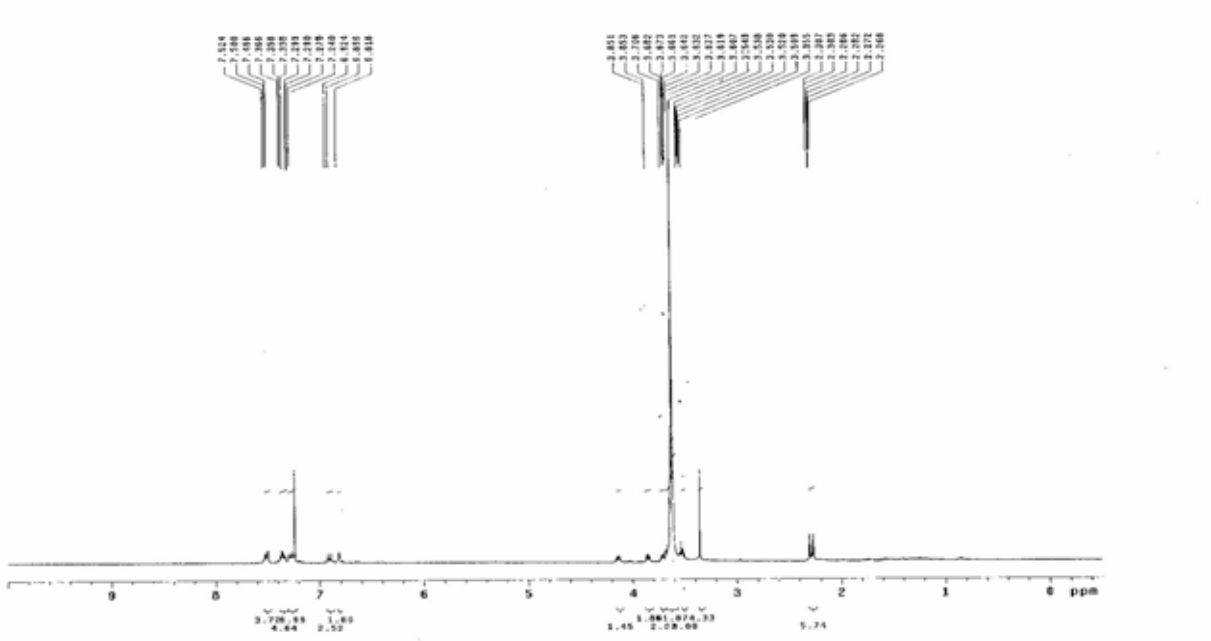

Figure 3.24 ^{1}H NMR Spectrum of Compound 19b

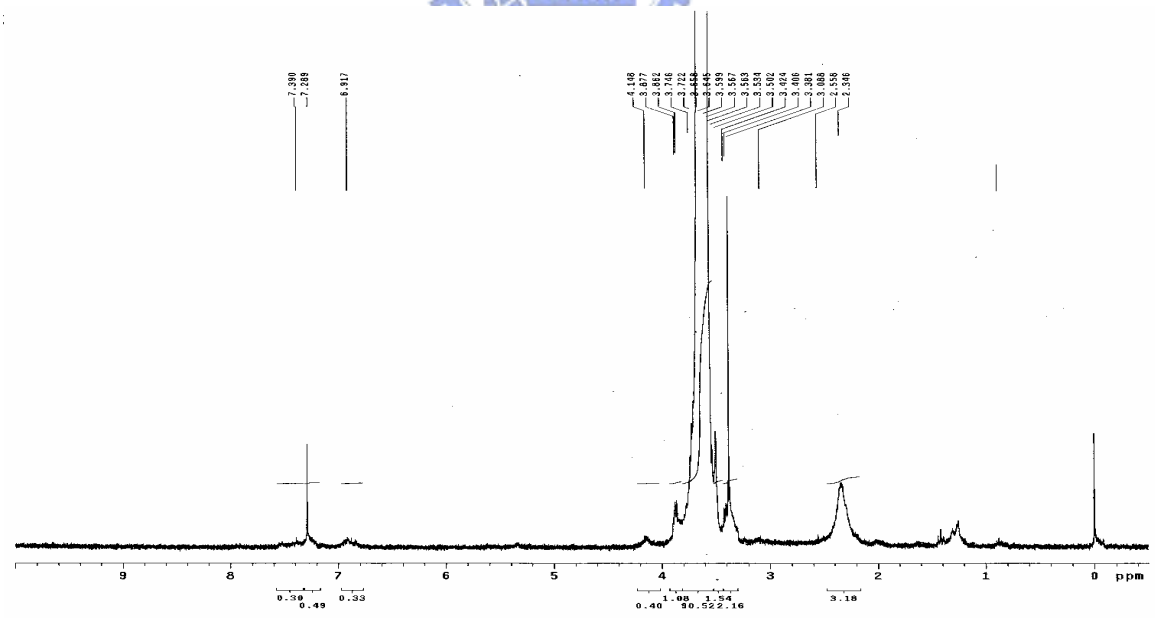

Figure 3.25 ^{1}H NMR Spectrum of Compound 19c

Nanostructures Formation of OPV Derivatives:

Typically, stock solution of the compounds 19a, 19b and 19c were made and certain amount of stock solution was injected in the water and made its dispersions in water. The dispersions were stirred for one hour prior to measurements. The concentrations of all solutions were 1.35 x 10^{-5} M after injecting into THF or water.

3.6.1 Steady-state absorbance and photoluminescence spectra:

Steady-state absorbance and photoliminscence spectra of **19a-c** in molecular solutions of THF and their dispersions in water were recorded as shown in figure 3.26 (a) and (b), respectively. The absorbance of **19a** and **19b** in THF solution was observed to be almost the same, except the shift in the band position. **19a** in THF showed absorbance at λ_{max} = 317 nm while **19b** showed at 315 nm. However, **19c** in THF showed comparatively low absorbance with a band splitting at 280 and 310 nm. When nanodispersions of these compounds in water were formed, their absorbances increased dramataically. The **19a-b** nanodispersions in water showed the absorbance at around 305 nm. Nanodispersions of **19c** also showed increase in the absorbance with λ_{max} at 295 nm and a less prominent shoulder at about 324 nm.

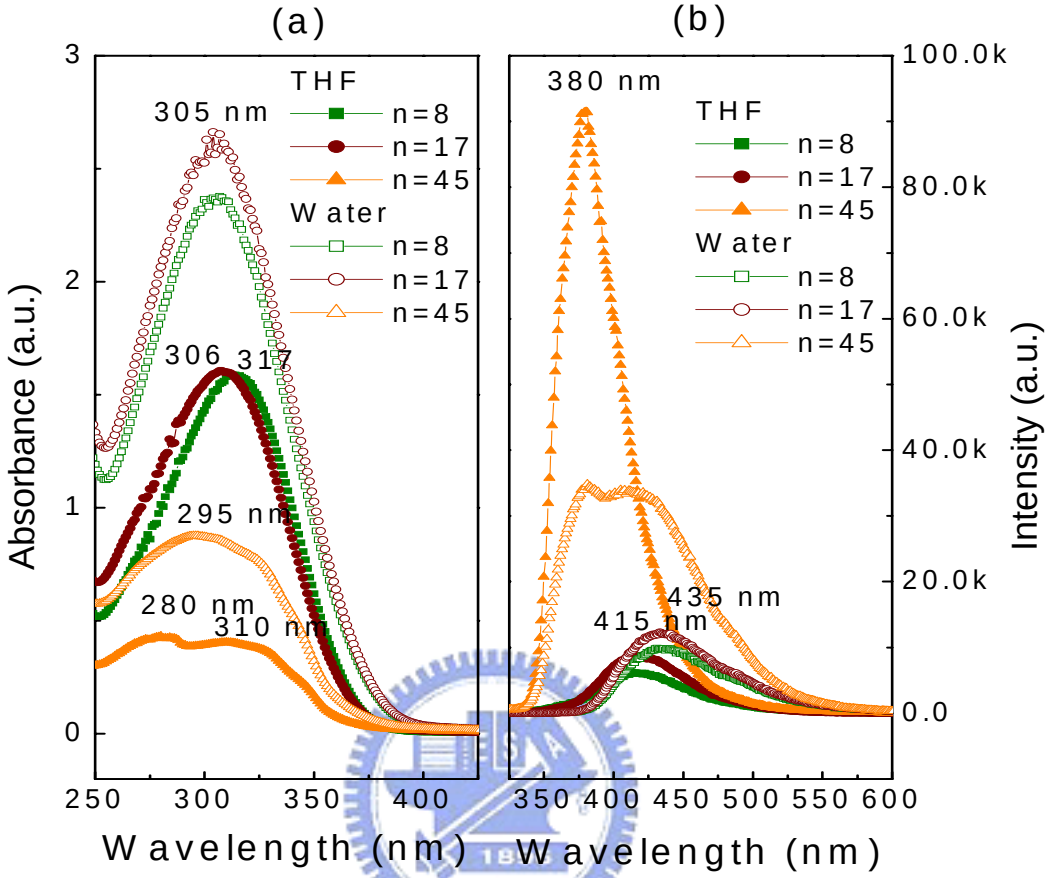

Figure 3.26 Steady-state (a) UV-Visible absorbance and (b) Photoluminescence (PL) spectra of rod-coil molecules (19a-c) in THF as well as in nanodispersions in water.

Photoluminescence of **19a** and **19b** in THF showed increasing trend in their intensities. This trend remained the same in nanodispersions with comparative increase in the PL intensities than their respective THF solutions. Both these rod-coil molecules showed maximum wavelength at about 415 and 435 nm in their THF solution and nanodispersions,

respectively. However, rod-coil molecule with n=45 (**19c**) showed different results. **19c** in THF solution showed highest photoluminescence intensity of all with λ_{max} at 380 nm and its photoluminescence intensity decreased in nanodispersions drastically with a red shift in the PL peak and band splittings at 381 and 415 nm.

3.6.2 Nanostructures Formation and Scanning Electron Microscopy (SEM):

Nanoparticles of OPV rod-coil molecules were formed after making their dispersion in water. The size of the nanoparticles increased with length of the coil. The scanning electron microscopy images are shown in Figure 3.27. The average diameter of the particles of **19a** was about 150 nm and that for **19b** was about 300 nm. These particles were uniformly distributed. However the particles of **19c** rod-coil molecule were in the micrometer range (1-3 μm) and were unevenly distributed.

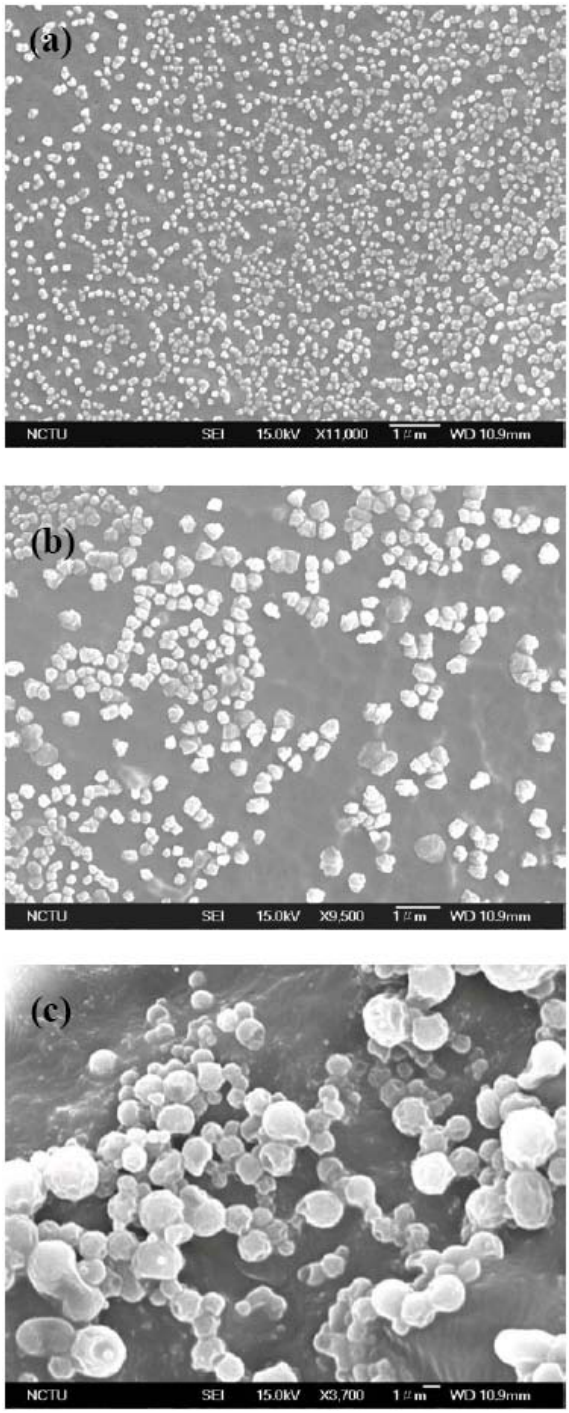

Figure 3.27 SEM images obtained from the nanodispersions in water of the OPV rod-coil molecules (a) 19a (b) 19b and (c) 19c.

(B) OPV rod-coil molecules with DSB as the rod

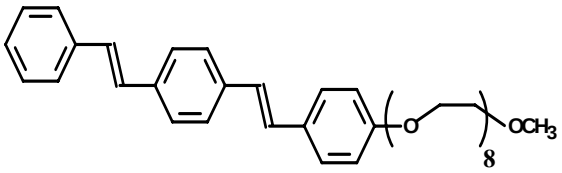

Synthesis of OPV derivative (**21**) with 8 ethylene glycol repeating units shown above is outlined in a Scheme 2.7. Its ^{1}H NMR spectrum is shown in Figure 3.28.

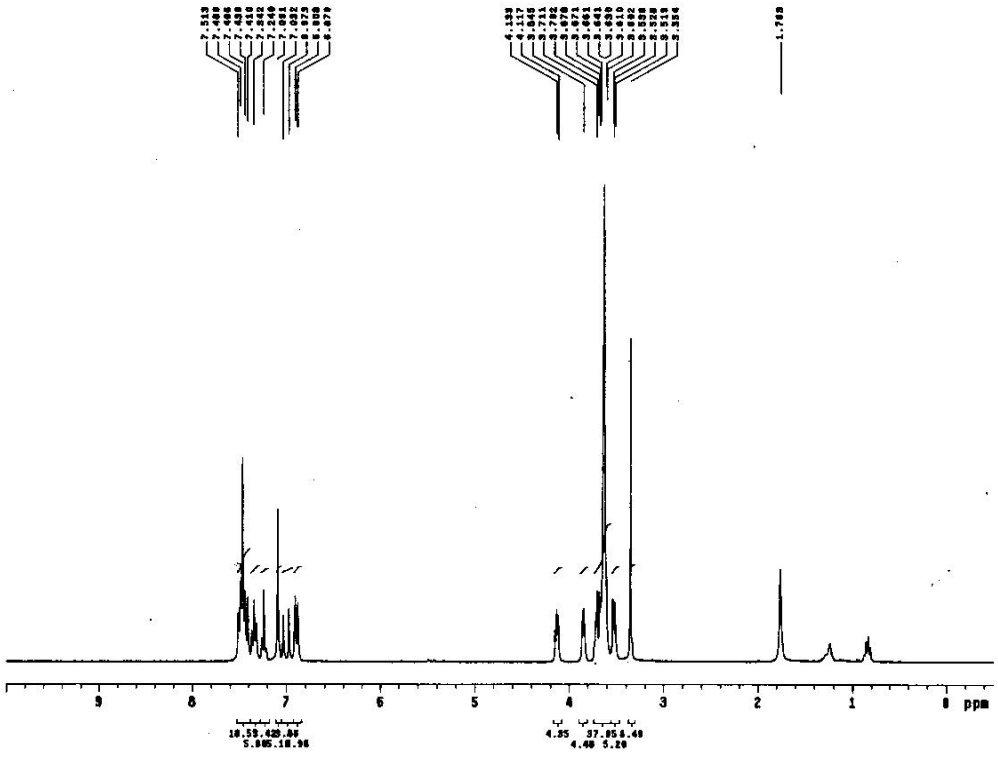

Figure 3.28 ^{1}H NMR spectrum of Compound 21

3.6.3 Steady-state Absorbance and Photoluminescence Spectroscopy:

Steady-state absorbance and photoluminescence measurements in various solvents were done for the OPV rod-coil compound **21** and the spectra are shown in Figure 3.29 (a) and (b), respectively. Fluorescence was quenched in the carbon tetrachloride solution. The SEM observation of the chloroform solution following standard procedure it is believed that the quenching of the fluorescence is due the nanoparticles formation, as shown in figure 3.30. The morphology of the nanoparticles is like vesicles. Thus it could be useful in the fluorescence on-off switching devices or sensors.

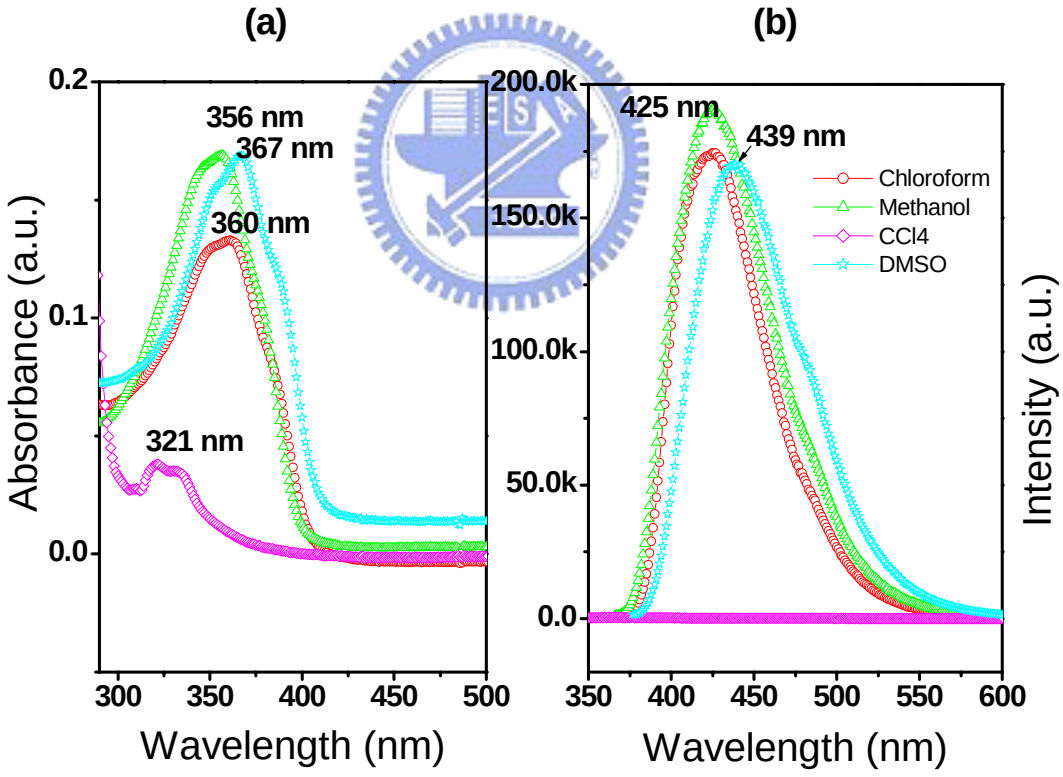

Figure 3.29 (a) UV-visible absorbance and (b) Photoluminescence spectra of 21 in different solvents

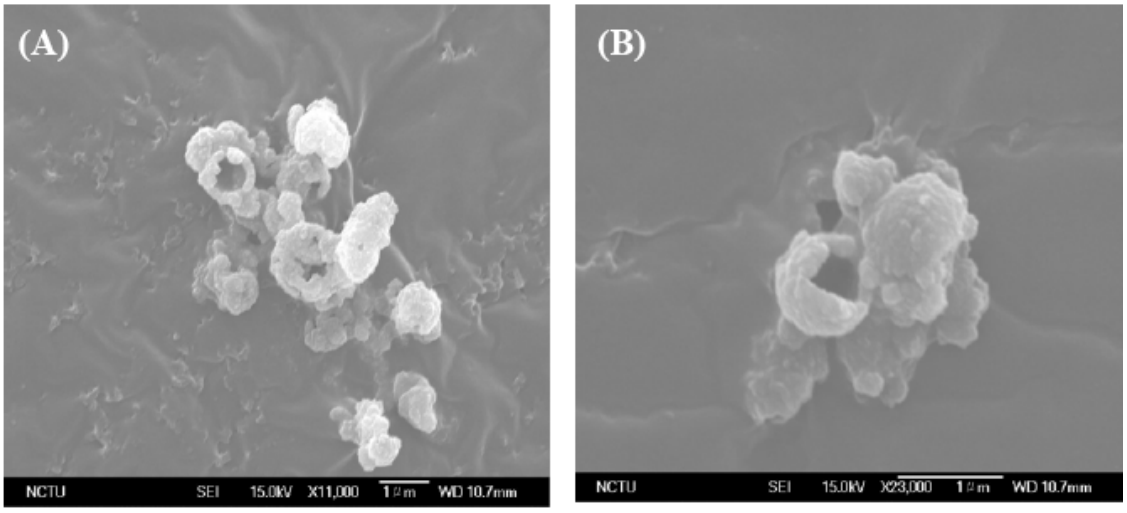

Figure 3.30 Scanning Electron Microscopy images of 21 in CCl_4 observed at (a) Lower magnification and (b) Higher magnification.

Conclusion

We synthesized a series of conjugated organic compounds, especially the oliogophenylene vinylene derivatives, and have observed the fascinating photophysical properties of their fluorescent organic nanoparticles and these were studied by several characterization techniques. These nanoparticles were prepared by reprecipitation in solutions of water and THF at various volume fractions.

We observed strong emission from PPB nanoparticles, but emission of free PPB in dilute solution was scarcely detectable. Furthermore, the fluorescent intensity of these nanoparticles increases with their size. Measurements of femtosecond fluorescence indicate that intramolecular nonradiative deactivation through torsional motions is efficient in PPB solution but inactive in DSB solution; intermolecular nonradiative deactivation through π–π interactions of carbon backbones is more efficient in DSB nanoparticles than in PPB nanoparticles. Such disparate dynamical behavior is inferred to reflect the dissimilar structures of PPB and DSB molecules in dilute solution and in nanoparticles. In this manner, we rationalize the nonfluorescent nature of the twisted PPB molecule in dilute solution and establish the concept that molecular planarity, geometrical rigidity, and loose packing produce strong fluorescent emission in PPB nanoparticles. A nearly planar geometry of molecules of PPB in the unit cell of a single crystal is confirmed by our XRD measurements. Moreover, powder XRD experiments demonstrate that two packing structures are involved in PPB nanocrystals: one forms aggregates according to a

herringbone-type arrangement as observed in a single crystal, whereas the other is not yet determined.

By comparing the time-resolved transients of CNDSB in THF and PMMA film, the excited dynamics of CNDSB were investigated. For CNDSB in THF, both the isomerization (0.91 ps) and vibrational relaxation (23.6 ps) processes were observed. However, in PMMA film, as the isomerization channel was blocked, we only observed the energy transfer process (31 ps). CNDSB molecules formed nanobelts as the volume fraction of the water exceeded 70%, and the size of the nanobelts increased with increase of water. In this study, we provided more direct evidence for the deactivation through intramolecular isomerization channel, and the result indicated that structural confinement also contributed parts of the enhancement in nanobelts. Measurements of femtosecond time-resolved fluorescence spectroscopy indicated that a unique ultra-fast energy transfer process existed in CNDSB nanobelts, and this might be useful in making quantum devices.

DSB-C8 shows bright blue fluorescence in solution state (THF) and it is observed that its absorbance in THF solution shows two bands with λ_{max} at 297 nm and other at 345 nm. For 60, 70 and 80% water volume fractions, at longer wavelength there observed mie-scattering which is attributed due to the formation of the larger structures which is evident from the SEM images. The nanostructures were started to form at 60% volume fractions of water addition. At 60%, worm-like micellar structures having lengths in about 100 nm were observed and as the water volume fraction was increased from 70 to 80%, theses worm-like micelles appeared to be accumulated or started to aggregate and form the granular nanostructures with the diameters roughly about 200-300 nm. The latter might be responsible for the mie-scattering of the absorbance and enhancement of the PL intensity.

Also we have prepared nanostructures of HPS of various types in solutions of water and THF using reprecipitation, and characterized their enhanced and color-tunable photophysical properties with steady-state and time-resolved spectral methods. We observed strong emission from well evolved HPS nanoaggregates, but emission from HPS in dilute THF solution was scarcely detectable. We discovered that novel nanoflowers were produced at 70% water with blue-shifted emission, λ_{em} = 462 nm, of which the intensity increased 100 times. At 80% solution, nanoglobular structures were formed at the expense of the nanoflowers, and the emission intensity was decreased significantly, but microglobular structures evolved from the nanoglobules at 90% water with intermediate emission intensity at λ_{em} = 500 nm. Picosecond time-resolved fluorescence investigations yielded mean lifetimes 4.6, 0.4 and 1.7 ns for 70, 80 and 90% solutions, respectively; the corresponding fluorescence quantum efficiencies were estimated to be 0.35, 0.03 and 0.13, respectively. The present study indicates that the observed enhancement of the emissions in various water/THF solutions of HPS is not only due to the AIE effect but also strongly depends on the morphologies of the nano/microstructures. Formation of the nanoflowers of HPS is perhaps the first example of any organic compound.

Along with this, we fabricated the nanoparticles of various shapes of amino-stilbene derivatives.

Rod-coil molecules with OPV derivatives as rods showed different sizes of the nanoparticles in water dispersions and they showed the size-dependent photophysical properties.

References:

[1] D. Horn, J. Rieger, *Angew. Chem. Int. Ed.* **2001**, *40*, 4330.

[2] S. Forrest, *MRS Bull.* **2001**, *26*, 108.

[3] E. A. Silinsh, *Organic Molecular Crystals: Their Electronic States*, Springer-Verlag, Berlin, **1980**.

[4] H. Yoshikava, H. Masuhara, *J. Photochem. Photobiol. C* **2000**, *1*, 57.

[5] D. S. Chemla, J. Zyss, *In Nonlinear Optical Properties of Organic Molecules and Crystals, Vol. 1*, Academic Press, Orlando, USA, **1987**.

[6] H. Oikawa, F. Kasai, H. Nakanishi, *Anisotropic Organic Materials, Vol. Chapter 12*, American Chemical Society, Washington, DC, **2002**.

[7] H. Kasai, H. S. Nalwa, H. Oikawa, S. Okada, H. Matsuda, N. Minami, A. Kakuta, K. Ono, A. Mukoh, N. H., *Jpn. J. Appl. Phys.* **1992**, *31*, L1132.

[8] H. B. Fu, J. N. Yao, *J. Am. Chem. Soc.* **2001**, *123*, 1434.

[9] B.-K. An, S.-K. Kwon, S.-D. Jung, S.-Y. Park, *J. Am. Chem. Soc.* **2002**, *124*, 14410.

[10] S. Li, L. He, F. Xiong, Y. Li, G. Yang, *J. Phys. Chem. B* **2004**, *108*, 10887.

[11] J. Luo, Z. Xie, J. W. Y. Lam, L. Cheng, H. Chen, C. Qiu, H. S. Kwok, X. Zhan, Y. Liu, D. Zhu, B. Z. Tang, *Chem. Commun.* **2001**, 1740.

[12] R. Deans, J. Kim, M. R. Machacek, T. M. Swager, *J. Am. Chem. Soc.* **2000**, *122*, 8565.

[13] R. J. Gehr, R. W. Boyd, *Chem. Mater.* **1996**, *8*, 1807.

[14] J. A. He, K. Yang, J. Kumar, S. K. Tripathi, L. A. Samuelson, T. Oshikiri, H. Katagi, H. Kasai, S. Okada, H. Oikawa, H. Nakanishi, *J. Phys. Chem. B* **1999**, *103*, 11050.

[15] H. Kasai, H. Kamatani, S. Okada, H. Oikawa, H. Matsuda, H. Nakanishi, *Jpn. J. Appl. Phys.* **1996**, *35*, L221.

[16] T. Onodera, H. Kasai, S. Okada, H. Oikawa, K. Mizuno, M. Fijitsuka, O. Ito, H. Nakanishi, *Opt. Mater.* **2002**, *21*.

[17] H. Oikawa, T. Mitsui, T. Onodera, H. Kasai, H. Nakanishi, T. Sekiguchi, *Jpn. J. Appl. Phys., Part 2* **2003**, *42*, L111.

[18] H. Katagi, H. Kasai, S. Okada, H. Oikawa, K. Komatsu, H. Matsuda, Z. Liu, *Jpn. J. Appl. Phys.* **1996**, *35*, L1364.

[19] K. Baba, H. Kasai, S. Okada, H. Oikawa, H. Nakanishi, *Opt. Mater.* **2002**, *21*, 591.

[20] S. Takahashi, H. Miura, H. Kasai, S. Okada, H. Oikawa, H. Nakanishi, *J. Am. Chem. Soc.* **2002**, *124*, 10944.

[21] H. B. Fu, B. H. Loo, D. B. Xiao, *Angew. Chem. Int. Ed.* **2002**, *41*, 962.

[22] D. I. Xiao, *J. Am. Chem. Sco.* **2003**, *125*, 6740.

[23] V. V. Volkov, T. Asahi, H. Masuhara, A. Masuhara, H. Kasai, H. Oikawa, H. Nakanishi, *J. Phys. Chem. B* **2004**, *108*, 7674.

[24] M. L. Ferrer, F. Monte, *J. Phys. Chem. B* **2005**, *109*, 80.

[25] B. Z. Tang, X. Zhan, G. Yu, P. S. Lee, Y. Liu, D. Zhu, *J. Mater. Chem.* **2001**, *11*, 2974.

[26] J. Chan, C. C. W. Law, J. Y. W. Lam, Y. Dong, S. M. F. Lo, I. D. Williams, D. Zhu, B. Z. Tang, *Chem. Mater.* **2003**, *15*, 1535.

[27] J. Chen, Z. Xie, J. W. Y. Lam, C. C. W. Law, B. Z. Tang, *Macromolecules.* **2003**, *36*, 1108.

[28] J. Chen, H. Peng, C. C. W. Law, Y. Dong, J. W. Y. Lam, I. D. Williams, B. Z. Tang, *Macromolecules* **2003**, *36*, 4319.

[29] H. Chen, J. W. Y. Lam, J. Luo, Y. Ho, B. Z. Tang, D. Zhu, M. Wong, H. S. Kwok, *Appl. Phys. Lett.* **2002**, *81*, 574.

[30] Y. Ren, J. W. Y. Lam, Y. Dong, B. Z. Tang, K. S. Wong, *J. Phys. Chem. B* **2005**, *109*, 1135.

[31] Y. Ren, Y. Dong, J. W. Y. Lam, B. Z. Tang, K. S. Wong, *Chem. Phys. Lett.* **2005**, *402*, 468.

[32] C. Liu, W. Yang, Y. Mo, Y. Cao, J. Chen, B. Z. Tang, *Synth. Met.* **2003**, *135-136*, 187.

[33] Y. Dong, J. W. Y. Lam, Z. Li, H. Tong, C. C. W. Law, X. D. Feng, B. Z. Tang, *Poly. Mater.: Science & Engg.* **2004**, *91*, 707.

[34] Y. Dong, J. W. Y. Lam, Z. Li, H. Peng, C. C. W. Law, X. D. Feng, B. Z. Tang, *Polym. Prepr.* **2004**, *45*, 823.

[35] M. H. Lee, D. Kim, Y. Dong, B. Z. Tang, *J. Kor. Phys. Soc.* **2004**, *45*, 329.

[36] M. Lee, B.-K. Cho, W.-C. Zin, *Chem. Rev.* **2001**, *101*, 3869.

[37] J. E. G. J. Wijnhoven, W. L. Vos, *Science* **1998**, *281*, 802.

[38] A. Imhor, D. J. Pine, *Nature* **1997**, *389*, 948.

[39] J. D. Joannopoulos, P. R. Villeneuve, S. Fan, *Nature* **1997**, *386*, 143.

[40] G. M. Whitesides, *Science* **1991**, *254*, 1312.

[41] J. M. Lehn, *Supramolecular Chemistry*, VCH, Weiheim, Germany, **1995**.

[42] M. Muthukumar, *Science* **1997**, *277*, 1225.

[43] S. Foster, *Adv. Mater.* **1998**, *10*, 195.

[44] J. N. Israelachvili, *Intermolecular and Surface Forces*, Academic Press, London, **1992**.

[45] S. A. Jenekhe, X. L. Chen, *Science* **1999**, *283*, 372.

[46] S. A. Jenekhe, X. L. Chen, *Science* **1998**, *279*, 1903.

[47] C. Bianchi, E. Cecchetto, B. Francois, *Synth. Met.* **1999**, *102*, 916.

[48] M. Grell, D. D. C. Bradley, *Adv. Mater.* **1999**, *11*, 895.

[49] D. H. Hwang, H. K. Shim, *Thin Solid Films* **2002**, *417*, 166.

[50] D. T. McQuade, J. Kim, T. M. Swager, *J. Am. Chem. Sco.* **2000**, *122*, 5885.

[51] J. Kim, I. A. Levitsky, D. T. Maquade, T. M. Swager, *J. Am. Chem. Sco.* **2002**, *124*, 7710.

[52] A. P. H. J. Schenning, E. Peeters, E. W. J. Meijer, *J. Am. Chem. Sco.* **2000**, *122*, 4489.

[53] F. Cacialli, R. H. Friend, W. J. Feast, P. W. Lovenich, *Chem. Comm.* **2001**, 1778.

[54] A. Ajayaghosh, S. J. George, V. K. Praveen, *Angew. Chem. Int. Ed.* **2003**, *42*, 332.

[55] T. Q. Nguyen, R. Y. Yee, B. J. Schwartz, *J. Photochem. Photobiol. A* **2001**, *144*, 21.

[56] H. E. Katz, S. F. Bent, W. L. Wilson, M. L. Schilling, S. B. Ungashe, *J. Am. Chem. Sco.* **1994**, *116*, 6631.

[57] A. P. H. J. Schenning, P. Jonkheijm, E. Peeters, E. W. Meijer, *J. Am. Chem. Sco.* **2001**, *123*, 409.

[58] C. Lowe, C. weder, *Adv. Mater.* **2002**, *14*, 1625.

[59] D. S. Seferos, D. A. Banach, N. A. Alcantar, J. N. Israelachvili, G. C. Bazan, *J. Org. Chem.* **2004**, *69*, 1110.

[60] M. R. Robinson, S. J. Wang, A. J. Heeger, G. C. Bazan, *Adv. Funct. Mater.* **2001**, *11*, 413.

[61] T. Goodson, W. Li, A. Gharavi, L. Yu, *Adv. Mater.* **1997**, *9*, 639.

[62] Y. Tao, A. Donat-Bouillud, M. D'Iorio, J. Lam, T. C. Gorjanc, C. Py, M. S. Wong, Z. H. Li, *Thin Solid Films* **2000**, *363*, 298.

[63] M. Era, J. Koganemaru, T. Tsuitsui, A. Watakabe, T. Kunitake, *Synth. Met.* **1997**, *91*, 83.

[64] J. F. Hulvat, M. Sofos, K. Tajima, S. I. Stupp, *J. Am. Chem. Sco.* **2004**, *127*, 366.

Chapter 4
Introduction and Background

New technologies based on nanoscale machines and devices are gaining much attention in twenty first century. Key to the realization of this nanotech world are simple, efficient methods of organizing materials (molecules, molecular clusters, polymers, or, generally speaking, building blocks) into precise, predetermined nanostructures that can be preserved in a robust engineering form. Nature abounds with intricate composite architectures composed of hard and soft materials synergistically interwined to provide both useful functionality and mechanical integrity. For example, marine organisms like diatoms and radiolaria preserved in silica or calcium carbonate. Recent synthetic efforts to mimic such natural designs have focused on nanocomposites,[1-5] prepared mainly by slow procedures like monomer or polymer infiltration of inorganic nanostructures,[6, 7] or sequential deposition.[8, 9] Natural materials such as bone and shell teach us that combining hard and soft materials in periodic architectures over multiple length scales can result in composite materials with enhanced mechanical properties such as toughness, strength and hardness.[10] Since the recent development of organic templating growth of materials, new types of hybrid photonic composite materials whose structure and function are organized hierarchically are emerging. Ordered periodic mesoscopic materials allow the construction of composites with many guest types like organic molecules or polymers. These guest/host materials combine high

stability of the inorganic host system, new structure forming mechanism due to the confinement of guests in well-defined pore channels, and a modular composition.

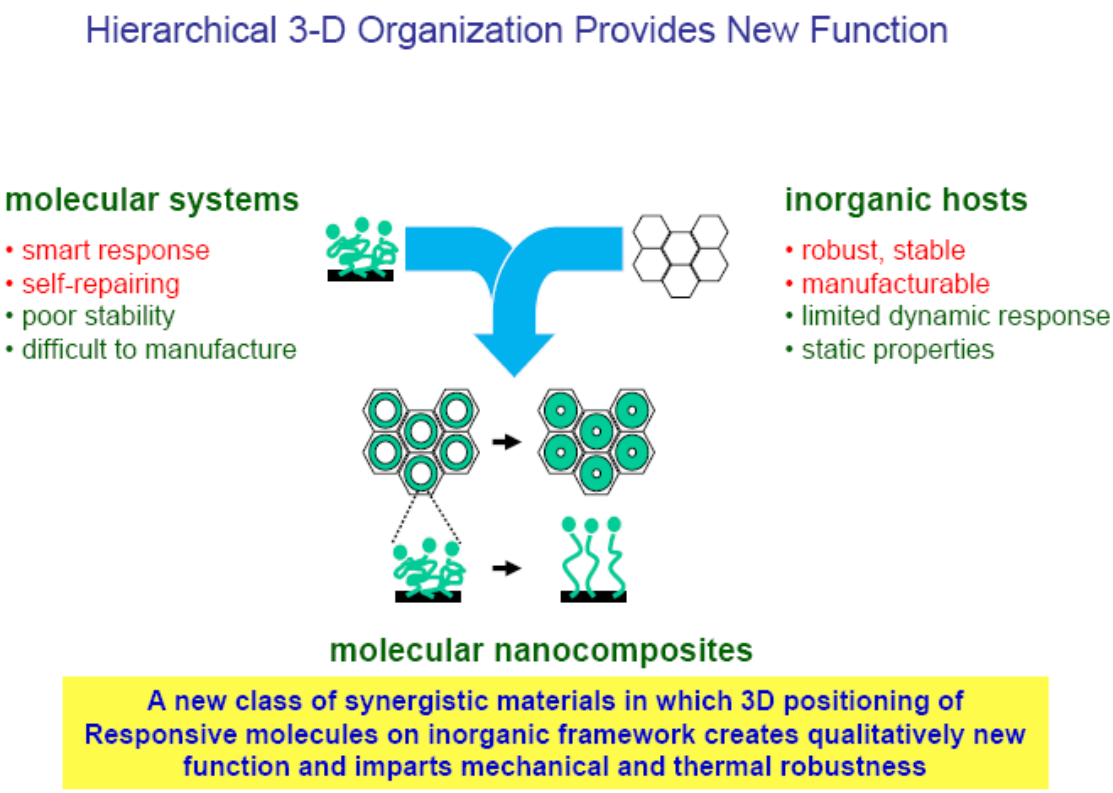

Scheme 4.1 Hierarchical 3-D Organization of Organic-Inorganic Functions

Preparation methods, properties, and possible applications of chromophores in porous silica, molecular sieves, and minerals have been summarized in a review article.[11] Inclusion of the dye molecules such as Coumarin 40, Rhodamine BE50, Oxazine 1 inside the nanopores has been demonstrated by

Schulz-Ekloff's group.[12-14] Several papers reported on this topic have demonstrated the optimization of the concentration of the dye molecules incorporated within the mesopores. These methods were either inclusion of the dye molecules within pre-formed mesopores or during sol-gel synthesis. At only moderate concentration of the dye these showed an increase in the photoluminescence intensity.[15-17] Nanocomposites that contain conjugated polymers confined within a silica matrix show enhanced conductivity, mechanical strength, processability, environmental stability, and other unique properties[18] that allow for potential use in light emitting diodes, information storage devices, optical signal processors, and sensors. To name a few, nanocomposites formation of polymers such as poly(phenylene vinylene),[19] polyaniline,[20] polydiacetylene,[21] poly(2,5-thienylene ethynylene),[18] polythiophene, polypyrrole, and polyacetylene[22, 23] have been reported. Several synthetic efforts to obtain such nanocomposites, were mainly by slow procedures like monomer or polymer infiltration of inorganic nanostructures,[6, 7, 19, 24, 25] or sequential deposition.[8, 9] Such nanocomposites are heterogeneous, exhibiting two distinct conjugated polymer environments, that is, polymers inside and outside the hexagonally arranged pore channels of the silica particles. However, self-assembly, one of the few practical strategies for making ensembles of nanostructures provides one solution to the fabrication of ordered aggregates from components with sizes from nanometers to micrometers.[26] It typically employs asymmetric molecules that are pre-programmed to organize into well-defined supramolecular assemblies and is the spontaneous organization of materials (micelles) through noncovalent interactions free of external intervention,[27] into periodic hexagonal, cubic, or lamellar mesophases. Amhiphilic surfactant molecules or polymers bearing hydrophilic and

hydrophobic parts are most common. Despite excellent control of pore size, early mesoporous materials, after the pioneering works by Mobil on surfactant-templated materials,[28] were made in the form of powders, precluding their use in thin film applications like membranes, catalysts, etc. For many envisioned nanotechnologies, it would be desirable to create patterned nanocomposites consisting of periodic arrangements of two or more dissimilar materials. Stable, supported, mesoporous silica films were prepared by evaporation induced self-assembly (EISA) and was first reported by Ozin's[29] and Brinker's[27, 30] group. These films can be processed into porous or composite mesostructures of potential utility for a variety of applications such as membranes,[31] sensors,[32] waveguides,[33] lasers,[14, 33, 34] low dielectric constant (low *k*) insulators[35, 36] and other still evolving fields of activities. More recently, Okabe et al[37] demonstrated the immobilization and tuning of one-dimensional columnar charge-transfer (CT) assemblies in mesoporous silica films consisting of hexagonal array of nanoscopic channels. Fabrication and characterization of multiply doped nanostructured silicate sol-gel thin films have been reported.[38, 39] Brinker et al reported the self assembly of conjugated polymer/silica nanocomposite films with hexagonal, cubic or lamellar mesoscopic order using polymerizable amphiphilic diacetylene molecules as both structure directing agents and monomers.[40]

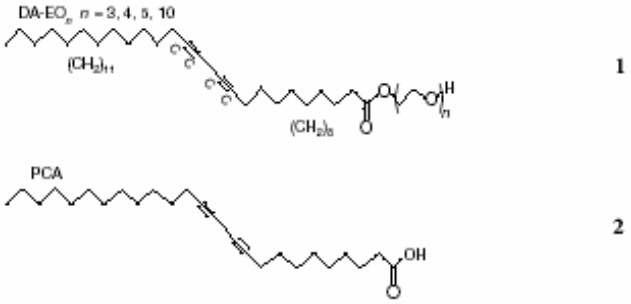

Scheme 4.2 Chemical structures of oligoethylene glycol functionalized diacetylenic (DA-EO$_n$) surfactants (1) and 10,12-Pentacosadiynoic acid (2).

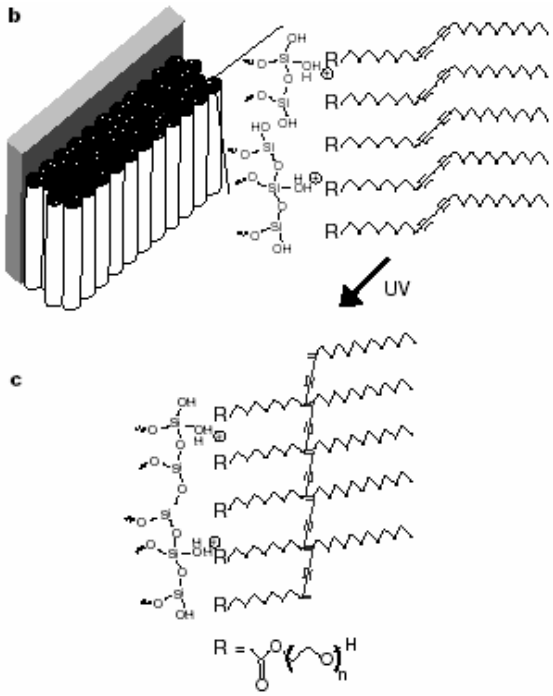

Figure 4.1 b) Hexagonal mesostructure and hypothetical arrangement of DA surfactants adjacent to the cylindrically structured silicic acid framework. c) Hypothetical structure of polymerized PDA/silica nanocomposite formed upon exposure to UV light and continued acid-catalysed siloxane condensation.

Polymerization results in polydiacetylene /silica nanocomposites that are optically transparent and mechanically robust.

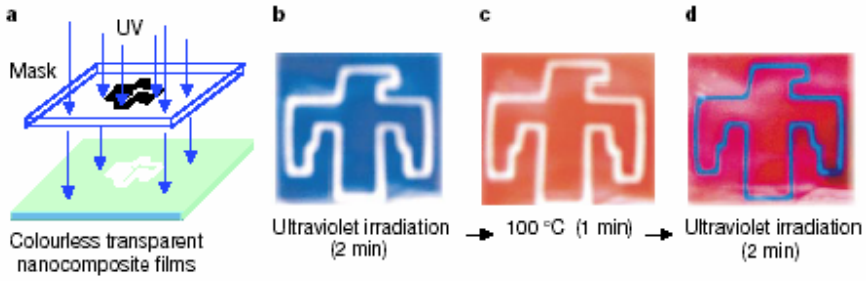

Figure 4.2 Patterned polymerization induced by UV irradiation and the thermochromic and solvatochromic transition of a hexagonal PDA/silica nanocomposite film.[21]

The self assembly procedure is rapid and incorporates the organic monomers uniformly within a highly ordered, inorganic environment. In aqueous solution above the critical micelle concentration (cmc), surfactants assemble into micelles, spherical, or cylindrical structures that maintain the hydrophilic parts of the surfactant in contact with water while shielding the hydrophobic parts within the micellar interior (see Fig.).[41] Further increases in surfactant concentration result in the self-organization of micelles into periodic hexagonal, cubic, or lamellar mesophases. Obviously such detergent mesophases do not themselves represent robust engineering materials suitable for nanotechnologies. However in 1992 Mobil researchers discovered that surfactant self-assembly conducted in aqueous solutions of soluble silica species results in spontaneous co-assembly of silica-surfactant mesophases. Surfactant removal creates periodic mesoporous solids, essentially silica fossils of the liquid crystalline assembly as shown in figure. Over the last few years, this pioneering work has been extended to produce a

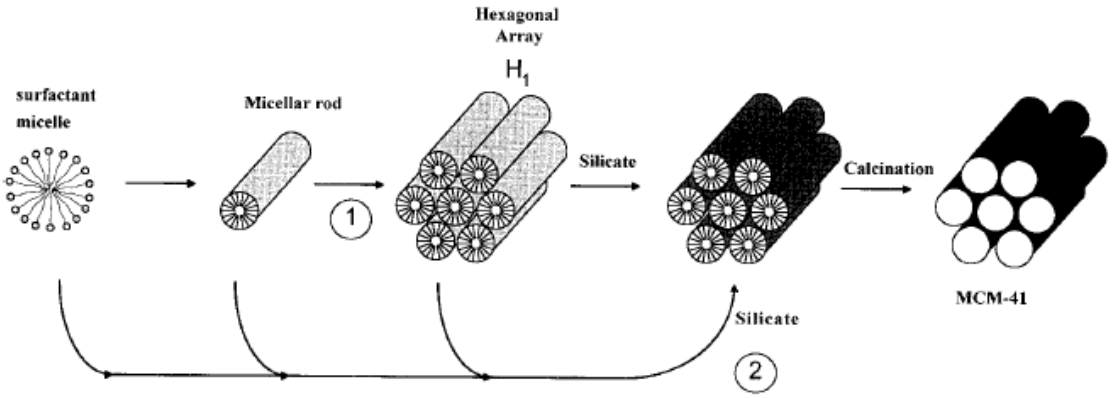

Figure 4.3 Schematic of the liquid-crystal templating (LCT) mechanism. Path 1 is liquid crystal initiated and 2 is silicate anion initiated.[41]

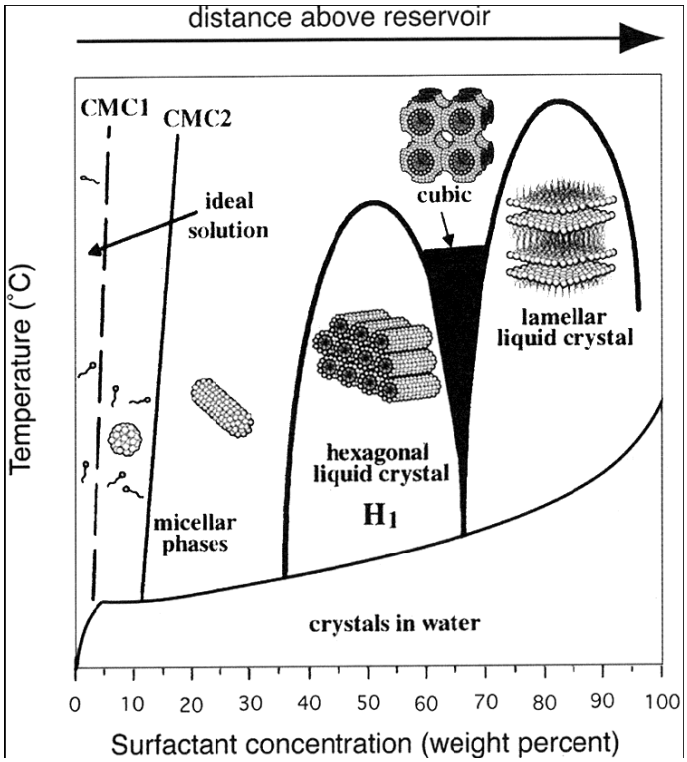

Figure 4.4 Schematic phase diagram for CTAB surfactant in water. Arrow denotes evaporation-driven pathway during dip-coating, aerosol processing, etc. Raman et al.[41]

wide compositional range of mesoporous solids, and, using a variety of surfactants, the pore sizes have been varied in the approximate range, 1 nm to over 10 nm.[42-44]

Consideration of above figure in the context of sol-gel dip-coating suggests an alternative route to the formation of thin film mesophases. Beginning with a homogenous solution of soluble silica and surfactant prepared in ethanol/water solvent with c_o << cmc, preferential evaporation of ethanol concentrates the depositing film in water and nonvolatile surfactant and silica species (Figure 4.4). The progressively increasing surfactant concentration drives self-assembly of silica-surfactant micelles and their further organization into liquid-crystalline mesophases.[45]

Dip-coating scheme depicted in the following Figure represents a rapid (~10s), dynamic self-assembly process conducted in a rather steep concentration gradient. Its steady, continuous nature promotes continuous accretion of micellar or perhaps liquid-crystalline species onto interfacially organized mesostructures. Large, liquid-crystalline domains grow progressively inward from solid-liquid and liquid-vapor interfaces (with increasing distance above the reservoir surface, Figure 4.4). Deposited films are optically transparent and completely featureless on the micrometer-length scale.

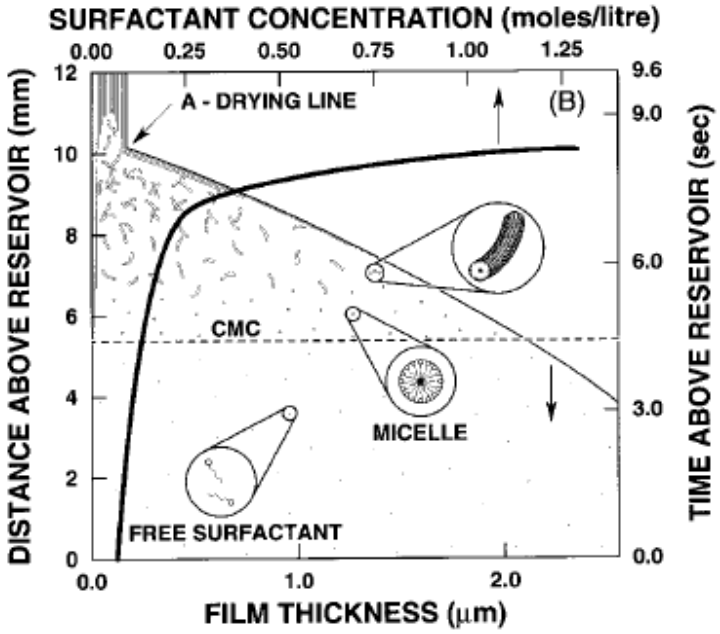

Figure 4.5 Steady-state film thinning profile established during dip-coating of a complex fluid comprising soluble silica, surfactant, alcohol, and water. Initial surfactant concentration c_o << cmc. Surfactant concentration increases with distance above the reservoir surface.

Nanocomposite self-assembly[5] represents an extension of the EISA process described above. Using the generic detergent diagram shown in the following Figure as a conceptual guide, we can consider as oil a wide variety of hydrophobic, organic precursors and reagents (monomers, crosslinkers, oligomers, functionalized polymers, initiators, etc.). In a process not so unlike washing dishes, we use micelle formation to spatially separate and organize organic precursors (sequestered within the hydrophobic micellar interiors) and inorganic precursors (organized around the hydrophilic micellar exteriors). Further self-organization of micelles into periodic hexagonal, cubic, or lamellar mesophases simultaneously positions both the organic and inorganic precursors into precise 3-D arrangements. Combined

organic/inorganic polymerization locks in the nanocomposite architecture and covalently bonds the organic/inorganic interface. The beauty of this approach is its simplicity and efficiency: if we seek to prepare laminated organic/inorganic composites, many hundreds of alternating organic/inorganic layers can be assembled in seconds. During nanocomposite self-assembly, a homogeneous solution of soluble silicates, surfactant, organic monomers, and photo or thermal initiators prepared in ethanol/water or THF/water solvent with c_o << cmc is prepared. During coating, preferential evaporation of ethanol (used initially to solubilize the organic precursors and homogenize the solution), progressively enriches the concentrations of water, HCl and the nonvolatile solution constituents within the depositing film.[45] As confirmed by optical probe studies, the increasing concentrations of surfactant and water cause the surfactant concentration to exceed the cmc, resulting in micelle formation and concurrent partitioning of the organic precursors and initiators into the micellar interiors and the inorganic precursors surrounding the micellar exteriors. Continuous evaporation promotes co-assembly of these species into liquid-crystalline mesophases, thereby simultaneously organizing both the organic and inorganic precursors into the desired laminated form.

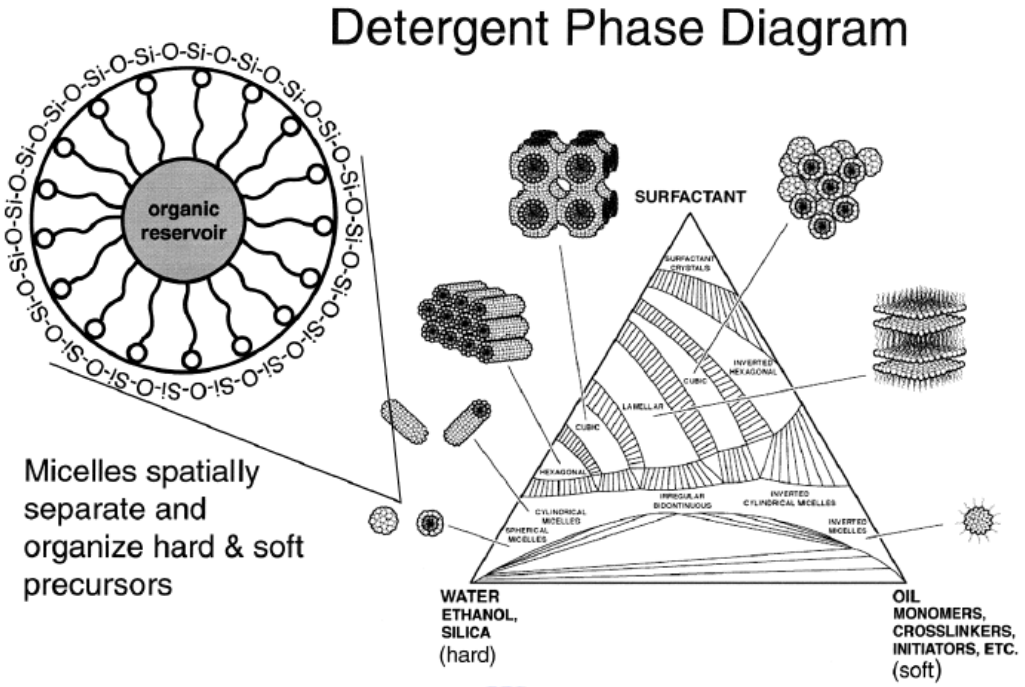

Figure 4.6 Schematic detergent (surfactant-oil-water) phase diagram. With the introduction of hydrophobic organic (or generally soft) precursors and hydrophilic inorganic (or generally hard) precursors, organic constituents partition within the hydrophobic micellar interiors, while inorganic constituents are organized around the micellar exteriors. Evaporation promotes further self-assembly into liquid-crystalline mesophases, simultaneously organizing organic and inorganic precursors into nanocomposite architectures.

According to Whitesides,[26] there are two main kinds of self-assembly: static and dynamic. Most research in self-assembly has focused on the static type. For example, molecular crystals are formed by static self-assembly; so are most folded, globular proteins. In static self-assembly, formation of the ordered structure may require energy (for example in the form of stirring), but once it is formed, it is stable.

Common Features of Self-assembly: Self-assembly reflects information coded (as shape, surface properties, charge, polarizability, magnetic dipole, mass, etc.) in indivisual components; these characteristics determine the interaction among them. The design of components that organize themselves into desired patterns and functions is the key to applications of self-assembly.

Because self-assembly requires that the components be mobile, it usually takes place in fluid phases or on smooth surfaces. The environment can modify the interactions between the components; the use of boundaries and other templates in self-assembly is particularly important, because templates can reduce defects and control structures.

Table: Examples of self-assembly (S, static, D, dynamic, T, templated, B, biological).[26]

System	Type	Applications/importance
Atomic, ionic, and molecular crystals	S	Materials, optoelectronics
Phase-separated and ionic layered polymers	S	
Self-assembled monolayers (SAMs)	S, T	Microfabrication, sensors, nanoelectronics
Lipid bilayers and black lipid films	S	Biomembranes, emulsions
Liquid crystals	S	Displays
Colloidal crystals	S	Band gap materials, molecular sieves
Bubble rafts	S	Models of crack propagation
Macro- and mesoscopic structures (MESA)	S or D, T	Electronic circuits
Fluidic self-assembly	S, T	Microfabrication
"Light matter"	D, T	
Oscillating and reaction-diffusion reactions	D	Biological oscillations
Bacterial colonies	D, B	
Swarms (ants) and schools (fish)	D, B	New models for computation/optimization
Weather patterns	D	
Solar systems	D	
Galaxies	D	

Present and Future Applications of Self-assembly:

Self-assembly is already a widely (if unwittingly) applied strategy in synthesis and fabrication (Table). Perhaps, one can predict areas where self-assembly will be used in the future. These are possibilities:[26]

(1) *Crystallization at All Scales*. The formation of regular, crystalline lattices is a fundamental process in self-assembly, and is a method to convert ;100-nm particles into photonic materials;[46] using micrometerscale components may lead to new routes to microelectronic devices.[47]

(2) *Robotics and Manufacturing*. Robots are indispensable to current systems for manufacturing. As components become smaller, following the trend in miniaturization through microfabrication to nanofabrication, conventional robotic methods will fail because of the difficulty in building robots that can economically manipulate components only micrometers in size. Self-assembly offers a new approach to the assembly of parts with nano- and micrometer dimensions.

(3) *Nanoscience and Technology*. There are two approaches to the fabrication of nanosystems: bottom-up and top-down. Chemical synthesis is developing a range of methods for making nanostructures—colloids, nanotubes, and wires—to use in bottom- up approaches. Self-assembly offers a route for assembling these components into larger, functional ensembles.

(4) *Microelectronics*. The fabrication of microelectronic devices is based almost entirely on photolithography, an intrinsically two-dimensional technology. Another computer of great interest—the brain—is three-dimensional. There are no clear strategic paths from two-dimensional to three-dimensional technology (and, of course, no absolute certainty that three-dimensional microelectronic devices will be useful, although the brain is certainly a three-dimensional system, and three dimensionality offers, in

principle, the advantages of short interconnects and efficient use of volume). Self-assembly offers a possible route to three-dimensional microsystems.

(5) *Netted Systems*. At the outer limits of self-assembly, at least as it is currently defined in the physical and biological sciences, are netted systems: computers, sensors, and controllers that interact with one another only through the flow of bits and configure (or self-assemble) themselves based on that flow into functional systems. These netted information systems will be entirely different in their realization from self-assembled aggregates of material components, but will share underlying concepts of design and architecture.

Chapter 5

Experimental Section

5.1 Instrumental Techniques (Characterization Methods):

The instrumental techniques we used for the characterization of the materials are summarized below.

5.1.1 Nuclear Magnetic Resonance (NMR):

^{1}H NMR spectra were recorded on Unity-300 spectrometer at 300 MHz for samples in $CDCl_3$, *d*-Acetone, *d*-Methanol solutions.

5.1.2 Scanning Electron Microscopy (SEM):

Images were acquired on a field-emission scanning electron microscope-JSM-6500 F, JEOL. To enhance the conductivity of the specimen, a layer of platinum was sputtered (current 30 mA, pressure 4 Pa, duration 30 s).

5.1.3 Tunneling Electron Microscopy (TEM):

TEM micrographs and EDS experiments were carried under AEM/EDS JEOL, JEM-2010 using copper grid having lasey carbon as the substrate.

5.1.4 Steady State UV/visible Absorption and Photoluminescence spectra (PL):

UV-Visible absorption spectra were recorded on Hewlett-Packard HP8453 spectrometer and Cary 50 Varian and Photoluminescence spectra were obtained on a SpectraPro-150 with Muller SVX 1450 xenon lamp.

5.1.5 X-ray Diffraction Measurements:

X-ray diffraction measurements for nanocomposite films were done with a diffractometer (Bede D1 type) with $Cu_{K\alpha}$ radiation at $\lambda = 1.54056$ Å.

5.1.6 Fourier Transfer Infra-Red (FTIR) Spectroscopy:

FT-IR spectra were recorded on PerkinElmer Spectrum One instrument.

5.2 Synthetic Procedures:

Emission Enhancement *via* Formation of 'Controlled' Aggregations in the Hybrid Chromophoric Surfactant Amphiphile/Silica Self-assembled Nanocomposites

Synthesis of Terphenyl chromophore amphiphile (PPP-C11):

5.2.1 4-Biphenylboronic acid (22):

To a cooled solution (-78°C) of 4-bromobiphenyl (9.3 g, 40 mmol) in 100 mL dry THF, was added dropwise, 16 mL of a 2.5 M solution of *n*-BuLi in hexane. This mixture was stirred and kept at -78°C for 2.5 h. Color of the solution became green to pale white. A solution of tri-isopropyl borate (15.0 g, 80 mol) was slowly added over 30 minutes after which the reaction mixture was allowed to warm up to room temperature overnight. The resulting greenish yellow mixture was acidified with 60 mL of a 10% HCl solution and stirred for 16 h at room temperature. The crude product was extracted into diethyl ether (3 x 100 mL), and washed successively with a concentrated sodium carbonate solution and water. The ether was removed

by distillation and the crude product was recrystallized twice from a water/ethanol mixture (95/5). The crystals were dried under vacuum overnight at 60°C to obtain 6.0 g (76%) of off-white 4-biphenylboronic acid.

^{1}H NMR (300 MHz, Acetone-d_6): δ= 7.98 (d, 2H; ArH), 7.68 (t, 4H; ArH), 7.48 (t, 2H, ArH), 7.43 (d, 1H, ArH), 7.38 (s, 2H, -B(OH)$_2$).

5.2.2 I-Phenyl-C11 (23):

p-Iodophenol (6.0 g, 29.7 mmols) and K_2CO_3 (5.1 g, 37.1 mmols) were mixed in dimethylformamide (DMF) and stirred for 30 min. Resulting solution turned reddish. To it was added 11-Bromo-1-undecanol (7.45 g, 29.7 mmol) and the reaction mixture was stirred and heated at 60°C for one day. Milky white solution thus obtained was acidified by dilute HCl and then extracted with CH_2Cl_2/water. The organic layer was washed with saturated NaCl solution, dried over $MgSO_4$. Dichloromethane was evaporated in vacuo and solid obtained was recrystallized from ethyl acetate to give white product (82%).

^{1}H NMR (300 MHz, $CDCl_3$) δ= 7.52 (d, 2H; ArH), 6.65 (d, 2H; ArH), 3.88 (t, 2H; -OCH$_2$), 3.61 (t, 2H; -CH$_2$), 1.73 (m, 2H; -CH$_2$), 1.54 (m, 2H; -CH$_2$), 1.51-1.27 ppm (m, 14H; -CH$_2$).

5.2.3 Terphenyl chromophore amphiphile (PPP-C11) (24):

22 (0.5 g, 2.6 mmols) and **23** (1 g, 2.5 mmols) were mixed in dimethoxyethane (DME) and stirred in round bottom flask under nitrogen atmosphere. After about 10 min, when the mixture turned brownish, 2M Na_2CO_3 (0.57 g, 5.37 mmol) solution in water was added. After a few minutes, solution turned black. It was heated at 85°C under nitrogen for two days. The mixture was then acidified with dilute HCl and extracted with

dichloromethane and water. Organic layer was washed with saturated NaCl and dried over $MgSO_4$ and the solvent was evaporated in vacuo. After double recrystallization of the crude from chloroform, a pale white product **24** was obtained (Yield= 62%).

^{1}H NMR (300 MHz, $CDCl_3$) δ= 7.70 (d, 2H; ArH), 7.65 (t, 3H; ArH), 7.45 (m, 4H; ArH), 7.43 (m, 2H; ArH), 6.98 (d, 2H; ArH), 3.98 (t, 2H; -OCH_2), 3.62 (t, 2H; -C$\underline{H_2}$-OH), 1.77 (m, 2H; -CH_2), 1.53-1.29 ppm (m, 14H; -CH_2), EI-MS (32, 41, 55, 246, 306, 416).

Synthesis of Fluorene-Stilbene chromophore amphiphile (FL-Stilbene-(C11)$_2$):

5.2.4 FL-(C11)$_2$ (25):

Tetrabutylammonium chloride (TBACl) (0.08 g, 12.34 mmol) was added in 50 wt% NaOH in water and heated at 70^{o}C. 11-Bromo-1-undecanol (3.1 g, 12.34 mmol) was added to it after some time. Then 2, 7-dibromofluorene (2 g, 6.17 mmol) in THF was slowly added to the mixture, stirred and heated at 70^{o}C for two days. After cooling the reaction mixture to room temperature, THF was removed on rotar. The mixture was poured into water and acidified with dilute HCl and then extracted with ethyl acetate. Organic phase was washed with saturated NaCl, dried over $MgSO_4$ and after removing EA on rotar, crude was obtained. The product was purified by column chromatography (SiO_2, 20% EA/Hexane) to give 2.5 g (60.8%) highly viscous oil. ^{1}H NMR (300 MHz, $CDCl_3$) δ= 7.47 (d, 2H; ArH), 7.42 (d, 4H; ArH), 3.57 (t, 4H; -C$\underline{H_2}$OH), 2.49 (q, 4H; -CH_2), 1.87 (m, 4H; -CH_2), 1.50 (m, 4H; -CH_2), 1.23-0.97 ppm (m, 28H; -CH_2).

5.2.5 FL-Stilbene-(C11)$_2$ (26):

Compound **25** (1 g, 0.9 mmol), styrene (0.24 g, 2.4 mmol), palladium (II) acetate (0.004 g, 0.02 mmol), tri-*o*-toluene phosphine (0.01 g, 0.04 mmol) and triethylamine (0.57 g, 7.7 mmol) were heated at 90^{o}C for one day in a hard glass tube sealed under nitrogen. The reaction mixture was allowed to cool to room temperature and after evaporating triethylamine on rotar, was extracted with dichloromethane, water and saturated NaCl. Organic phase was dried over $MgSO_4$ and the solvent was evaporated in vacuo. The product (Yield= 67%) was obtained by column chromatography (SiO_2, 3:7 EA/Hexane). ^{1}H NMR (300 MHz, $CDCl_3$) δ = 7.63 (d, 2H,), 7.54 (m, 6H, ArH), 7.38 (m, 4H; ArH), 7.27 (d, 4H; ArH), 7.17 (d, 4H; =CH), 3.55 (t, 4H; -C$\underline{H_2}$OH), 1.99 (m, 4H; -CH_2), 1.46 (t, 4H; -CH_2), 1.23-1.03 ppm (m, 32H; -CH_2). MS (366, 369, 395, 540, 711).

5.2.6 Chromophore amhiphile/silica hybrid nanocomposites formation by evaporation-induced self-assembly (EISA):

Precursor solutions were synthesized from tetraethyl orthosilicate (TEOS, $Si(OC_2H_5)_4$), chromophoric amphiphiles (PPP-C11 and FL-Stilbene-$(C11)_2$), and HCl catalyst prepared in ethanol/water solvent. The final reactant mole ratio for nanocomposites prepared from PPP-C11 and FL-Stilbene-C11, were 1 TEOS:30 ethanol:5 H_2O: 0.1 HCl: 1 PPP-C11 and 1 TEOS:30 ethanol:5 H_2O: 0.1 HCl: 0.5 FL-Stilbene-$(C11)_2$, respectively. In a typical preparation, TEOS, ethanol, water and dilute HCl were stirred and heated at 35^{o}C for half an hour. To this solution was added the chromophoric surfactant in ethanol and stirred for three hours. Films were prepared on quartz by evaporative spin-coating (1,500 r.p.m.), or dip-coating (at a rate of 30 cm min^{-1}). During deposition, preferential evaporation of THF concentrates the depositing film in water and nonvolatile silica and

chromophoric surfactant. The progressively increasing surfactant concentration drives self-assembly of chromophore amphiphile/silica micelles and their further organization into ordered liquid crystalline mesophases.

Bergman Cyclopolymerization within the Channels of Functional Hybrid Nanocomposite Formed by Self-assembly of Silica and Polymerizable Surfactant Monomer

Synthesis of biphenyl with ortho-diacetylene groups (A Bergamn Monomer):

5.2.7 Synthesis of 1,2-Dibromo-4-nitrobenzene (27):

Concentrated sulphuric acid (63 mL) was added drop-wise into the beaker containing conc. nitric acid (63 mL) kept in ice bath. 20 g (84.77 mmols) of 1,2-dibromobenzene was taken in 100 mL RBF which was also kept in ice-bath in which NaCl was added. To this solution fuming nitric acid prepared was added drop-wise with stirring. Keep and stir this mixture for 30 minutes. An oily layer was formed in the solution. So this mixture was heated at about 65^{o}C for almost an hour on oil-bath and then allowed it to cool for few minutes. Then it was immediately poured into ice and formation of a milky solution was observed and solid was settled at the bottom. It was kept as it is for some time and then it was filtered and washed by water. Then above solid was kept for drying at high vacuum.

Recrystallization: The solid formed was dissolved in methanol after heating at around 50^{o}C; a clear solution was formed. Then after cooling at

room temperature or keeping in ice bath, it formed nice long whitish needle-like crystals of 1,2-dibromo-4-nitrobenzene (**27**). It is better to follow slow cooling procedure to get good crystals. Methanol was removed by filtration and crystals were kept at high vacuum to remove adsorbed methanol.

^{1}H NMR (300 MHz, $CDCl_3$) δ = 8.48 (d, 1H, ArH), 8.04 (m, 1H, Ar-H), 7.82 (d, 1H, Ar-H)

5.2.8 Synthesis of 3,4-Dibromoaniline (28):

3,4-dibromobenzene (8 g, 28.47 mmols) was taken in a RBF to which was added absolute ethanol and was warmed to dissolve. A clear yellow solution was formed. To this solution was added 32 g (142.3 mmols) tin chloride dehydrate-$SnCl_2.2H_2O$. The solution was stirred and heated 70^{o}C on oil-bath for about 2 h; then it was poured into the ice. The aqueous phase was adjusted to pH=9 with 2N NaOH which was added drop-wise to the above solution and while adding the solution became milky white and precipitate was formed. This was extracted with ether and ether layer was dried on $MgSO_4$, filtered and ether was removed on rotar and solid obtained was kept at high vacuum to remove the traces of solvent. The crude product (3,4-dibromoaniline) needed not to purified as it was 98% pure (checked by TLC and ^{1}H NMR).

^{1}H NMR (300 MHz, $CDCl_3$) δ = 7.28 (d, 1H, ArH), 6.92 (d, 1H, Ar-H), 6.48-6.44 (dd, 1H, Ar-H), 3.7 (s, 2H, -NH_2)

5.2.9 Synthesis of 1,2-Dibromo-4-iodobenzene (29):

3,4-dibromoaniline (5 g, 18.8 mmols) was dissolved in sulphuric acid (3.14 mL concentrated in ~15 mL water). It was not completely dissolved, so added little THF, then cooled the solution to 0-5^{o}C. To this cooled

solution was added cooled aqueous solution of $NaNO_2$ (1.68 g in ~10 mL). Bubbles started coming. The mixture was stirred for some time and then added KI solution (4 g in ~15 mL water) drop-wise. Reddish-yellow fumes started to evolve. Then stirred the mixture for few hours and then finally heated at ~55^oC for 3 h. Stand the mixture overnight and added aqueous $Na_2S_2O_7$ solution in water to liberate excess iodide. The solution turned pale yellow, stirred for some time. The mixture was then extracted with ethyl acetate or diethyl ether. Orange layer was obtained which was dried over $MgSO_4$, filtered and solvent was removed on rotar at 35^oC. The solid obtained was purified on silica column using hexane as eluent to get 1,2-dibromo-4-iodobenzene (**29**) as greenish white solid.

^1H NMR (300 MHz, $CDCl_3$) δ = 7.87 (s, 1H, ArH), 7.37-7.40 (m, 1H, Ar-H), 7.23 (d, 1H, Ar-H).

5.2.10 Synthesis of (30):

1,2-dibromo-4-iodobenzene (3 g, 8.3 mmols) was dissolved in about 20 mL 1,2-dimethoxyethane and kept under nitrogen atmosphere. To it was added $Pd(PPh_3)4$ (0.41 g, 0.38 mmols) quickly and solution became reddish; stirred for 10 minutes. Then added boronic acid (1.06 g, 8.7 mmols) and 2M Na_2CO_3 to the reaction mixture. After a while solution became yellowish and it was refluxed (85^oC). The reaction was monitored by TLC and showed completion after 14 h, stopped heating and stirring and allowed to cool at room temperature. The mixture was then extracted with CH_2Cl_2/water, organic layer dried over $MgSO_4$ and filtered. The organic solvent was removed on rotar to get yellowish red viscous liquid crude. Purification of the crude on the silica column using hexane as an eluent gave colorless viscous liquid (**30**).

^{1}H NMR (300 MHz, $CDCl_3$) δ = 7.83 (s, 1H, ArH), 7.65 (d, 1H, Ar-H), 7.50-7.33 (m, 8H, Ar-H).

5.2.11 Synthesis of (31):

Compound **30** (2.2 g, 7.05 mmols), PPh_3 (0.27 g, 1.04 mmols), $PdCl_2(PPh_3)_2$ (0.1 g, 0.14 mmols), CuI (0.1 g, 0.56 mmols) and triethylamine (~50 mL) were taken in RBF and stirred and heated at ~40^{o}C for about 45 minutes under nitrogen atmosphere; immediately yellowish suspension was formed. Then added 2-methyl-3-butyn-2-ol quickly to it and heating and stiring continued for 2 days. After work-up brown solid crude was obtained, which was used without purification for further reaction.

5.2.12 Synthesis of (32):

Crude compound **31** (4 g, 12.57 mmols) was dissolved in 1,4-dioxane solvent and added crushed KOH pellets (1.7 g, 30.16 mmols) to it. The mixture was stirred and heated at 75-80^{o}C for ~6 h. Reaction was monitored by TLC and showed completion. After work-up viscous red liquid was obtained. The crude was purified by column chromatography (silica gel) using hexane as an eluent. Collected the first fraction (**32**) which was highly viscous greenish oil and on keeping several days in a refrigerator got solidified.

^{1}H NMR (300 MHz, $CDCl_3$) δ = 7.65 (s, 1H, ArH), 7.58-7.22 (m, 7H, Ar-H), 3.28 (d, 2H, ≡C-H).

Synthesis of the amphiphilic surfactant monomer:

5.2.13 1,2-Diiodo-4,5-dimethoxybenzene (33):

Iodine crystals 39.67 g (156.31 mmols) and dry CH_2Cl_2 (50 mL) were taken in round bottom flask, sonicated and stirred for few minutes. 16.92 g HgO (red) powder (78.15 mmols) was added slowly for about 20 minutes. Then added 1,2-dimethoxybenzene 9.0 g (65.13 mmols) from side arm slowly. The reaction was stirred at room temperature for 20 hours. Filtered the solution and discarded the scarlet red precipitate formed. The filtrate was washed with 5% sodium thiosulphate, saturated NaCl and then extracted with ethyl acetate (EA). The organic layer was dried over $MgSO_4$, filtered; the ethyl acetate was removed on rotar to get the solid crude. Recrystallization of the crude from ethyl acetate gave white product.

^{1}H NMR: (300 MHz, $CDCl_3$): δ= (300 MHz, $CDCl_3$): δ=7.23 (s, 2H; ArH), 3.83 (s, 6H; OCH_3).

5.2.14 4,5-Diiodo-1,2-benzenediol (34):

1,2-diiodo-4,5-dimethoxybenzene (7 g, 17.94 mmols) was dissolved in about 40 mL CH_2Cl_2 and maintained the reaction temperature at -15^{o}C. Then 12 mL of BBr_3 solution (1M in CH_2Cl_2) was added slowly by syringe under N_2 atmosphere while stirring. The reaction was monitored by TLC. Reaction completed after 6 hours. The reaction mixture was extracted with CH_2Cl_2 and water, saturated NaCl, organic layer separated and dried over $MgSO_4$. The organic layer was filtered and solvent evaporated on rotar to get the solid crude. The compound was purified on column with EA/Hexane (3:7) as an eluent, to get pink white solid.

^{1}H NMR (300 MHz, $CDCl_3$): δ=7.34 (s, 2H; ArH), 5.45 (s, 2H, –OH).

5.2.15 11-2-[(11-Hydroxyundecyl)oxy]-4,5-diiodophenoxy-1-undecanol (35):

3 g (8.2 mmols) of compound **34** was dissolved in little DMF and to it was added 2.8 g (20.7 mmols) K_2CO_3. The mixture was stirred and heated at 60-70^oC, on which solution was turned reddish after about 45 minutes and then added 4.16 g (16.5 mmols) of 11-bromo-1-undecanol to the reaction mixture. Heating continued for about three hours under N_2 atmosphere. Then the reaction mixture was poured into the water, acidified by dilute HCl, extracted with EA/water and washed two times with saturated NaCl. The organic layer was separated and dried over $MgSO_4$. After evaporating EA on rotar, pink solid obtained. Decanting several times with EA, yellowish solid product was obtained.

^{1}H NMR: (300 MHz, $CDCl_3$): δ=7.24 (s, 2H; ArH), 3.92 (t, 4H, –OCH_2), 3.63 (t, 4H, –$\underline{CH_2}$OH), 1.78-1.29 ppm (m, 36H, –CH_2).

5.2.16 4-2-(3-Hydroxy-3-methyl-1-butynyl)-4,5-di[(11-hydroxyundecyl)oxy]phenyl-2-methyl-3-butyn-2-ol (36):

Compound **35** (3 g, 4.2 mmols) was dissolved in three neck round bottom flask containing about 50 mL triethylamine by sonication. Then added $PdCl_2(PPh_3)_2$ (0.06 g, 0.03 mmols), PPh_3 (0.16 g, 0.6 mmols) and CuI (0.02, 0.34 mmols) to it. The mixture was stirred and heated at about 70^oC for 45 minutes. Then was added 2-methyl-3-butyn-2-ol (0.86 g, 10.02 mmols) to it from the side arm. Yellowish gel was formed. Heating and stirring continued for one day. Reaction was monitored by TLC. Filtered the reaction mixture and triethylamine was removed on rotar; extracted with EA and water, washed with saturated NaCl. Organic layer was separated and dried over $MgSO_4$, filtered and EA was removed on rotar to get the solid crude. Recrystallization of the crude from EA/Hexane gave fine yellowish crystals.

^{1}H NMR: (300 MHz, CDCl3): δ=6.86 (s, 2H; ArH), 3.97 (t, 4H, –OCH_2), 3.63 (t, 4H, –$\underline{CH_2}OH$), 2.81 (s, 2H, $\underline{HO}$–$C(CH_3)_2$), 1.62 (s, 12H, –CH_3), 1.80-1.28 ppm (m, 36H, –CH_2).

5.2.17 11-4,5-Di(1-ethynyl)-2-[(11-hydroxyundecyl)oxy]phenoxy-1-undecanol (37):

Compound **36** (1.2 g, 1.95 mmols) was dissolved in a little amount of 1,4-dioxane. KOH pellets (0.52 g, 9.3 mmols) were crushed and added to it. Mixture was stirred and heated at about 80-90^{o}C for about four hours. Dean-Stark apparatus was attached to it to collect the acetone formed during the reaction. Then the reaction mixture was poured into water and was acidified with dilute HCl, extracted with EA, water and washed by saturated NaCl. The organic layer was separated, dried over $MgSO_4$, filtered and EA was removed on rotar. Recrystallization from EA/Hexane gave **37** as off-white solid.

^{1}H NMR: 6.92 (s, 2H, ArH), 3.98 (t, 4H, –OCH_2), 3.63 (t, 4H, –$\underline{CH_2}OH$), 3.22 (s, 2H, ≡C–H), 1.81-1.26 ppm (m, 36H, –CH_2).

IR (KBr): 3360, 3280, 2920, 2850, 2107, 1705, 1595, 1506, 1460, 1388, 1340, 1260, 1205, 1093, 1055, 850, 720 and 610 cm^{-1}.

5.2.18 Polymerization of surfactant monomer (37):

Benzene solution of surfactant monomer (0.3 g, 0.6 mmols) was taken in thick-walled screw cap glass tube which was capped in the glove box under nitrogen atmosphere prior to heating at 140^{o}C for one day. After cooling, polymer was collected by filtration and washed with diethyl ether. The polymer was dried *in vacuo* to yield 0.22 g of insoluble red-brown solid.

IR (KBr): 3425, 2913, 2845, 1625, 1505, 1457, 1378, 1250, 1050, 847 and 719 cm^{-1}.

5.2.19 Evaporation Induced Self Assembly (EISA) to form the hybrid nanocomposite:

Precursor solutions were synthesized from tetraethyl orthosilicate (TEOS, $Si(OC_2H_5)_4$), surfactant monomer, and HCl catalyst prepared in ethanol/water solvent. The final reactant mole ratio for nanocomposites prepared from surfactant monomer was 1 TEOS: 30 ethanol: 5 H_2O: 0.1 HCl: 0.5 monomer. In a typical preparation, TEOS, ethanol, water and dilute HCl were stirred and heated at 35^oC for half an hour. To this solution was added the surfactant monomer in ethanol and stirred for three hours. Films were prepared on quartz by evaporative spin-coating (1,500 r.p.m.), or dip-coating (at a rate of 30 cm min^{-1}). During deposition, preferential evaporation of THF concentrates the depositing film in water and nonvolatile silica and surfactant monomer. The progressively increasing surfactant concentration drives self-assembly of surfactant monomer/silica micelles and their further organization into ordered liquid crystalline mesophases. These films were vacuum-dried for overnight and kept immersed in benzene in thick-walled screw cap glass tubes which were capped in the glove box under nitrogen atmosphere prior to heating at 140^oC for one day.

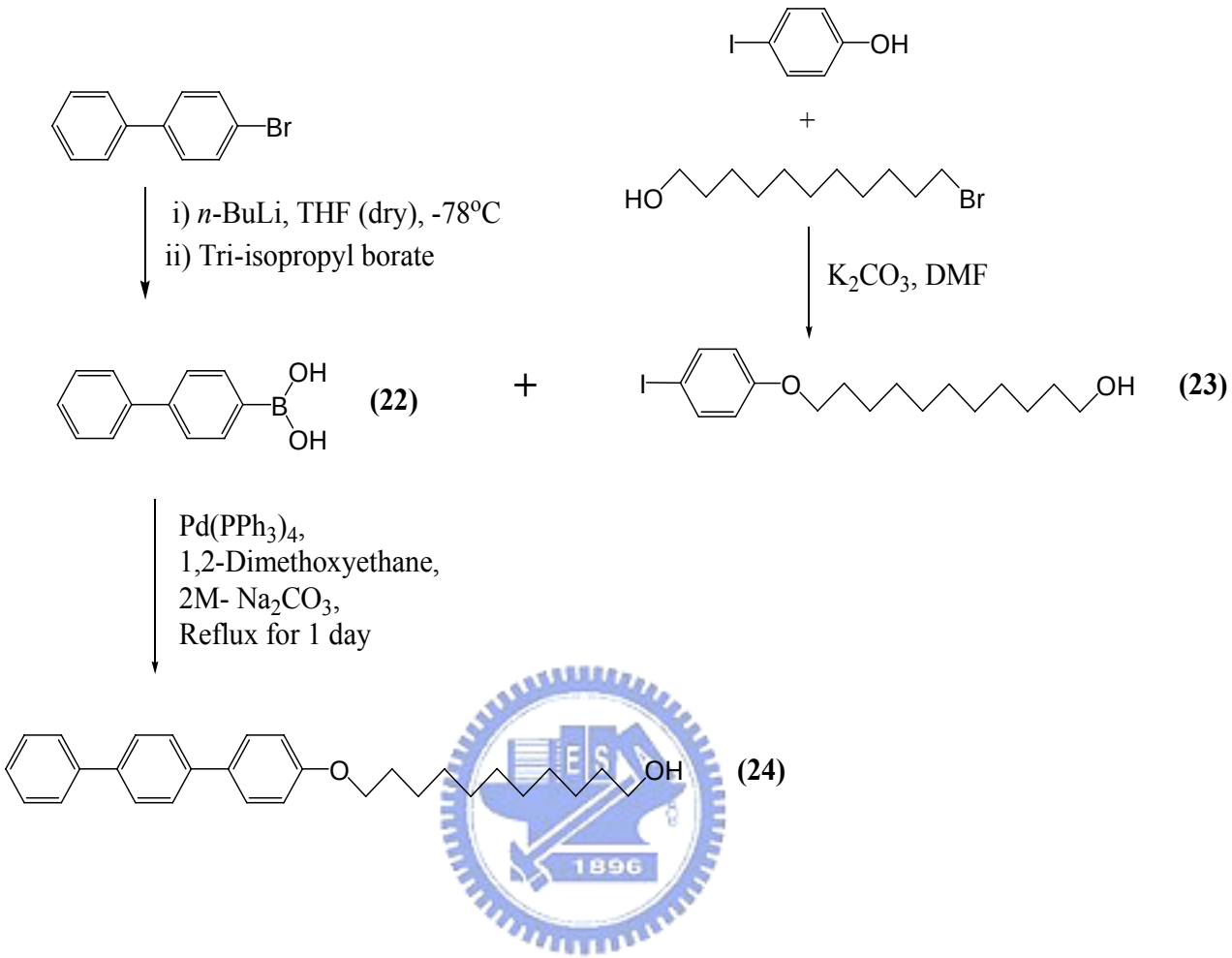

Scheme 5.1 Synthesis of PPP-C11.

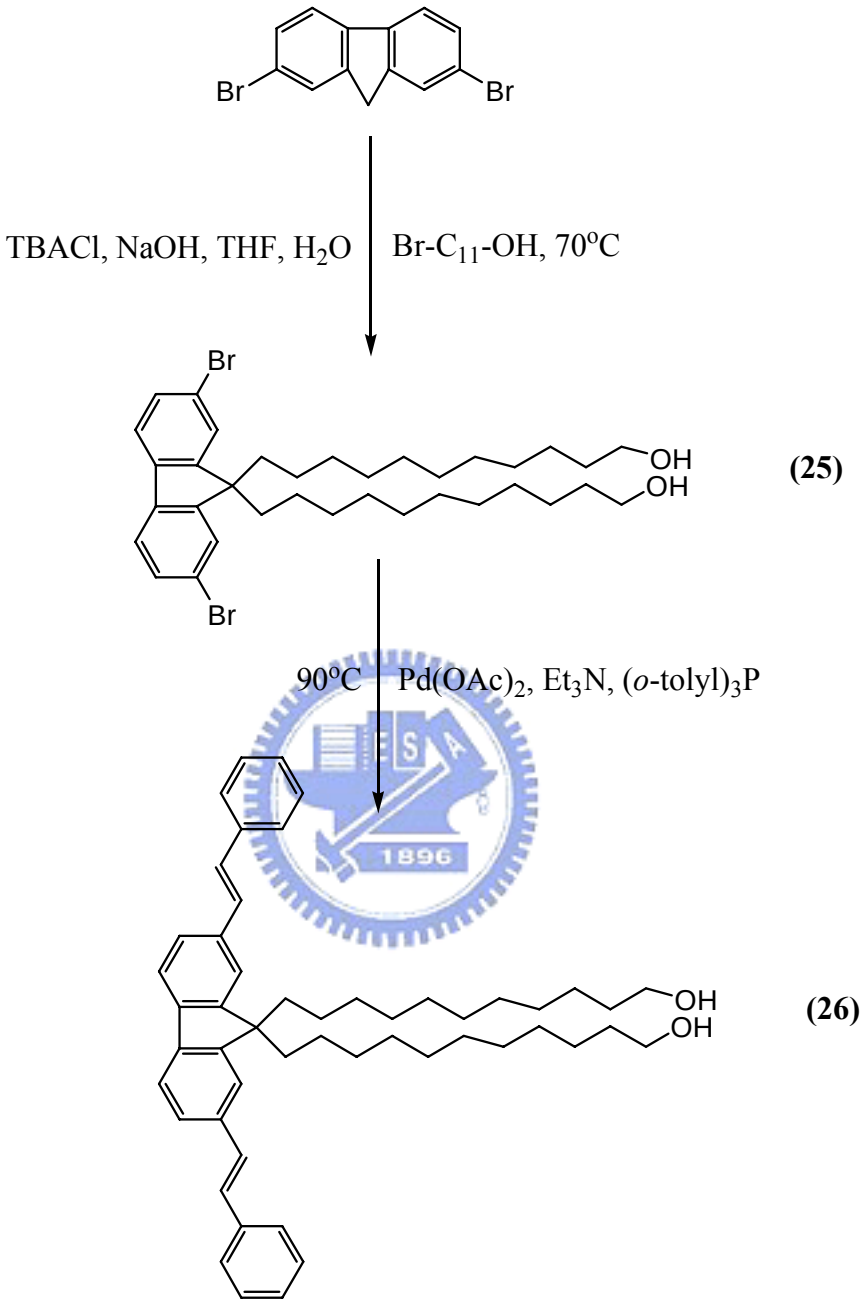

Scheme 5.2 Synthesis of FL-Stilbene-$(C11)_2$.

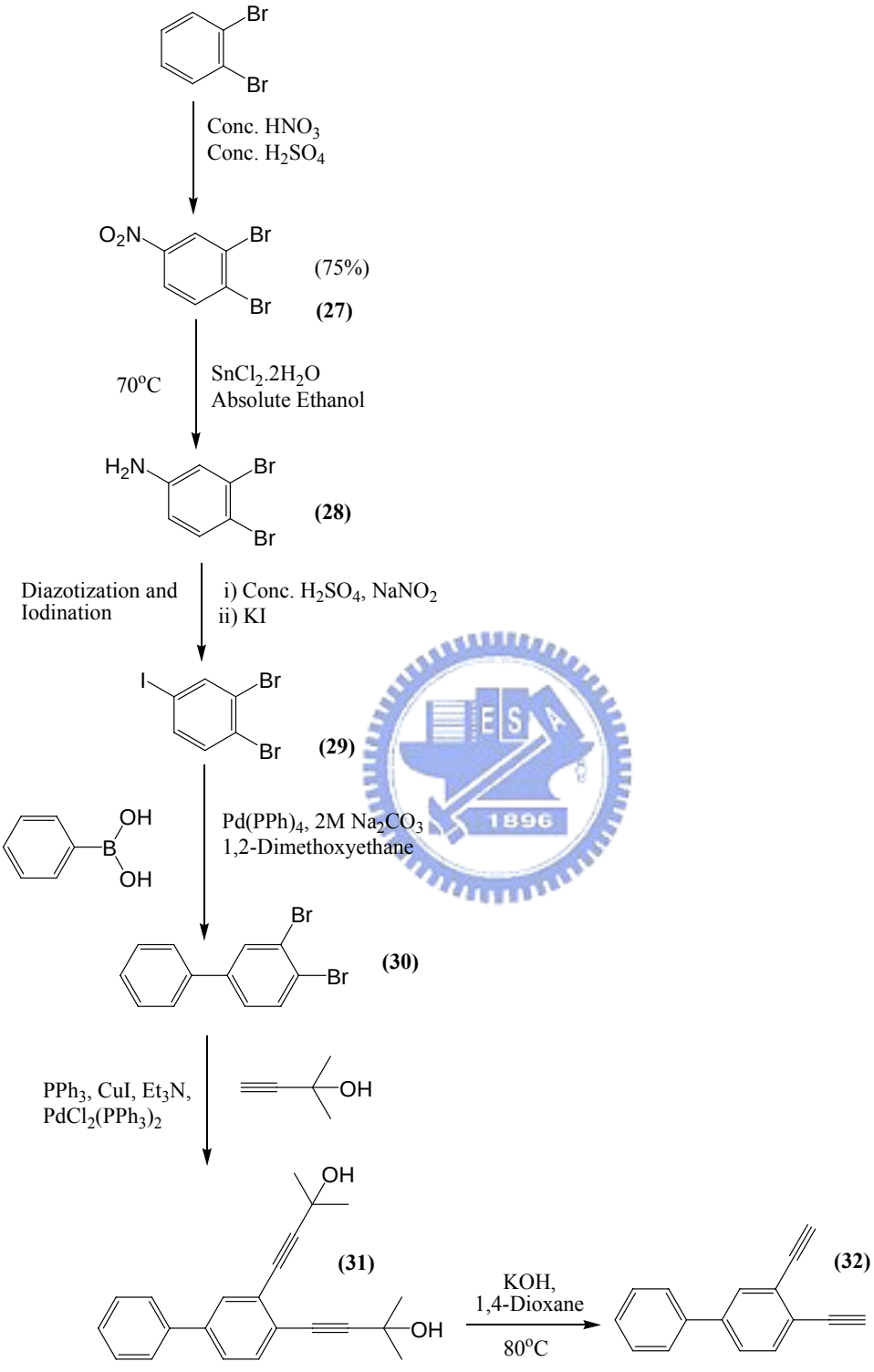

Scheme 5.3 Synthesis of Bergman Monomer (32)

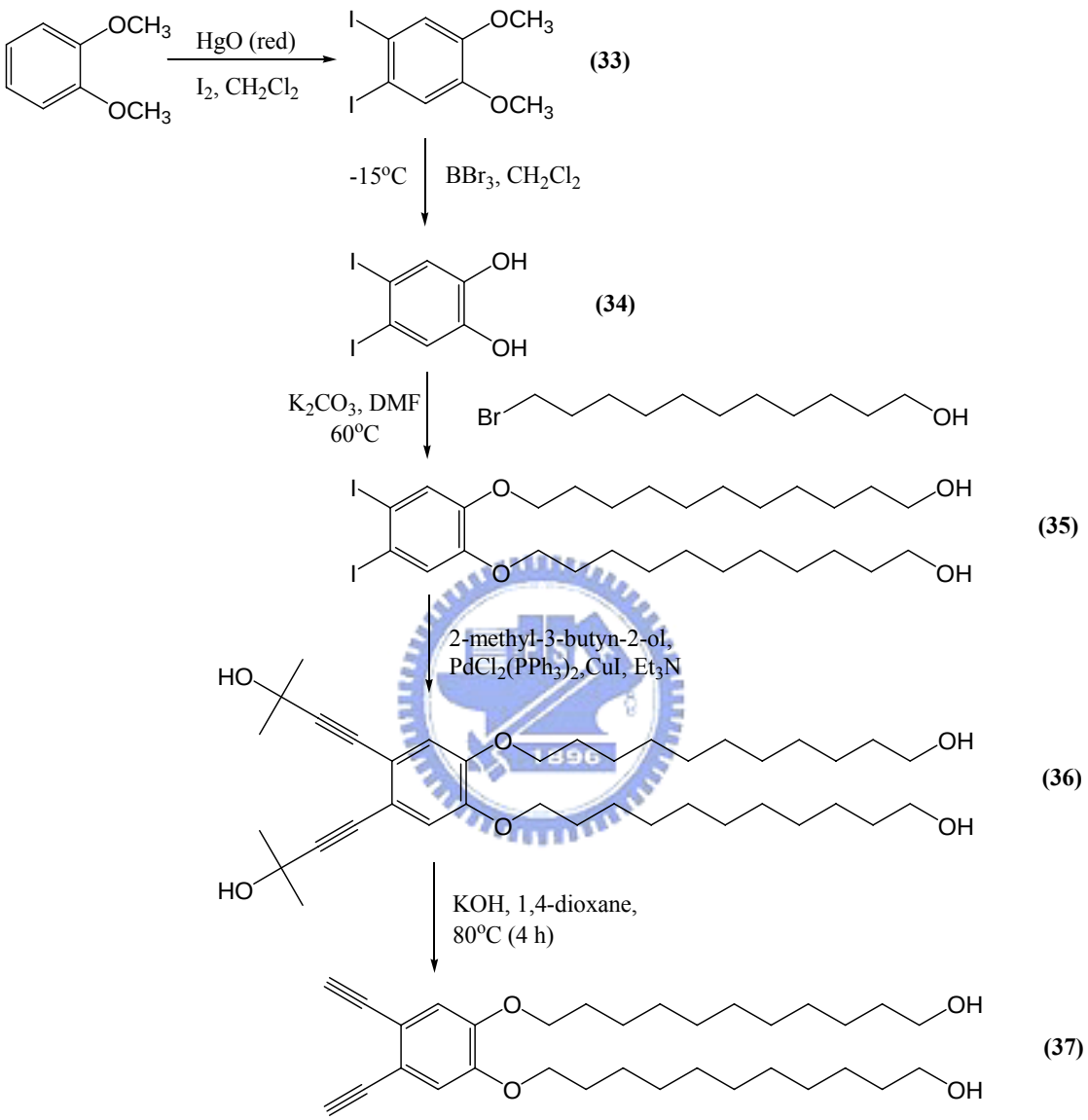

Scheme 5.4 Synthesis of polymerizable amphiphilic surfactant monomer

Chapter 6
Results and Discussion

6.1 Synthesis and Characterization of Organic-Inorganic Functional Hybrid Nanocomposites formed by Self-Assembly

We designed and synthesized chromophoric surfactant amphiphiles PPP-C11 and FL-Stilbene-$(C11)_2$ (Scheme 6.1) and carried out their co-assembly with silica precursor (TEOS) to give the organic-inorganic functional hybrid nanocomposites, with remarkable fluorescence enhancement properties and these were characterized with different techniques such as SEM, TEM, UV-Visible absorbance and photoluminescence, XRD analysis, etc. (see Experimental Part of this section for the procedural details). ^{1}H NMR spectra for PPP-C11 and FL-Stilbene-$(C11)_2$ are shown in the following Figures 6.1 and 6.2, respectively.

Here, we have exploited the Evaporation Induced Self-Assembly (EISA) approach to make mesostructured functional hybrid nanocomposite films keeping in view its potential use in electroluminescence devices where fluorescence quenching in solid state is the thorniest problem.

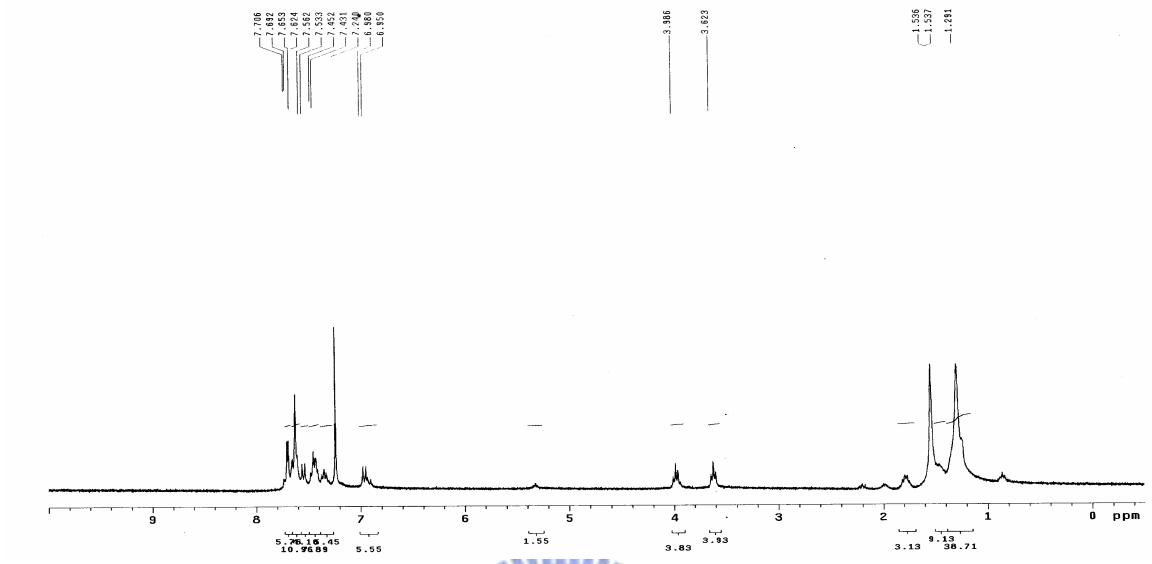

Figure 6.1 ^{1}H NMR spectrum of PPP-C11

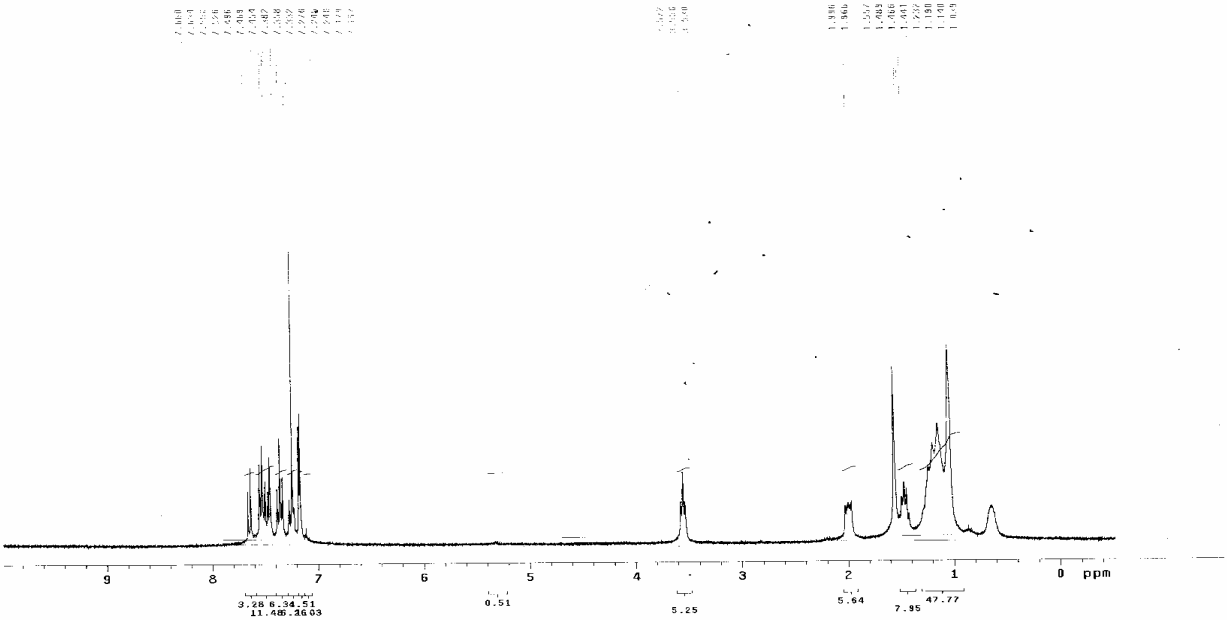

Figure 6.2 ^{1}H NMR spectrum of FL-Stilbene-$(C11)_2$

Self-assembly can organize hydrophilic, inorganic and hydrophobic, organic precursors into ordered nanostructures. It is well known that the organic nanoparticles have special properties which lie between the properties of molecules and those of bulk materials. Aggregation induced emission (AIE) enhancement has been observed for diverse range of conjugated organic nanoparticles. The idea behind the formation of these hybrid nanocomposites was to form the core or clusters of the chromophoric groups as nano-packets through self-assembly that could enhance the photoluminescence (PL) of the nanocomposite films prepared; a seemingly ideal solution for the solid-state quenching of fluorescence.

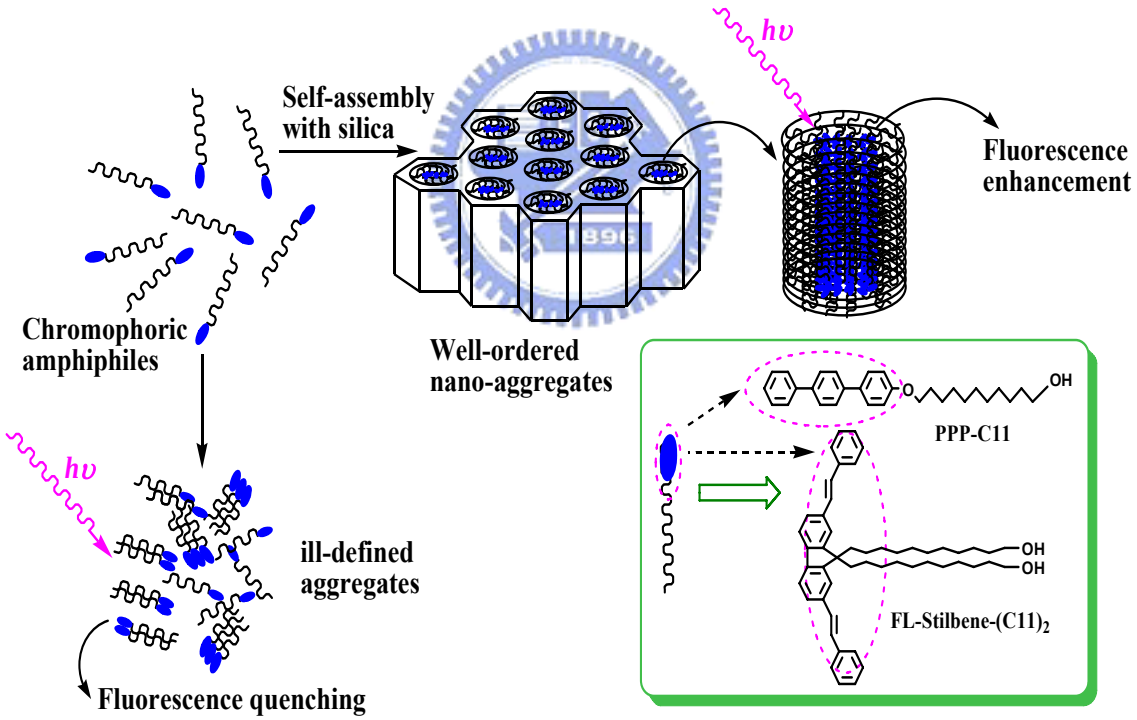

Scheme 6.1 Formation of chromophore bearing amphiphile/silica self-assembled hybrid nanocomposite and chemical structures of the chromophore amphiphiles used.

And, indeed, we observed an enhancement of photoluminescence intensity and quantum efficiency depending on orientation and packing of chromophoric groups at the tail end. The chromophore amphiphiles act as photoactive molecules as well as structure directing agents. Scheme 6.1 shows the schematic formation of these nanocomposites with well ordered array of the chromophores within the silica pores, enhancing the fluorescence.

6.1.1 Scanning Electron Microscopy (SEM):

Parts a and b, in Figure 6.3, are scanning electron microscopy (SEM) images of the nanocomposites formed. Figure 6.3-a, shows the formation of nanosheets of somewhat rectangular shape and few nanometers in thickness, of PPP-C11 nanocomposite. Uniform nanorods of about 75 nm in diameters and lengths measuring below 1 μm were formed for FL-Stilbene-$(C11)_2$ nanocomposite (Figure 6.3-b). These specimens were scratched gently from the dip-coated quartz substrates for the imaging.

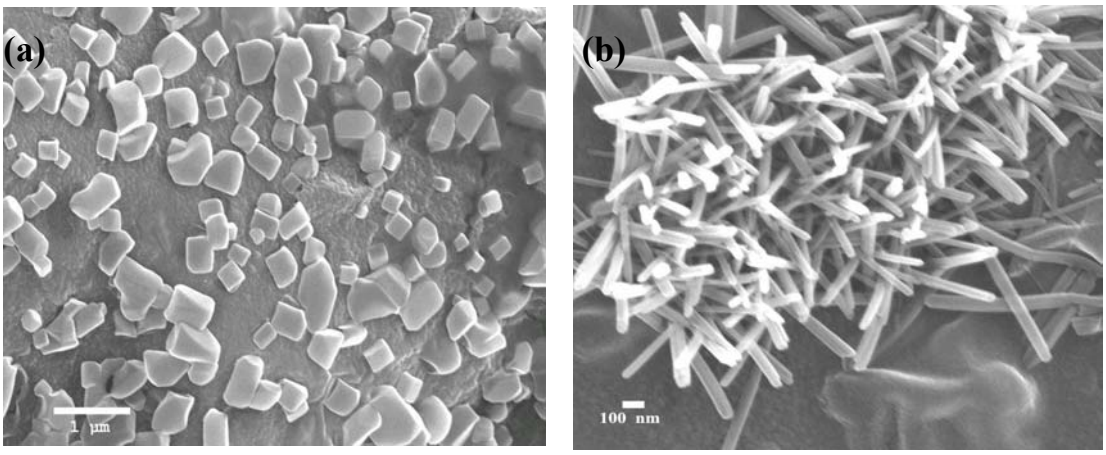

Figure 6.3 Scanning electron microscopy images of chromophore amphiphile/silica self-assembled nanocomposites formed from a) PPP-C11 and b) FL-Stilbene-$(C11)_2$.

6.1.2 X-ray Diffraction:

X-ray diffraction (XRD) analysis of the nanocomposite thin films showed peaks characteristics of periodic mesoscopic silicate structure. XRD revealed a single peak around 2θ = 1.53 and 1.57°, indicating periodic short range structural order with *d*-spacing for (100) diffraction peak of 57.9 and 56.2 Å for nanocomposite films of PPP-C11 and FL-Stilbene-$(C11)_2$, respectively (see Figure 6.4). The presence of higher order Bragg peaks around 2θ = 3 and 4.5° in Figure 6.4-a indicates that PPP-C11 nanocomposite posseses high degree of long-range structural order also.

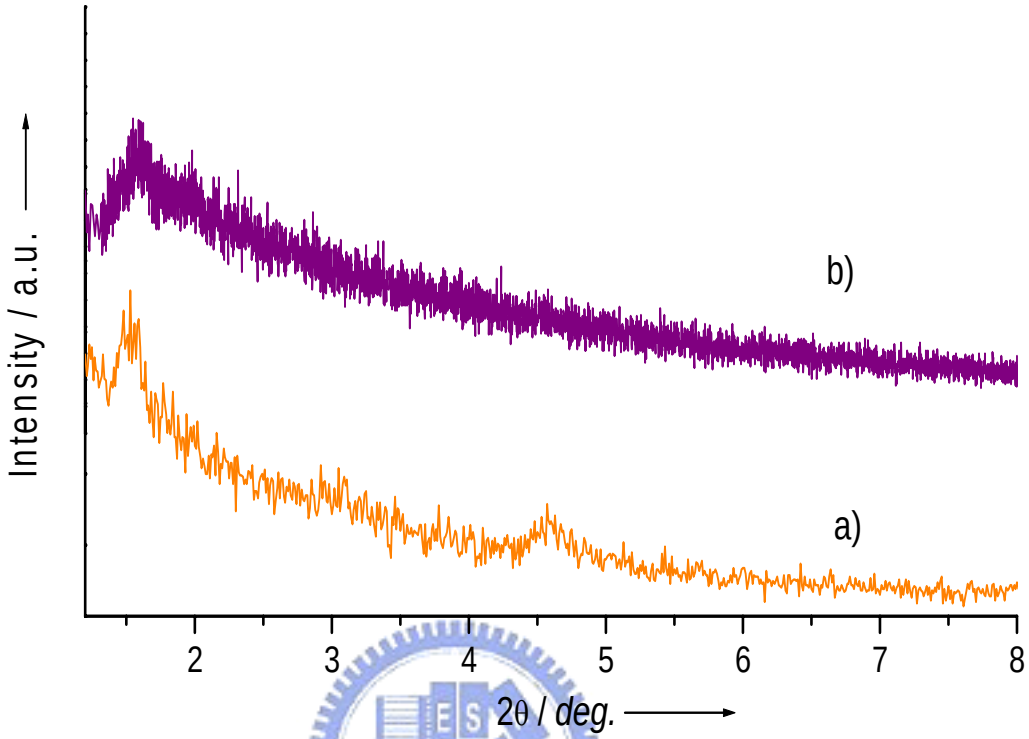

Figure 6.4 XRD of mesostructured chromophore amphiphile/silica self-assembled nanocomposites formed from a) PPP-C11 and b) FL-Stilbene-$(C11)_2$.

6.1.3 Transmission Electron Microscopy (TEM):

Transmission electron microscopy (TEM) images obtained from nanocomposites revealed that the composite with FL-Stilbene-$(C11)_2$ displayed a uniform mesostructure, but with no apparent long-range ordering (Figure 6.5-b), whereas nanocomposite produced using PPP-C11 displayed a highly uniform periodic mesostructure (Figure 6.5-a).

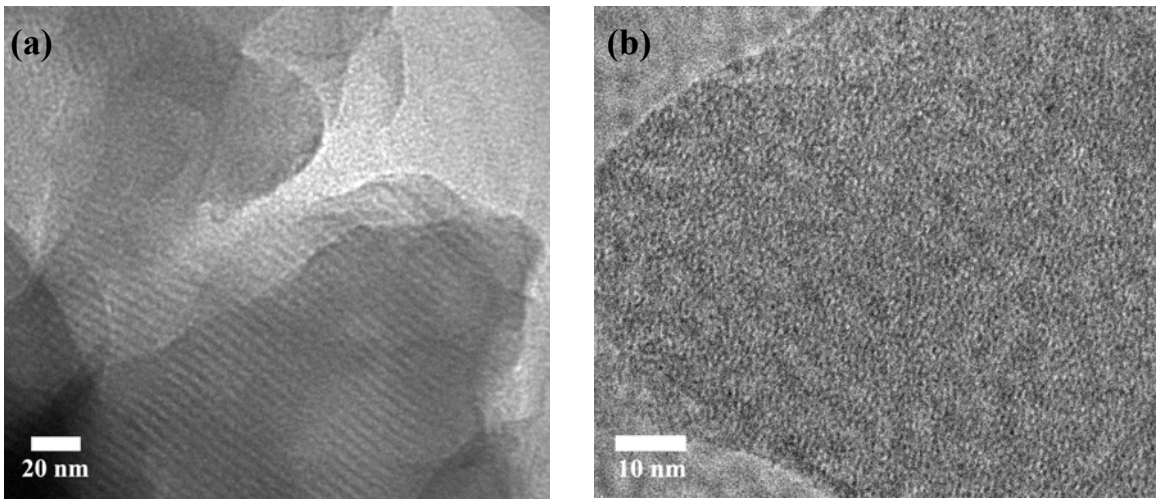

Figure 6.5 Transmission electron micrographs (TEM) of chromophore amphiphile/silica self-assembled nanocomposites formed from a) PPP-C11 and b) FL-Stilbene-$(C11)_2$.

This difference is attributed due to the size and orientation of the chromopore groups employed at the tail ends and length and size of surfactant in nanocomposites as these factors affect the topochemicity of amphiphile surfactants and consequently packing of the chromophores within the channels. Bulkier the group more is the steric hindrance; hence loose packing of the chromophores. We propose that increasing the surfactant tail area, consequently that of chromophore, might reduce value of the surfactant packing parameter (g) and thus affect the mesostructure formation. An apparent decrease in the d-spacing in comparison to the XRD results may be due to the shrinkage of the samples in the TEM chamber. Although a future detailed structural study is needed, the present results show that these precursors have the ability to form mesophases through self-assembly.

6.1.4 UV-Visible Absorbance and Photoluminescence Spectroscopy:

UV-Visible absorption and PL spectra for PPP-C11 nanocomposite are shown in Figure 6.6-a and b, respectively. PPP-C11 is an amphiphile bearing terphenyl (oligomer of polyphenylene) chromophore as a hydrophobic part and a single alkyl chain with hydroxyl head group as hydrophilic part. Absorbance of PPP-C11 surfactant chromophore solution in THF is observed at 292 nm of wavelength. But when thin film is formed of PPP-C11 surfactant chromophore, its absorbance is decreased with a blue shift of about 17 nm. Nanocomposite thin film also showed maximum peak (λ_{max}) around 275 nm. Photoluminescence of PPP-C11 surfactant chromophore solution in THF showed a single band with maximum peak at 365 nm. In solid state it showed much decrease in the PL with a maximum peak at 390 nm and two weak shoulders were observed at longer wavelength. There was a red shift of 25 nm compared to its solution PL. However, in its nanocomposite, we observed strong emission enhancement in UV-blue region with a maximum peak at 390 nm and two well pronounced shoulders at 406 and 435 nm, indicative of an evident vibrational structure. This fluorescence change, with about fourteen fold increase in the intensity, is quite unusual considering that the fluorescence efficiency of organic chromophores generally decreases in the solid state, although they show high fluorescence efficiency in solution.

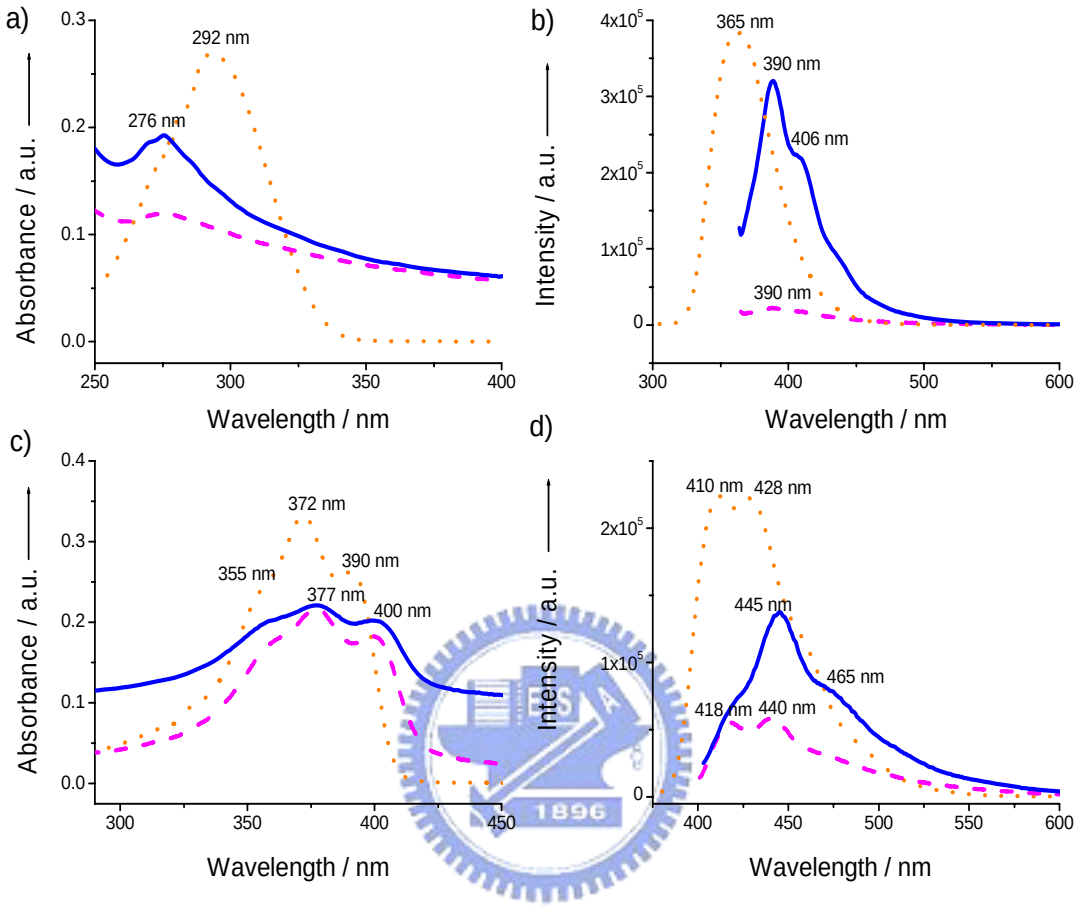

Figure 6.6 UV-Visible absorption spectra for THF solution (dotted lines), chromophore (dashed lines) and nanocomposite (solid lines) films of a) PPP-C11 and c) FL-Stilbene-$(C11)_2$. Photoluminescence spectra for THF solution (dotted lines), chromophore (dashed lines) and nanocomposite (solid lines) films of b) PPP-C11 and d) FL-Stilbene-$(C11)_2$. (PL intensities of solutions were normalized for comparison.)

The decrease in fluorescence efficiency in the solid state is quite general and is mainly attributed to the intermolecular vibronic interactions which induce the nonradiative deactivation process, that is, fluorescence quenching, such

as excitonic coupling, excimer formations, and excitation energy migration to the impurity traps. However, the emission enhancement we observed in the nanocomposite films is due to the well ordered arrangement of the chromophore groups at nanoscale. The other chromophore amphiphile studied, FL-Stilbene-$(C11)_2$, is having bulky chromophoric group, as the hydrophobic tail end, containing fluorene and stilbene moieties and two long alkyl chains with hydroxyl head groups as hydrophilic part. Tetrahydrofuran solution of FL-Stilbene-$(C11)_2$ showed absorbance at 372 nm with two shoulders at 355 and 390 nm (see Figure 6.6-c). Its absorbance decreased in chromophore and nanocomposite films with a red shift of five nm for λ_{max}, measuring at 377 nm and shoulder peaks were also shifted to longer wavelengths by about five and ten nanometer, correspondingly. FL-Stilbene-$(C11)_2$ in THF solution showed bright blue fluorescence with two clearly resolved vibronic features peaked at 410 and 428 nm in PL spectrum (see Figure 6.6-d). In pure chromophore amphiphile film, its PL intensity quenched with red-shifted emission still showing the well resolved vibronic features at 418 and 440 nm and a broad shoulder at longer wavelength. However, when the nanocomposite film of FL-Stilbene-$(C11)_2$ was formed by EISA, its emission intensity was enhanced more than two folds compared to its chromophore amphiphile film alone and λ_{max} was observed at 445 nm, with shoulders being at around 428 and 465 nm. Increase in absorbance in nanocomposite indicates increase in effective conjugation length of chromophores and consequently enhancement in the fluorescence is observed. The 'controlled' aggregations of the chromophoric groups within the hydrophobic core of the nanocomposite minimize the larger crystals formation and thus enhance the fluorescence. The nanopackets in hybrid composites could provide controlled concentration of active dots or

chromophores, better defined systems, and avoid coalescence into larger ill-defined aggregates. Similar enhancement was observed for C540A residing in the organic, hydrophobic regions of the nanocomposite. Though in most cases for fluorescent molecules in molecular sieves Forster quenching is observed, the induced fluorescence enhancement in this case is attributed due to the well ordered nanopackets of 'controlled' chromophore aggregations formed in the self-assembled nanocomposites, and is evident from above results. The intensity increase may be due to an increased quantum efficiency of chromophore nanoaggregates within silica. Such fluorescence enhancement was also observed for the well-packed chains and aggregates in conjugated polymers and for fullerene aggregates in organic-inorganic nanocomposites. The mode of interactions amongst the chromophore amphiphile molecules in the functional hybrid nanocomposites is a topic of vast research interest and will get due attention in near future.

6.2 Bergman Cyclopolymerization of Polymerizable Amphiphilic Surfactant Monomer within the Channels of the Functional Hybrid Nanocomposites formed by co-assembly of monomer and silica.

The use of polymerizable surfactants as both structure-directing agents and monomers in various evaporation-driven self-assembly schemes represents a general, efficient route to the formation of robust and functional nanocomposites. We designed and synthesized Bergman monomer **32** and incorporated it in the pore channels of MCM-41, a mesoporous host material;

with the aim of carrying out Bergman cyclopolymierization within the hexagonal channels of MCM-41. However, monomer **32** met with the problem of leaching out of the host material, so effective incorporation and consequently, Bergman polymerization was not possible. To avoid such problem, we designed and synthesized another Bergman monomer **37**. In this research we utilize evaporation induced self-assembly (EISA) route to form mesostructured polynaphthalene/silica nanocomposites. One of the many approaches to form the polynaphthalenes (PN) is through Bergman cycloaromatization, a remarkable isomerization in which an en-diyne forms an arene 1,4-diradical. Here, we make use of this approach with materials synthesis view-point. Amphiphilic polymerizable surfactant monomer **37** was synthesized. It has two long alkyl chains with hydrophilic hydroxyl head groups at one end and the phenyl ring with two terminal acetylene groups *ortho* to each other at the tail end. These nanocomposites were characterized by different techniques such as SEM, TEM, UV-Visible absorbance and photoluminescence, XRD analysis, EDX, FT-IR, etc. (see Experimental Part of this section for the procedural details).

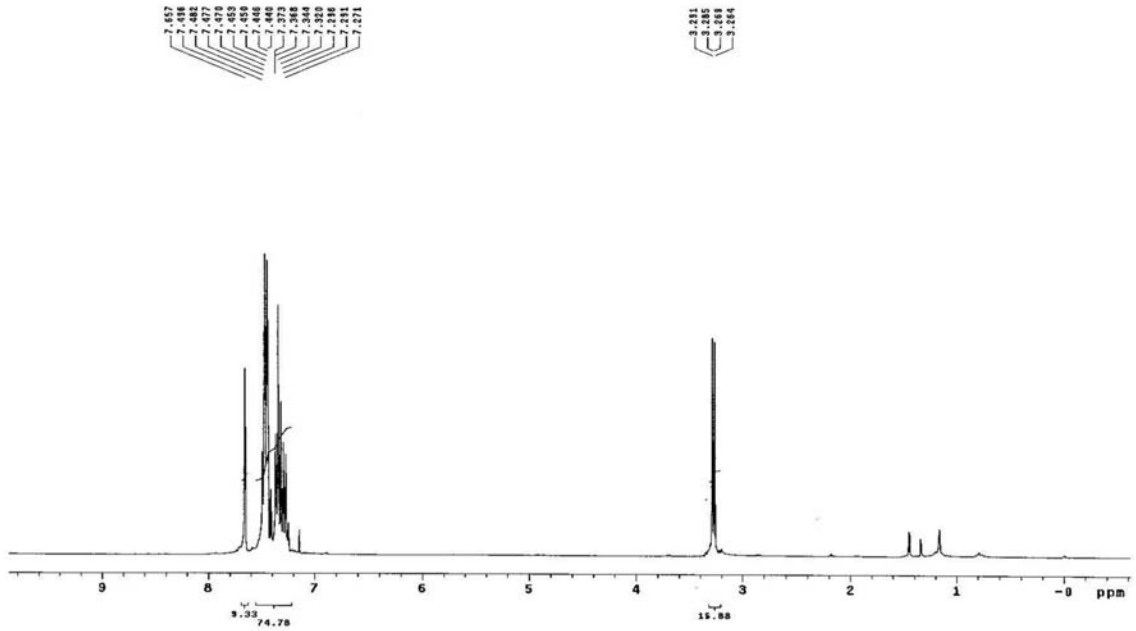

Figure 6.7 ^{1}H NMR spectrum of monomer 32

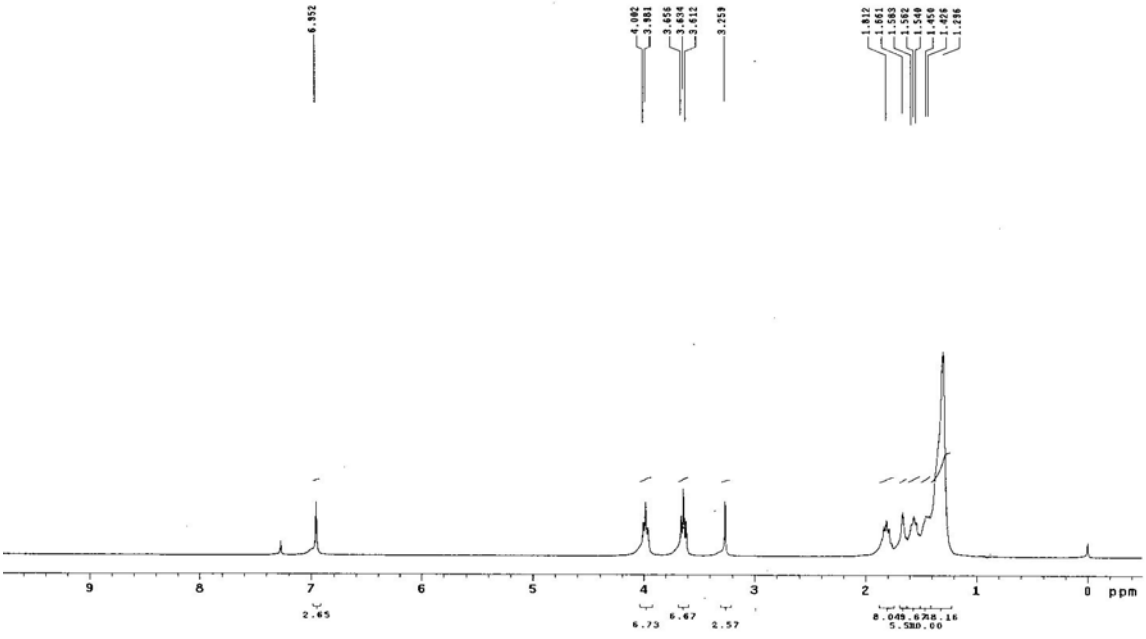

Figure 6.8 ^{1}H NMR spectrum of monomer 37

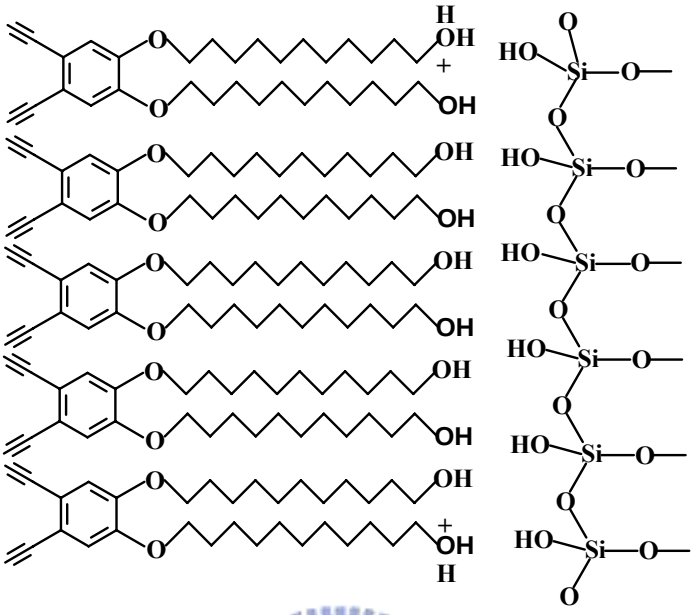

Scheme 6.2 Co-assembly of silica and polymerizable surfactant monomer.

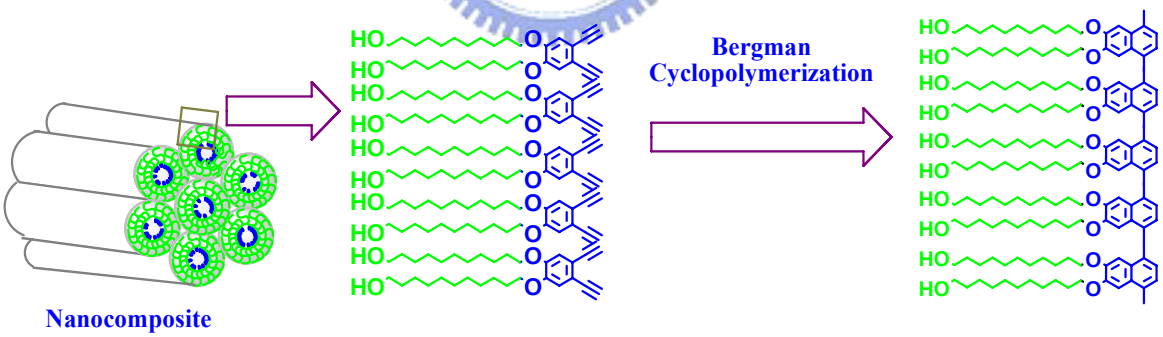

Scheme 6.3 Polymerization of the amphiphilic surfactant monomer within the hexagonal channels of silica.

6.2.1 Molar composition of the gel:

The final molar composition of the gel formed was 0.02 TEOS : 0.6 Ethanol : 0.10 H_2O : 0.002 HCl : 0.02 Monomer.

6.2.2 SEM images of the nanocomposite:

Scanning Electron Microscopy images were observed by the deposition of the gel mixture of the monomer/silica composite onto the carbon tape and are shown in the following Figure 6.9.

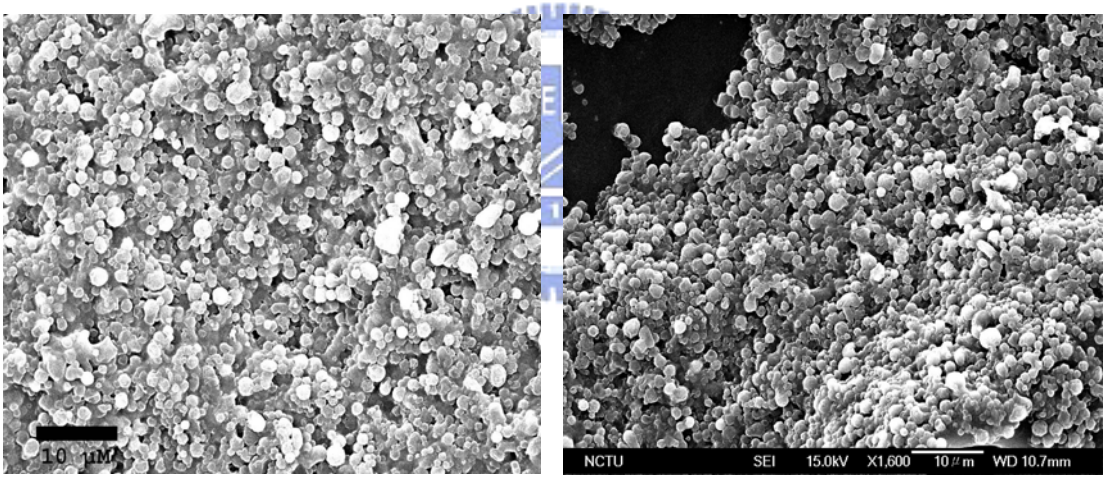

Figure 6.9 SEM images of amphiphilic surfactant monomer/silica nanocomposite formed.

6.2.3 X-Ray Diffraction (XRD):

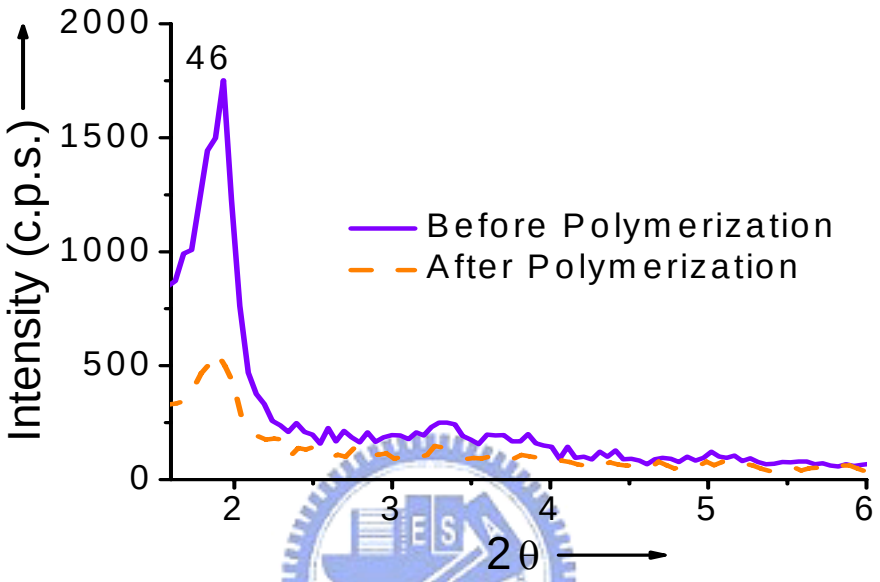

Figure 6.10 XRD of the amphiphilic surfactant monomer/silica nanocomposite formed (Before and after polymerization).

X-ray diffraction (XRD) patterns of the nanocomposites before (solid lines) and after (dashed lines) the Bergman cyclopolymerization are shown in Figure 6.10. The diffraction peak at around $2\theta = 1.90$ is attributed to the [100] orientation of the hexagonal mesophase. There was no change in the XRD peak position for the heat-treated (polymerized) sample, except a decrease in the intensity of the spectrum which indicates that the nanocomposite is intact even after heat-treatment (polymerization). The *d*-spacing value for the [100] peak from the XRD is found to be 46 Å.

6.2.4 Tunneling Electron Microscopy (TEM):

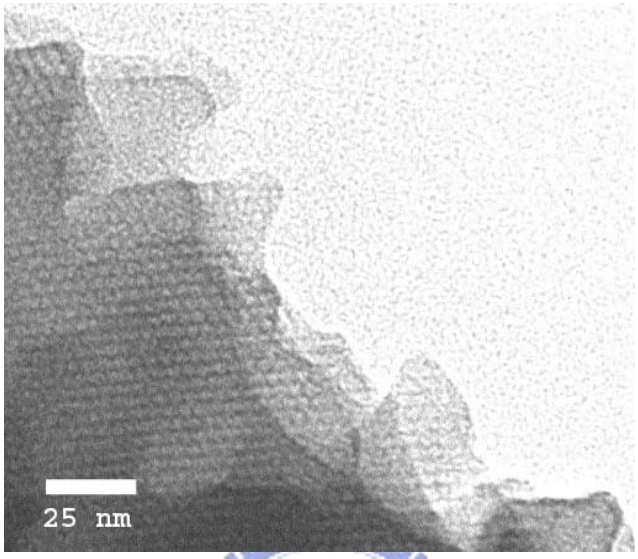

Figure 6.11 TEM image of the amphiphilic surfactant monomer/silica nanocomposite formed.

6.2.5 Energy Dispersive X-ray Spectroscopy (EDS):

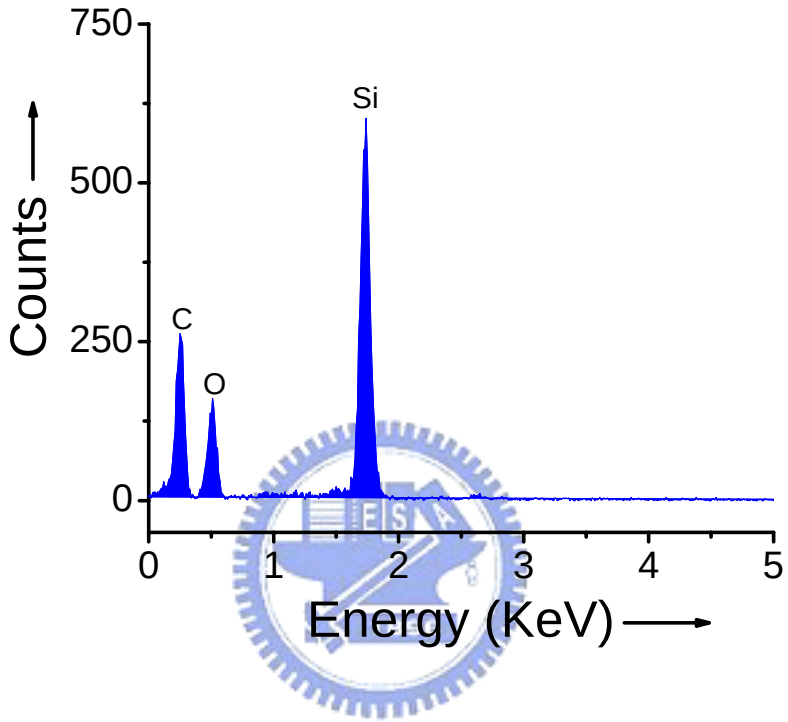

Figure 6.12 EDS of the amphiphilic surfactant monomer/silica nanocomposite formed.

Energy dispersive spectroscopy (EDS) elemental analysis identified carbon, silicon and oxygen as expected for the nanocomposite prepared and is shown in Figure 6.12.

6.2.6 Absorbance and Photoluminescence Spectra:

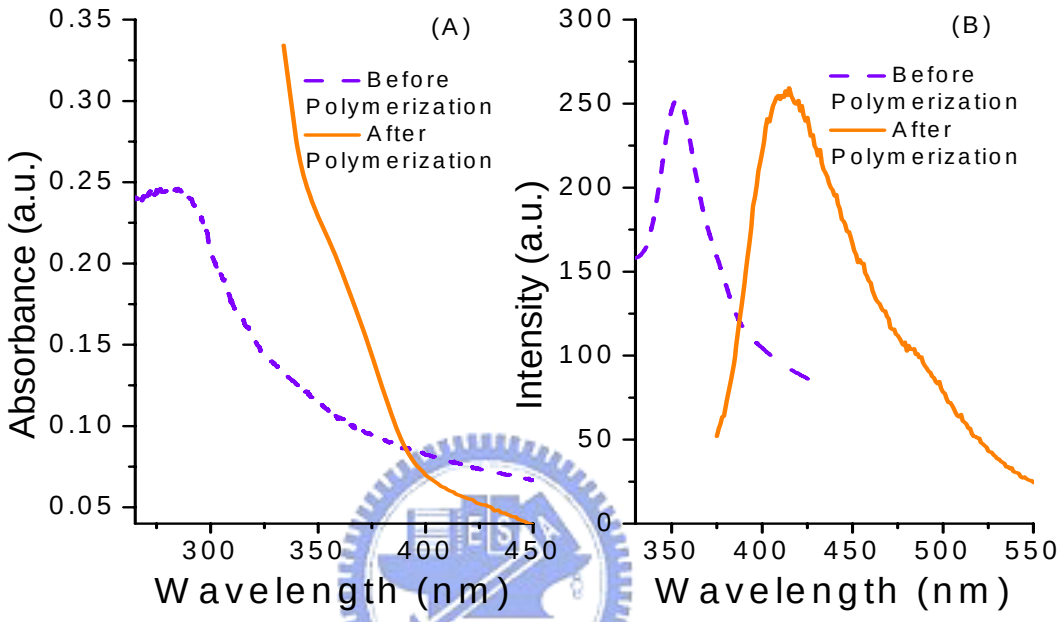

Figure 6.13 (A) UV-Visible absorbance and (B) Normalized PL spectra of the nanocomposites formed.

The topochemicity generated during the co-assembly favors the Bergman cyclopolymerization. Formation of polymer within the hexagonal channels of the nanocomposite was verified by UV-vis and photoluminescence spectroscopy. UV-vis spectroscopy has been used previously to relate the degree of polymerization and absorbance. Figure 6.13-A shows the absorption spectra of the nanocomposite before and after the polymerization. Monomer nanocomposite showed maximum absorbance at about 285 nm, whereas polymer nanocomposite showed absorbance between 345 to 390 nm

tailing up to 450 nm, indicating extensive conjugation of the polymer backbone. Direct molecular weight determination of such type of polymer/nanocomposite films is difficult. Monomer nanocomposite showed photoluminescence (PL) in uv-blue region with maximum peak at 353 nm (Figure 6.13-B). After polymerization, the photoluminescence was red-shifted with a maximum peak at 415 nm and a shoulder at around 483 nm.

6.2.7 Fourier Transform Infra-red (FTIR) Spectroscopy:

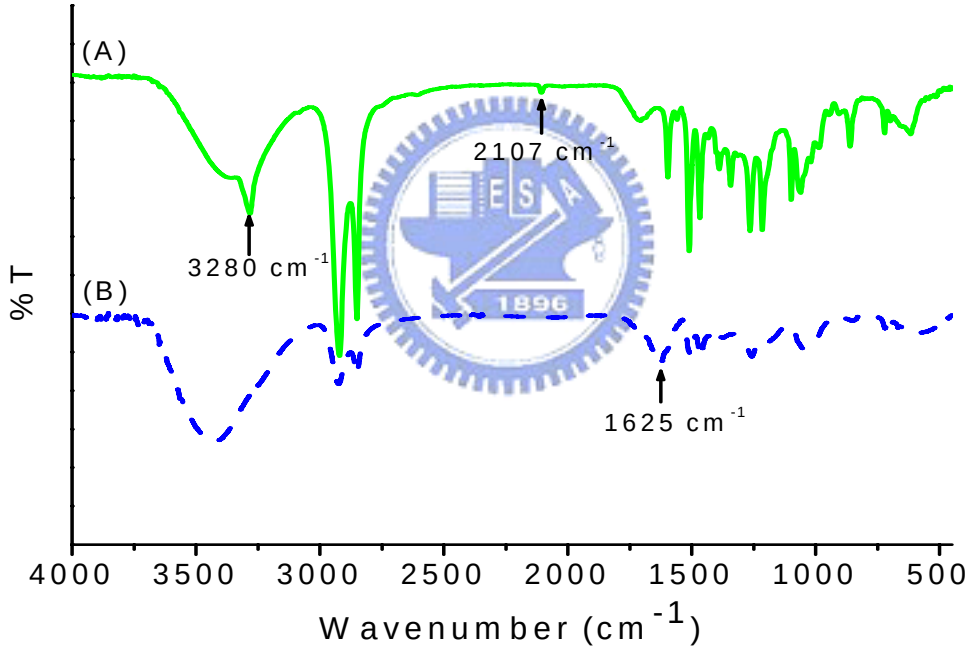

Figure 6.14 FTIR spectra of (A) monomer and (B) polymer formed by heating monomer in benzene

Bergman cyclopolymerization of the monomers with terminal acetylene groups, as in the present case, generally gives insoluble polymers, making

their characterization difficult. We carried out the polymerization of surfactant monomer dissolved in benzene as described in literature. Heating the monomer at about 140^{o}C for one day indeed afforded insoluble red brown solid. Monomer and polymer were characterized by infra-red (IR) spectra for comparison, as shown in Figure 6.14. The characteristic alkyne triple bond C-H and C≡C stretching bands at 3280 and 2107 cm^{-1}, respectively, present in the monomer disappeared after the polymerization. A new broad and strong band at 1625 cm^{-1}, due to C=C stretching was observed, indicating formation of polymer with extensive conjugation. The degree of polymerization in thin film and in bulk might be different as these are two different environments and should affect the extent of conjugation. There are controversies regarding the structure of the polymer formed by Bergman cyclization of monomer with terminal triple bonds, as presence of five-membered ring and terminal triple bonds has been reported recently. However, from the IR spectra shown above, the possibility of presence of terminal triple bonds in the final product is ruled out in this case. Topochemicity enhanced due to the self-assembly and orientation of the surfactant monomers within the inorganic framework limits the formation of unidentified polymeric byproducts, thereby giving small chain polynaphthalenes or its oligomers. We envisage formation of low molecular weight PN obtained by Bergman cyclization of polymerizable surfactant monomer within the hybrid nanocomposites formed by evaporation-induced self-assembly. The polymers thus obtained could be soluble and be applied in opto-electronic devices. This route to polynaphthalenes (or polyphenylenes) and their derivatives is most attractive since it requires no exogenous chemical catalysts or reagents for the polymerization.

Conclusion

In summary, we have demonstrated the preparation of chromophoric amphiphile/silica self-assembled nanocomposite films of PPP-C11 and FL-Stilbene-$(C11)_2$ with enhanced emission; thus tried to solve the problem of soild-state quenching of the organic chromophores to some extent. These nanocomposites showed nanosheet or nanorod morphology. The ability to tailor the orientation of the chromophore surfactant amphiphiles within the mesoscopic structures by solvent evaporation induced self-assembly in thin films and subsequent formation of well ordered chromophore nanopackets in this fashion dramatically impacts the photophysical properties of these materials. Moreover, chromophore amphiphile/silica self-assembly approach to overcome the problem of soild-state quenching in the development of organic light emitting devices with high efficiencies, carry the broad applicability that will enable new physical studies and device fabrication using these nanocomposite materials. Also, this method is free of chromophore leaching problem which is common in inclusion chemistry. The further design of surfactant amphiphiles with various chromophores employed at the tail ends will allow variations and improvement in the architecture at molecular and nanometer scales. The demonstration of 'controlled' chromophoric aggregation induced emission enhancement in self-assembled functional hybrid nanocomposites may stimulate new molecular engineering endeavours in the design of luminescent organics with highly emissive aggregation states.

Moreover, we have demonstrated Bergman cyclopolymerization of polymerizable amphiphilic surfactant monomer within the hexagonal

channels of functional hybrid nanocomposite formed by evaporation-induced self-assembly. Such a technique allows the patterned polymerization of the polymer precursor material directly onto a surface, thus avoiding solubility related problems that may be encountered when attempting to directly coat the pristine polymeric material, which is often insoluble, thereby facilitating its use in device fabrication.

References:

[1] R. Dagani, *Chem. Eng. News* **1999**, *77*, 25.

[2] E. Giannelis, *Adv. Mater.* **1996**, *8*, 29.

[3] T. Asefa, C. Yoshina-Ishii, M. J. a. McLachlan, G. A. Ozin, *J. Mater. Chem.* **2000**, *10*, 1751.

[4] R. C. Smith, W. M. Fischer, D. L. Gin, *J. Am. Chem. Soc.* **1997**, *119*, 4092.

[5] A. Sellinger, P. M. Weiss, A. Nguyen, Y. Lu, R. A. Assink, W. Gong, C. J. Brinker, *Nature* **1998**, *394*, 256.

[6] K. Moller, T. Bein, R. X. Fischer, *Chem. Mater.* **1998**, *10*, 1841.

[7] T. -Q. Nguyen, J. Wu, V. Doan, B. J. Schwartz, S. H. Tolbert, *Science* **2000**, *288*, 652.

[8] E. R. Kleinfeld, G. S. Ferguson, *Science* **1994**, *265*, 370.

[9] S. W. Keller, H.-N. Kim, T. E. Mallouk, *J. Am. Chem. Soc.* **1994**, *116*, 8817.

[10] G. Garnweitner, B. Smarsly, R. Assink, W. Ruland, E. Bond, C. J. Brinker, *J. Am. Chem. Soc.* **2003**, *125*, 5626.

[11] G. Schulz-Ekloff, D. Wohrle, B. van Duffel, R. A. Schoonheydt, *Microporous Mesoporous Materials* **2002**, *51*, 91.

[12] M. Ganschow, C. Hellriegel, E. Kneuper, M. Wark, C. Thiel, G. Schulz-Ekloff, C. Brauchle, D. Wohrle, *Adv. Funct. Mater.* **2004**, *14*, 269.

[13] M. Ganschow, M. Wark, D. Wohrle, G. Schulz-Ekloff, *Angew. Chem. Int. Ed.* **2000**, *39*, 161.

[14] M. Ganschow, I. Braun, G. Schulz-Ekloff, D. Wohrle, *Host-Guest Systems Based on Nanoporors Crystals*, WILEY-VCH Verlog GmbH and Co., Weinheim, **2003**.

[15] P. Innocenzi, G. Brusatin, *Chem. Mater.* **2001**, *13*, 3126.

[16] A. Costela, I. Garcia-Moreno, C. Gomez, O. Garcia, R. Sastre, *Appl. Phys. B* **2002**, *75*, 827.

[17] C. Peng, H. Zhang, J. Yu, Q. Meng, L. Fu, H. Li, L. Sun, X. Guo, *J. Phys. Chem. B* **2005**, *109*, 15278.

[18] B. McCaughey, C. Costello, D. Wang, J. E. Hampsey, Z. Yang, C. Li, C. J. Brinker, Y. Lu, *Adv. Mater.* **2003**, *15*, 1266.

[19] T.-Q. Nguyen, J. Wu, S. H. Tolbert, B. J. Schwartz, *Adv. Mater.* **2001**, *13*, 609.

[20] C.-G. Wu, T. Bein, *Science* **1994**, *266*, 1013.

[21] Y. Lu, Y. Yang, A. Sellinger, M. Lu, J. Huang, H. Y. Fan, G. P. Lopez, A. R. Burns, D. Y. Sasaki, J. A. Shelnutt, C. J. Brinker, *Nature* **2001**, *410*, 913.

[22] C. R. Martin, *Science* **1994**, *266*, 1961.

[23] D. J. Cardin, S. P. Constantine, A. Gilbert, A. K. Lay, M. Alvaro, M. S. Galletero, H. Garcia, F. Marquez, *J. Am. Chem. Soc.* **2001**, *123*, 3141.

[24] C. G. Wu, T. Bein, *Science* **1994**, *264*, 1757.

[25] S. Spange, A. Graser, A. Huwe, F. Kremer, C. Tintemann, P. Behrens, *Chem. Eur. J.* **2001**, *7*, 3722.

[26] G. M. Whitesides, B. Grzybowski, *Science* **2002**, *295*, 2418.

[27] C. J. Brinker, Y. Lu, A. Sellinger, H. Fan, *Adv. Mater.* **1999**, *11*, 579.

[28] C. T. Kresge, M. E. Leonowicz, W. J. Roth, J. C. Vartuli, J. S. Beck, *Nature* **1992**, *359*, 710.

[29] H. Yang, N. Coombs, I. Sokolov, G. A. Ozin, *Nature* **1996**, *381*, 589.

[30] Y. Lu, H. Fan, A. Stump, T. L. Ward, T. Rieker, C. J. Brinker, *Nature* **1999**, *398*, 223.

[31] C. Tsai, S. Tam, Y. Lu, C. J. Brinker, *J. Membr. Sci.* **2000**, *169*, 255.

[32] K. Domansky, J. Liu, L.-Q. Wang, M. H. Engelhard, S. Baskaran, *J. Mater. Res.* **2001**, *16*, 2810.

[33] P. D. Yang, G. Wirnsberger, H. C. Huang, S. R. Cordero, M. D. McGehee, B. Scott, T. Deng, G. M. Whitesides, B. F. Chmelka, S. K. Buratto, G. D. Stucky, *Science* **2000**, *287*, 465.

[34] I. Braun, G. Ihlein, F. Laeri, J. Nockel, G. Schulz-Ekloff, F. Schulth, U. Vietze, O. Weiss, D. Wohrle, *Appl. Phys. B* **2000**, *70*, 335.

[35] R. D. Miller, *Science* **1999**, *286*, 421.

[36] H. Y. Fan, e. al, *J. Non-Cryst. Solids* **2001**, *285*, 79.

[37] A. Okabe, T. Fukushima, K. Ariga, T. Aida, *Angew. Chem. Int. Ed.* **2002**, *41*, 3414.

[38] P. N. Minoofar, R. Hernandez, S. Chia, B. Dunn, J. I. Zink, A.-C. Franville, *J. Am. Chem. Soc.* **2002**, *124*, 14388.

[39] P. N. Minoofar, B. Dunn, J. I. Zink, *J. Am. Chem. Soc.* **2005**, *127*, 2656.

[40] Y. Lu, Y. Yang, A. Sellinger, M. Lu, J. Huang, H. Fan, R. Haddad, G. Lopez, A. R. Burns, D. Y. Sasaki, J. Shelnutt, C. J. Brinker, *Nature* **1999**, *410*, 913.

[41] N. Raman, M. Anderson, C. Brinker, *Chem. Mater.* **1996**, *8*, 1682.

[42] Q. Huo, D. Margolese, U. Ciesla, P. Feng, T. G. Gier, P. Sieger, R. Leon, P. M. Petroff, F. Schuth, G. Stucky, *Nature* **1994**, *368*, 317.

[43] P. T. Tanev, T. G. Pinnavia, *Science* **1995**, *267*, 865.

[44] D. M. Antonelli, J. Y. Ying, *Angew. Chem. Int. Ed.* **1995**, *34*, 2014.

[45] Y. Lu, R. Ganguli, C. Drwien, M. Anderson, C. Brinker, W. Gong, Y. Guo, H. Soyez, B. Dunn, M. Huang, J. Zink, *Nature* **1997**, *389*, 364.

[46] Y. Xia, B. Gates, Y. Yin, Y. Lu, *Adv. Mater.* **2000**, *12*, 693.

[47] D. Gracias, J. Tien, T. L. Breen, C. Hsu, G. M. Whitesides, *Science* **2000**, *289*, 1170.